Formation and Properties of Ion-Induced Nanoparticles in SiN_x

by

Justin C. Canniff

A dissertation submitted in partial fulfillment
of the requirements for the degree of
Doctor of Philosophy
(Materials Science and Engineering)
in the University of Michigan
2014

Doctoral Committee:

Professor Rachel S. Goldman, Chair
Professor Roy Clarke
Assistant Professor Emmanouil Kioupakis
Associate Professor Katsuyo S. Thornton

Acknowledgements

I would like to thank my family and friends, all of the teachers that have ever taught me, and give a special thanks to my fellow group members, past and present. I would like to give a special thanks to my wife Ji Yeon, for all her support and love.

I would also like to thank Vladimir for all his help and hard work in our research collaboration. In addition I would like to thank my committee for their guidance and helpful comments.

Support by the AFOSR through the MURI program under Grant No. FA9950-08-1-0340 is gratefully acknowledged. This research was also supported by the Center for Solar and Thermal Energy Conversion, an Energy Frontier Research Center funded by the U. S. Department of Energy, Office of Science, Office of Basic Energy Science under Award Number DE-SC0000957.

Table of Contents

List of Tables

List of Figures

List of Appendices

Abstract

Formation and Growth of Ion-Induced Nanoparticles in SiNx

by

Justin C. Canniff

Chair: Rachel S. Goldman

For many decades, there has been interest in low-dimensional structures (nanostructures) due to their expected unique physical properties. Due to the size dependence of their band gap energy, light emission, and free carrier confinement, NCs are promising for tandem solar cells, optical amplification medium, and memory applications. In addition, NCs may scatter acoustic phonons, thereby enabling engineering of the phonon mean free path and the resulting thermal conductivity. In this thesis, we examine the formation of metallic and semiconducting nanostructures using various focused-ion-beam irradiation doses followed by rapid-thermal-annealing. The mechanisms for nanocomposite formation and their influence on acoustic phonon resonances in SiN_x are examined.

For a range of high dose Ga^+ irradiations of SiN_x, we report on the formation of Si, SiN, Ga, and GaN embedded nanocrystals (NCs) as well as Ga-rich fractal morphologies. Since the fractal dimensions depend on surface Ga coverage, their growth may be due to rapid successive nucleation, local nucleation and fractal growth induced by

the release of heat during crystallization. During ultra-high dose Ga^+ irradiation, redeposition is enhanced by developing side walls, leading to enhanced near-surface [Ga] and [Si]. Subsequent RTA leads to the formation of Si and Ga NCs embedded in SiN_x. When the ratio of the irradiated area to the sidewall area is increased, redeposition is limited, and SiN_x and GaN NCs are also apparent. We discuss the effect of limited redeposition on NC formation and the catalytic effect of Ga on Si nucleation and growth.

For a combination of low and medium dose Ga^+ irradiation into SiNx, we report on the formation and coarsening of near-surface Ga nanoparticles (NPs). For surfaces with minimal curvature, diffusive growth is apparent. Following annealing at elevated temperatures, the diffusive flux is increased, leading to NP coarsening by Ostwald ripening. For surfaces with increased curvature, the driving force for diffusion towards the valleys also increases, leading to Ga NP coalescence and a bi-modal distribution of NP sizes.

Finally, we have investigated the effect of embedded NCs on coherent acoustic phonon damping in SiNx membranes. Similar acoustic phonon damping was observed for the as-received, annealed, and as-implanted SiNx membranes whose thickness exceeds 200nm. For the thinner SiNx membranes, an increase in acoustic phonon damping is observed for both as-received membranes and those which were implanted and annealed to form nano crystallites.

Chapter 1

Introduction

1.1 Overview

For many decades, there has been interest in low-dimensional structures (nanostructures) due to their expected unique physical properties. For semiconductor nanostructures, with sizes similar to or less than the Bohr exciton radius, the effective bandgap is dependent on the size of the nanostructure.[1] Also, when the size of the nanocrystals is similar to the phonon wavelength, phonon damping is enhanced.[2] Semiconductor nanocomposites may be formed by a wide variety of methods including molecular beam epitaxy, atomic beam deposition, evaporation, or solution-based deposition. However, these techniques offer limited control over size and shape uniformity of nanocrystal ensembles,[3,4,5,6,7,8,9] often due to the agglomeration of NPs.[3,4,5,10] Ion implantation followed by subsequent thermal processing or further ion irradiation has been used to induce the precipitation of nanoparticles within a host matrix.[11,12,13,14,15,16] Furthermore, focused ion beam (FIB) implantation has shown promise for allowing selective lateral patterning of nanostructures. Implantation areas have produced selective nucleation sites for Ge islands on Si,[17] near-surface GaN nanocrystals in GaAs,[18] Cu_2O nanodots on $SrTiO_3$,[19] and InP nanowires on GaAs.[20] In this thesis, we examine the selective formation and spatial positioning of Si, SiN, Ga, and

GaN embedded NCs and near-surface Ga NPs in SiN_x, synthesized by Ga^+ focused ion beam (FIB) irradiation and subsequent RTA.

This chapter opens with a description of key unique properties of nanostructured semiconductors including electron confinement and phonon scattering. We then discuss the predicted and observed properties of GaN, Si, and Ga nanostructures along with their applications and synthesis. Finally, this chapter concludes with an outline and objectives of the dissertation.

1.2 Nanostructured Semiconductors: Confining Electrons and Scattering Phonons

1.2.1 Electron Confinement

For semiconductor nanostructures, the effective bandgap is dependent on the size of the nanostructure, when the size is similar to the Bohr exciton radius. The Bohr exciton radius is the size at which the energy of the electron-hole pairs (excitons) becomes split into discrete states, leading to quantum confinement.[21] For GaN, the Bohr exciton radius is expected to be 2.8-11 nm,[22,23,24] while for Si, it is expected to be ~2.2 nm.[25] For insulating materials like Si_3N_4, which have a bandgap larger than 5 eV, the Bohr radius is expected to be very small, similar in size to the unit cell.[26] Most processing methods are limited, and cannot achieve nanostructures small enough for quantum confinement. Stranski-Krastanow (SK) growth has been used to form nanostructures as small as 10 nm in diameter,[27,28,29] but that is only small enough for quantum-confinement in materials with large Bohr exciton radii, such as InAs with a 30-

34 nm Bohr exciton radius.[30,31] For SK growth, the minimum size of the nanostructures is limited by the misfit strain between the film and substrate.[32,33] Although droplet epitaxy of QDs in not limited by misfit strain,[34] the smallest GaN reported to date have similar ~10 nm diameters.[35,36,37] The controlled formation of nanostructures through ion-beam synthesis, as discussed below, has been used to form nanostructures as small as ~5 nm,[38,39] potentially enabling quantum confinement in materials with smaller Bohr exciton radii, such as Si[25] and GaN.[22,23,24]

1.2.2 Scattering of Acoustic Phonons

In nanocomposite materials consisting of nanocrystals in a matrix, the phonon wavelength is similar to the size of the nanocrystals, resulting in enhanced scattering of the waves by the grain boundaries as illustrated in Fig. 1.1.[40] This scattering leads to the gradual loss of phonon energy that is typically proportional to either ω^2 or ω^4.[6,41,42,43,44,45] The thermal conductivity of various nanostructures including nanowires and nanocomposites is also reduced due to phonon scattering at boundaries. Thus, a multilayer structure of Ge nanoparticles on Si layers led to decreased thermal conductivity below the amorphous limit.[46] In another study, resonant acoustic waves in Si membranes were examined, but only the fundamental mode is observed.[47] In other work, resonant acoustic modes in a semiconductor membrane were observed to be dependent on the repetition-rate frequency offset in an ASOPS configuration (see section 2.9).[48] Directly correlating nanostructures to the damping of specific acoustic phonon

frequencies can potentially enable engineering of the phonon mean free path, which can enable thermal conductivity minimization.

1.3 Visible Optoelectronics: GaN and SiN_x Nanostructures

Due to its direct bandgap, GaN is of interest for high temperature electronic and visible optoelectronic applications.[49] GaN typically crystallizes in a WZ structure, but ZB GaN has also been reported, offering several advantages over WZ GaN, including higher carrier mobilities[50,51] and lower bandgaps (3.28-3.23 eV[52,53] vs. 3.5 eV). Polarized spontaneous light emission from LEDs fabricated on $(10\bar{1}0)$ *m* plane WZ GaN is potentially useful in liquid crystal display applications,[54] while WZ GaAsN is potentially useful in short-wavelength laser applications.[55,56] The piezoelectric properties of WZ GaN have potential applications in field-effect transistors and diodes, where mechanical stress is converted to electric energy.[57] Alternatively, the zinc-blende (ZB) phase of GaN is potentially free of polarization fields, which may reduce internal electric fields that can be detrimental to ultraviolet optoelectronic device performance.[58,59] In addition, GaN is of interest for high frequency power transistors (>10 GHz) due to its expected high maximum electron velocity, high electron mobility, and high breakdown field.[60] GaN-based light emitting diode, laser diode, detector, and transistor performance has been improved by SiN passivation or buffer layers.[61,62,63,64,65,66,67,68,69,70,71] GaN nanostructures have been grown by a variety of methods including metal-organic chemical vapor deposition (MOCVD),[6,72,73] molecular beam epitaxy (MBE),[74,7] and colloidal growth[10,3] with NC sizes ranging from ~3 - 40 nm. Ga^+ implantation into N-

rich (x > 1.5) α-SiN_x:H_y leads to preferential Ga displacement of Si, resulting in Ga-N, Ga-Ga, and Si-H bond formation.[75,76,77] In another report, 0.06 to 5 keV Ga^+ implantation into SiN induces the formation of an amorphous GaN surface layer,[78] subsequently used for seeding the epitaxial growth of GaN.[79]

1.4 Solar Cells and Flash Memory: Si Nanostructures

Due to the size dependence of their band gap energy, Si NCs embedded within a dielectric matrix are of interest for tandem solar cells.[80] Quantum confinement effects for Si NCs have been observed for NCs with diameters less than ~7 nm.[81] To maximize the efficiency of a two-cell tandem all-Si solar cell, the top cell should have a band gap of ~1.75 eV, while the bottom cell is crystalline Si (1.1 eV bandgap).[82] A diagram of this tandem cell is shown in Fig. 1.2. Si NCs with diameters as small as ~2 nm and bandgaps ranging from 1.5 to 3.0 eV have been embedded in various dielectric substrates including SiO_2,[83] Si_3N_4,[84] and SiC.[85]

Due to their confinement of free carriers, Si NCs are also promising for use in flash memory.[86] In flash memory, as shown in Fig. 1.3, the NCs are separated from the source and drain by a thin oxide layer, called the tunnel oxide. Electrons can be stored in the NCs by applying a forward bias to the gate with respect to the source and drain.[86] This stored charge will screen the gate, increasing the threshold voltage of the transistor. The voltage shift for one electron per nanocrystal has been described as:

$$\Delta V_T = \frac{q n_{well}}{\epsilon_{ox}} \left(t_{cntl} + \frac{\epsilon_{ox} t_{well}}{2\epsilon_{Si}} \right) \quad (1.2)$$

Where ΔV_T is the threshold voltage shift, n_{well} is the density of nanocrystals, ϵ_{ox} is the permittivity of the oxide, t_{cntl} is the thickness of the control oxide, t_{well} is the linear dimension of the nanocrystal well, and ϵ_{Si} is the permittivity of Si.[86] Basic flash memory stores a bit of data by distinguishing between the different threshold voltage states, shifted or unshifted. A larger threshold voltage shift allows the memory to have more than two distinguishable states, by utilizing intermediate voltage shift states to effectively store multiple bits of data per transistor. It is therefore advantageous to increase the threshold voltage shift, which can be accomplished by increasing the nanocrystal density, as shown by Equation 1.2. Other work has found that B doping of Si NCs has been shown to enhance the threshold voltage shift.[87] Since Ga has been used as both a dopant of Si NCs[88,89] and as a catalyst for Si nanowire growth,[90,91] it may provide an opportunity for simultaneous doping and catalysis of Si NCs. Co-sputtering[92,93] and plasma-enhanced chemical vapor deposition (PECVD)[94,95] of Si-rich SiO_2 or SiN_x, followed by annealing, have been used to nucleate embedded Si NCs throughout the film thickness. Si irradiation in conjunction with annealing has also been used to fabricate Si NCs at select depths within both SiO_2 and SiN_x.[96,97,98,99,100,101] Local regions of excess Si have also been achieved by breaking Si-N bonds in SiN_x using Ti^+, B^+, and Ga^+ ions.[102,103,104,105,106]

1.5 Nanowire Catalysts: Ga Nanoparticles

Due to the size dependence of their band gap energy and light emission, silicon nanowires (NWs) are promising for solar cells[107] and light emitting devices.[108] Nanoparticles (NPs) of various metals have been used to catalyze the VLS growth of Si

NWs, as shown in the diagram in Fig. 1.4.[109,110,111,112,113,114,115,116,117,118,119,120,121,122,123] Since Si NWs have been predicted to exhibit a strong increase in quantum confinement for diameters less than 2.2 nm,[110] it is important to control the diameter of the NWs, which is dependent on the diameter of the nanoparticles (NPs).[123,124] The growth direction of the NWs has also been shown to be dependent on the NP diameter, with NWs less than 20 nm being mostly <110> oriented, while larger wires also form in the <112> and <111> directions.[125] Due to their lower NW processing temperatures, Ga and Au catalysts are preferred over Ni and Fe catalysts.[130] However Au often forms deep impurity levels in the Si band gap,[126] while Ga has been used as a dopant of Si NCs.[127,128] Use of a Ga catalyst For VLS growth of Si NWs has been limited by the low silane dehydrogenation activity of Ga.[129] Recently, Ga catalyzed Si NWs have been realized by using silane plasma highly diluted in hydrogen.[130] Ga NPs have been formed by various methods including molecular beam epitaxy,[111,117,131,132,133] Ga atomic beam,[134,135] chemical liquid deposition,[136] or evaporation[120,137] on various substrates including Si,[122] SiC,[111] GaAs,[117,131] Al_2O_3,[133] GaN,[132] SiO_2,[116,121,134] Si_3N_4,[121] and glass.[120] Ga NPs have been formed with sizes as small as ~5.6 nm (density ~$4x10^{10}$ cm^{-2})[136] and densities as high as ~$1.5x10^{11}$ cm^{-2} (diameter >20 nm).[132] Ga^+ focused-ion-beam (FIB) irradiation, followed by annealing, has also been used as a means to achieve small Ga NPs within selected areas.[91,138] Random nucleation sites as well as agglomeration and coalescence are among the many mechanisms that must be controlled to achieve an ideal NP array.

1.6 Dissertation Objectives

The first part of this thesis work focuses on Si, SiN, Ga, and GaN nanocrystal formation in Ga-implanted and annealed SiN_x. The influence of the sample surface topography on redeposition and subsequent NC formation was examined. For patterned samples, redeposition is enhanced by developing side walls, leading to enhanced near-surface [Ga] and [Si]. Subsequent RTA leads to the formation of Si and Ga NCs embedded in SiN_x. When the ratio of the irradiated area to the sidewall area is increased, redeposition is limited, and SiN_x and GaN NCs are also apparent. We also observed the catalytic effect of Ga on Si NC formation. When the [Ga] was increased, Si NC nucleation was observed. Upon annealing Si NCs grew and coalesced. By patterning areas of increased [Ga] with the FIB, we have demonstrated control of the nucleation locations of Si NCs.

The middle part of this thesis is devoted to low dose Ga implantations into SiN_x and the resultant Ga NPs. The influences of annealing-induced bulk diffusion (due to [Ga] gradient) and surface diffusion (due to the chemical potential gradient) on Ga NP nucleation, growth, and coalescence by varying the ion fluence, beam spot separation (pitch), and annealing. When surface curvature is limited, dose-limited diffusive growth is apparent, leading to nearly close packed arrays with NP diameters as small as 3 nm and densities as high as ~$4x10^{12}$ cm^{-2}. When annealed at elevated temperatures, the diffusive flux is increased, leading to NP coarsening by Ostwald ripening. When surface curvature is increased, the driving force for diffusion towards the valleys also increases, leading to Ga NP coalescence and a bi-modal distribution of NP sizes.

In the final part of this thesis, we examine the effect of nanostructures on the coherent acoustic phonon damping in SiN_x. The similarity between the nanostructure

dimensions and the mean free path of the acoustic phonons is expected to increase phonon damping. Similar acoustic phonon damping was observed for the 200 nm unimplanted, unimplanted-annealed, and as-implanted samples. For the thinner 100 nm samples, a ~30% increase in damping was observed. The present studies not only show a linear-like relationship between the damping and acoustic mode frequency, but also demonstrate a clear damping dependency on the SiN_x membrane thickness. Both the FWHM as a function of frequency and the FWHM data suggest increased damping for the nanocrystalline sample relative to the amorphous samples, likely due to the similarity of the NC dimensions and the phonon wavelength. Further experiments could directly correlate nanostructures to damping of specific acoustic phonon frequencies, enabling engineering of the phonon mean free path that can allow for thermal conductivity minimization.

1.7 Dissertation Organization

This dissertation is organized as follows. Chapter 2 describes the experimental procedures used for this thesis work, including focused ion beam (FIB) irradiation, transmission electron microscopy (TEM), photolithography, metal deposition, and pump-probe thermoreflectance experiments.

In Chapter 3, we discuss the formation of embedded Si, SiN, Ga, and GaN nanocrystals (NCs) in SiN_x using Ga+ focused-ion beam irradiation of SiN_x membranes, followed by rapid thermal annealing (RTA). During irradiation, redeposition is enhanced by developing side walls, leading to enhanced near-surface [Ga] and [Si], while N likely

escapes as N_2.[139] We examine TEM images and SAD patterns of the NCs formed in these samples. We also discuss the NC sizes after annealing at 900ºC and the catalytic effect of Ga on Si NC formation.

Chapter 4 presents investigations of low dose Ga implantations into SiNx and the resultant Ga NPs. We examine the effects of annealing-induced diffusion, due to the vertical [Ga] gradient and the chemical potential gradient, on the growth and coalescence of Ga NPs. Using HAADF STEM images, we examine the size and distribution of the Ga NPs following irradiation and annealing. We also examine the effect of pitch on the nucleation and growth of Ga NPs. For beam spot separations (pitch) less than the lateral spread of implanted ions, dose-limited diffusive growth is apparent. When the pitch exceeds the lateral spread of implanted ions, the surface roughness increases, and Ga NP coalescence is apparent, leading to a bi-modal distribution of NP sizes. We compare STEM and AFM images to understand the effect of surface curvature and the chemical potential gradient on the resulting NP distribution.

In Chapter 5, we examine the effect of nanostructure on coherent acoustic phonon damping. Similar damping was observed for 200nm thick unimplanted, unimplanted-annealed, and as-implanted samples. For thinner 100 nm samples, a ~30% increase in damping was observed. We examine FFTs of the thermoreflectance signals to estimate the acoustic phonon damping as a function of frequency. The present studies show not only a linear-like relationship between damping and acoustic mode frequency, but also demonstrate a clear damping dependency on SiN_x membrane thickness. More work will also be needed to detect the effect of implantation and nanostructure modification on damping. Both the FWHM as a function of frequency and the FWHM data suggest

increased damping for the nanocrystalline sample relative to the amorphous samples. The increase is associated with the similarity in length scale of the NC dimensions and the phonon wavelength. Further experiments could directly correlate nanostructures to damping of specific acoustic phonon frequencies, enabling engineering of the phonon mean free path that can allow for thermal conductivity minimization. Finally in Chapter 6, we present a summary and suggestions for future work.

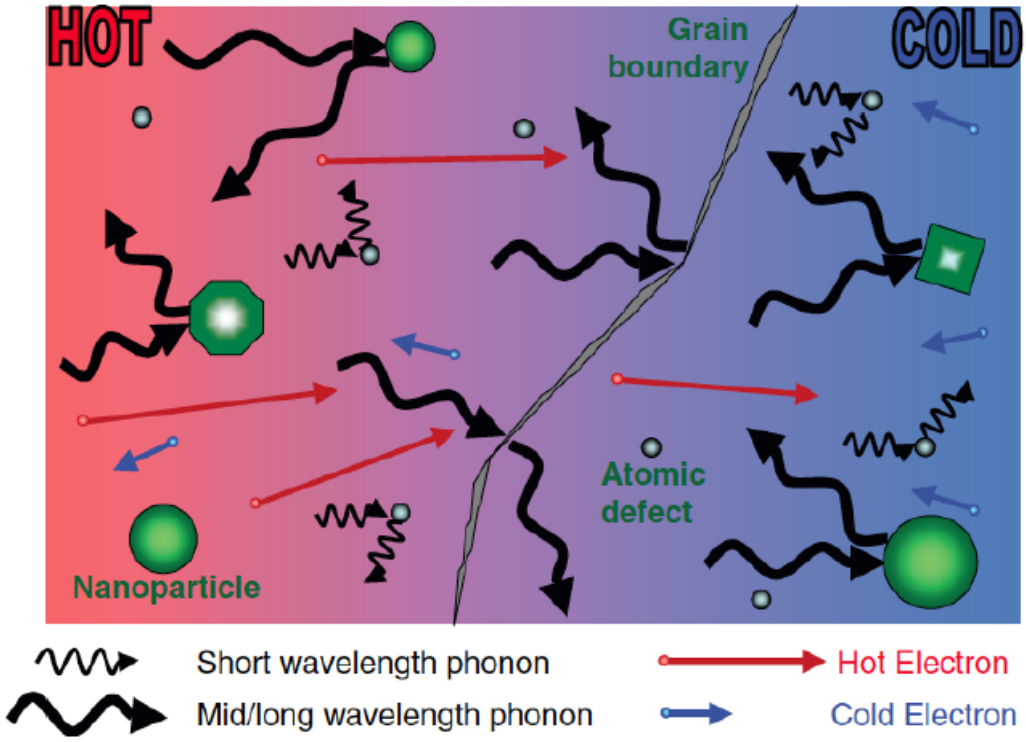

Fig. 1.1 NCs in a matrix scattering phonons that have a wavelength similar to the diameter of the NC. Reprinted with permission from [140]. Copyright 2010 John Wiley and Sons.

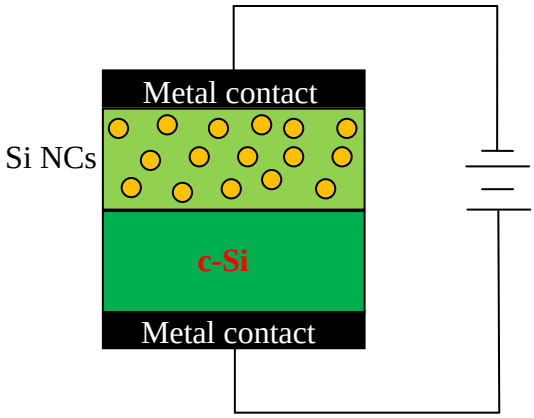

Fig. 1.2 Diagram of an all Si tandem solar cell with a top cell of Si QDs and a bottom cell of crystalline Si.

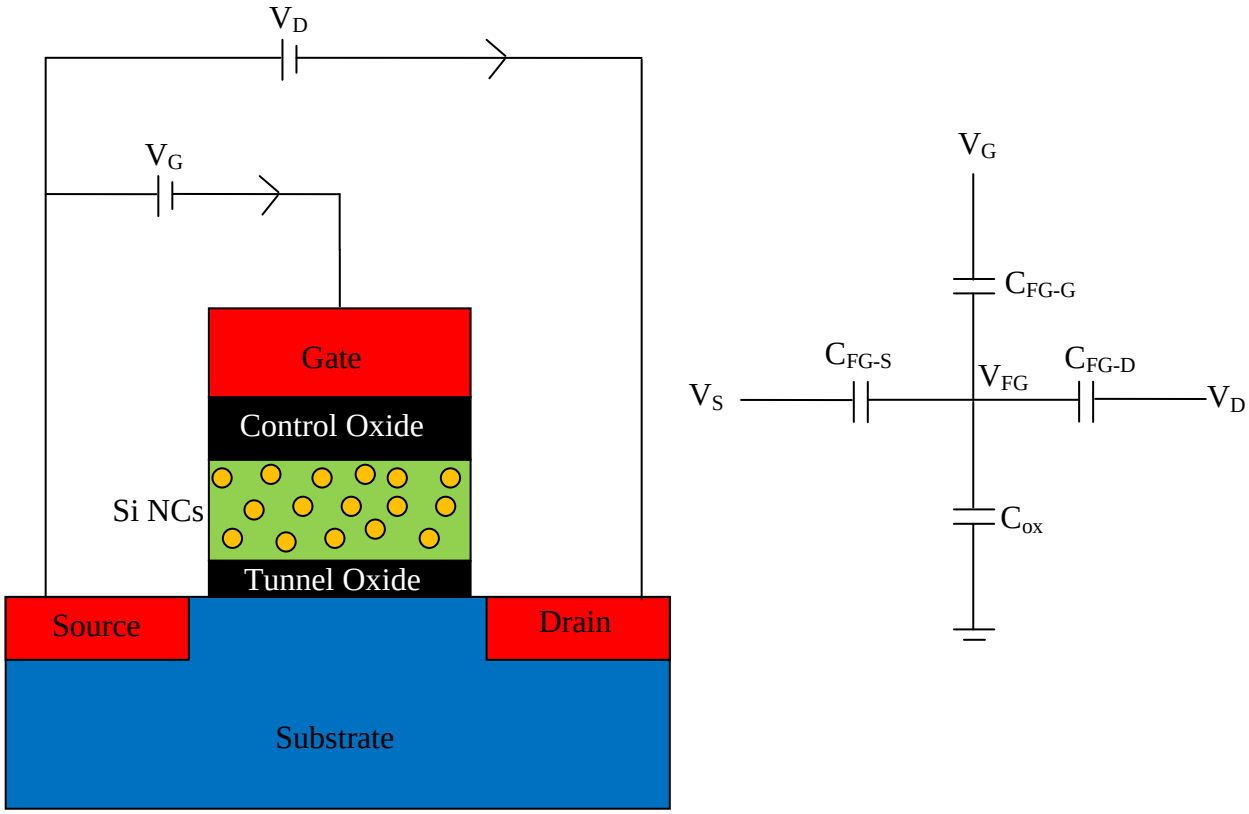

Fig. 1.3 Diagram of flash memory transistor with a Si NC layer between the tunnel oxide and control oxide, which is used to store charge.

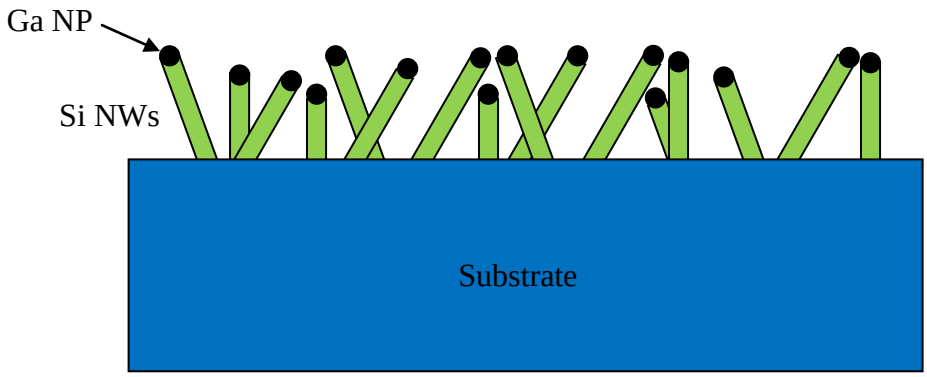

Fig. 1.4 Diagram of Si NWs grown using Ga NPs as a catalyst.

1.8 References

[1] A. P. Alivisatos, Science **271**, 933 (1996).

[2] H. Casimir, Physica (Amsterdam) 5, 495 (1938).

[3] O. I. Mićić, S. P. Ahrenkiel, D. Bertram, and A. J. Nozik, Appl. Phys. Lett. **75**, 478 (1999).

[4] Y. Xie, Y. Qian, W. Wang, S. Zhang, and Y. Zhang, Science **272**, 1926 (1996).

[5] K. Sardar, C. N. R. Rao, Adv. Mater. **16**, 425 (2004).

[6] K. Tachibana, T. Someya, and Y. Arakawa, Appl. Phys. Lett. **74**, 383 (1999).

[7] J. Ristić, E. Calleja, A. Trampert, S. Fernández-Garrido, C. Rvera, U. Jahn, and K. H. Ploog, Phys. Rev. Lett. **94**, 146102 (2005).

[8] M. Kolibal, T. Cechal, E. Brandejsova, J. Cechal and T. Sikola, Nanotechnology **19**, 475606 (2008).

[9] M. Hernandez, M. Cervera, E. Ruiz, J. L. Pau1, J. Piqueras, M. Avella, and J. Jimenez, Nanotechnology **21**, 455602 (2010).

[10] M. R. Greenberg, G. A. Smolyakov, J. C. Jones, S. D. Bunge, T. J. Boyle, and M. Osinski, "Synthesis and Characterization of InP and InN Colloidal Nanocrystals," in *Conference on Lasers and Electro-Optics/Quantum Electronics and Laser Science Conference and Photonic Applications Systems Technologies*, Technical Digest (CD) (Optical Society of America, 2006), paper CTuN5.

[11] A. Meldrum, R. F. Haglund, Jr., L. A. Boatner, and C. W. White, Adv. Mater. **13**, 1431 (2001).

[12] E. Rimini, “Ion implantation: basics to device fabrication” (Kluwer Acad. Pub. Boston, MA, 1995).

[13] C. W. White, A. Meldrum, J. D. Budai, S. P. Withrow, E. Sonder, R. A. Zuhr, D. M. Hembree, M. Wu, D. O. Henderson, Nucl. Instrum. Methods B **148**, 991 (1999).

[14] K. H. Heinig, B. Schmidt, A. Markwitz, R. Grötzschel, M. Strobel, S. Oswald, Nucl. Instrum. Methods B **148**, 969 (1999).

[15] T. Shimizu-Iwayama, M. Oshima, T. Niimi, S. Nakao, K. Saitoh, T. Fujita, N. Itoh, J. Phys.: Condens. Matter **5**, 375 (1993).

[16] A. Meldrum, R. F. Haglund, Jr., L. A. Boatner, and C. W. White, Adv. Mater. **13**, 1431 (2001).

[17] A. Portavoce, R. Hull, M. C. Reuter, F. M. Ross, Appl. Phys. Lett. **82**, 1093 (2003).

[18] A. W. Wood, R. R. Collino, B. L. Cardozo, F. Naab, Y. Q. Wang, and R. S. Goldman, J. Appl. Phys. **110**, 124307 (2011).

[19] J.F. Groves, Y. Du, I. Lyubinetsky, D.R. Baer, Superlattices and Microstructures **44** (4-5), 677-685 (2008)

[20] J. Ahopelto, H. Lezec and Y. Ochiai, A. Usui, H. Sakaki, Appl. Phys. Lett. **64**, 499 (1994)

[21] A. P. Alivisatos, Science **271**, 933 (1996).

[22] P. Ramvall, S. Tanaka, S. Nomura, P. Riblet, and Y. Aoyagi, Appl. Phys. Lett. **73**, 1104 (1998).

[23] J. Zhang, L. D. Zhang, X. F. Wang, C. H. Liang, and X. S. Peng, J. Chem. Phys. **115**, 5714 (2001).

[24] S. Chichibu, T. Azuhata, T. Sota, and S. Nakamura, *Appl. Phys. Lett*. **69**, 4188 (1996).

[25] X. Zhao, C. M. Wei, L. Yang, and M. Y. Chou, Phys. Rev. Lett. **92**, 236805 (2004).

[26] Fox, Mark. *Optical Properties of Solids*; Oxford University Press: New York, 2010.

[27] X.-Q. Shen, S. Tanaka, S. Iwai, and Y. Aoyagi, Appl. Phys. Lett. **72**, 344 (1998).

[28] C. Adelmann, J. Simon, G. Feuillet, N. T. Pelekanos, B. Daudin, and G. Fishman, Appl. Phys. Lett. **76**, 1570 (2000).

[29] F. Widmann, J. Simon, B. Daudin, G. Feuillet, J. L. Rouvière, N. T. Pelekanos, and G. Fishman, Phys. Rev. B **58**, 15989 (1998).

[30] G. Bastard, E. E. Mendez, L. L. Chang, and L. Esaki, Phys. Rev. B **26**, 1974 (1982).

[31] A. C. Ford, J. C. Ho, Y. –L. Chueh, Y. –C. Tseng, Z. Fan, J. Guo, J. Bokor, and A. Javey, Nanoletters **9**, 360 (2009).

[32] J. Tersoff, Phys. Rev. Lett. **81**, 3183 (1998).

[33] J. Tersoff and F. K. LeGoues, Phys. Rev. Lett. **72**, 3570 (1994).

[34] S. Naritsuka, T. Kondo, H. Otsubo, K. Saitoh, Y. Yamamoto, and T. Maruyama, J. Cryst. Growth **300**, 118 (2007).

[35] T. Kondo, K. Saitoh, Y. Yamamoto, T. Maruyama, and S. Naritsuka, Phys. Stat. Sol. A **203**, 1700 (2006).

[36] T. Maruyama, H. Otsubo, T. Kondo, Y. Yamamoto, and S. Naritsuka, J. Cryst. Growth **301-302**, 486 (2007).

[37] A. S. Özcan, Y. Wang, G. Ozaydin, K. F. Ludwig, A. Bhattacharyya, T. D. Moustakas, and D. P. Siddons, J. Appl. Phys. **100**, 084307 (2006).

[38] A. W. Wood, X. Weng, Y. Q. Wang, and R. S. Goldman, Appl. Phys. Lett. **99**, 093108 (2011).

[39] X. Weng, S. J. Clarke, W. Ye, S. Kumar, A. Daniel, R. Clake, J. Holt, J. Sipowska, A. Francis, V. Rotberg, and R. S. Goldman, J. Appl. Phys. **92**, 4012 (2002).

[40] H. Casimir, Physica (Amsterdam) 5, 495 (1938).

[41] D. B. Hondongwa, B. C. Daly, T. B. Norris, B. Yan, J. Yang, and S. Guha Phys. Rev. B 83, 121303 (2011).

[42] G. Baldi, V. M. Giordano, G. Monaco, F. Sette, E. Fabiani, A. Fontana, and G. Ruocco, Phys. Rev. B **77**, 214309 (2008).

[43] G. Baldi, V. M. Giordano, G. Monaco, and B. Ruta, Phys. Rev. Lett. **104**, 195501 (2010).

[44] J.-Y. Duquesne and B. Perrin, Phys. Rev. B **68**, 134205 (2003).

[45] F. Hudert, A. Bruchhausen, D. Issenmann, O. Schecker, R. Waitz, A. Erbe, E. Scheer, T. Dekorsy, A. Mlayah, and J.-R. Huntzinger, Phys. Rev. B **79**, 201307(R) (2009).

[46] G. Pernot et al., Nature Mater. 9, 491 (2010).

[47] J. Cuffe1, O. Ristow, E. Chávez, A. Shchepetov, P-O. Chapuis, F. Alzina, M. Hettich, M. Prunnila, J. Ahopelto, T. Dekorsy, and C. M. Sotomayor Torres, Phys. Rev. Lett. **110**, 095503 (2013).

[48] A. Bruchhausen, R. Gebs, F. Hudert, D. Issenmann, G. Klatt, A. Bartels, O. Schecker, R, Waitz, A. Erbe, E. Scheer, J.-R. Huntziner, A. Mlayah, and T. Dekorsy, Phys. Rev. Lett. **106**, 077401 (2011).

[49] I. Akasaki and H. Amano, Jpn. J. Appl. Phys. **36**, 5393(1997).

[50] P. Das and D. K. Ferry, *Solid-State Electron.* **19**, 851 (1976).

[51] H. Yang, L.X. Zheng, J.B. Li, X.J. Wang, D.P. Xu, Y.T. Wang, X.W. Hu, and P.D. Han, Appl. Phys. Lett. **74**, 2498 (1999).

[52] G. Ramírez-Flores, H. Navarro-Contreras, A. Lastras-Martínez, R. C. Powell, and J. E. Greene, Phys. Rev. B **50**, 8433 (1994).

[53] Z. Sitar, M. J. Paisley, J. Ruan, J. W. Choyke, and R. F. Davis, J. Mater. Sci. Lett. **11**, 261 (1992).

[54] N. F. Gardner, J. C. Kim, J. J. Wierer, Y. C. Shen, and M. R. Krames, Appl. Phys. Lett. **86**, 111101 (2005).

[55] H.J. Kim, T.G. Andersson, J.-M. Chauveau, and A. Trampert, J. Appl. Phys. **94**, 7193 (2003).

[56] H.J. Kim, T.G. Andersson, J.-M. Chauveau, and A. Trampert, Appl. Phys. Lett. **81**, 3407 (2002).

[57] Z. L. Wang, Adv. Mater. **19**, 889 (2007).

[58] T.X. Wang, Y. Li, and Y.M. Liu, Phys. Status Solidi B **248**, 1671 (2011).

[59] C. Adelmann, E. Martinezguerrero, F. Chabuel, J. Simon, B. Bataillou, G. Mula, L. Dang, N. Pelekanos, B. Daudin, and G. Feuillet, Mater. Sci. Eng. B **82**, 212 (2001).

[60] B. Monemar, J. Mat. Sci. Mater. Electr. **10**, 227 (1999).

[61] J. Bernát, P. Javorka, M. Marso, and P. Kordoš, Appl. Phys. Lett. **83**, 5455 (2003).

[62] Z.H. Feng, Y.G. Zhou, S.J. Cai, and K.M. Lau, Appl. Phys. Lett. **85**, 5248 (2004).

[63] J. Derluyn, S. Boeykens, K. Cheng, R. Vandersmissen, J. Das, W. Ruythooren, S. Degroote, M.R. Leys, M. Germain, and G. Borghs, J. Appl. Phys. **98**, 054501 (2005).

[64] M. Wang, B. Shen, F. Xu, Y. Wang, J. Xu, S. Huang, Z. Yang, Z. Qin, and G. Zhang, Phys. Lett. A **369**, 249(2007).

[65] Z. Fang, S. Li, J. Li, H. Sun, S. Wang, and J. Kang, Thin Solid Films **516**, 6344(2008).

[66] Z.L. Fang, J.Y. Kang, W.J. Huang, H.T. Sun, M. Lu, J.F. Kong, and W.Z. Shen, J. Phys. Chem. C **112**, 4925 (2008).

[67] S.-E. Park, S.-M. Lim, C.-R. Lee, C.S. Kim, and B. O, J. Cryst. Growth **249**, 487 (2003).

[68] J. Yanagisawa, M. Toda, T. Kitamura, H. Matsumoto, and Y. Akasaka, J. Vac. Sci. Technol. B **23**, 3205 (2005).

[69] J. Yanagisawa, Nucl. Instrum. Meth. B **257**, 348 (2007).

[70] C.M. Tsai, Jinn-Kong Sheu, Wei-Chih Lai, Ming-Lun Lee, Shoou-Jinn Chang, C.S. Chang, T.K. Ko, and C.F. Shen, IEEE J. Select. Topics Quantum Electron. **15**, 1275 (2009).

[71] C. Liu, R. Chuang, S. Chang, Y. Su, C. Kuo, J. Tsai, and C. Lin, Mater. Sci. Eng. B **111**, 214 (2004).

[72] M. Miyamura, K. Tachibana, and Y. Arakawa, Appl. Phys. Lett. **80**, 3937 (2002).

[73] S. C. Davies, D. J. Mowbray, Q. Wang, F. Ranalli, and T. Wang, Appl. Phys. Lett. **95**, 101909 (2009).

[74] B. Daudin, F. Widmann, G. Feuillet, C. Adelmann, Y. Samson, M. Arlery, and J. L. Rouviere, Mater. Sci. Eng. B, **50**, 8 (1997).

[75] S.A. Almeida, S.R.P. Silva, B.J. Sealy, and J.F. Watts, Phil. Mag. Lett. **78**, 319 (1998).

[76] S. Almeida, S. Silva, B. Sealy, and J. Watts, Thin Solid Films **343-344**, 632 (1999).

[77] S.R.P. Silva, S.A. Almeida, and B.J. Sealy, Nucl. Instrum. Meth. B **147**, 388 (1999).

[78] J. Yanagisawa, M. Toda, T. Kitamura, H. Matsumoto, and Y. Akasaka, J. Vac. Sci. Technol. B **23**, 3205 (2005).

[79] J. Yanagisawa, Nucl. Instrum. Meth. B **257**, 348 (2007).

[80] E. C. Cho, S. Park, X. Hao, D. Song, G. Conibeer, S. C. Park, and M. A. Green, Nanotechnology **19**, 245201 (2008).

[81] M. Green, E. Cho,Y. Cho,E. Pink, T. Trupke, K. Lin, T. Fangsuwannarak, T. Puzzer, G. Conibeer and R. Corkish Proc. 20th European Photovoltaic Solar Energy Conf. (Barcelona) (2005).

[82] F. Meillaud, A. Shah, C. Droz, E. Vallat-Sauvain and C. Miazza Sol. Energy Mater. Sol. Cells **90**, 29522 (2006).

[83] M. Zacharias, J. Heitmann, R. Scholz, U. Kahler and M. Schmidt Appl. Phys. Lett. **80**, 661 (2002).

[84] T. Kim, C. Cho, B. Kim, and S. Park, Appl. Phys. Lett. **88**, 123102 (2006).

[85] Y. Kurokawa, S. Miyajima, A. Yamada, and M. Konagai, Japan. J. Appl. Phys. **45**, L1064 (2006).

[86] S. Tiwari, F. Rana, H. Hanafi, A. Hartstein, E. F. Crabbe, and K. Chan, Appl. Phys. Lett. **68** 1377 (1996).

[87] Y.-H. So, S. Huang, G. Conibeer, and M. A. Green, Eur Phys. Lett. **96**, 17011 (2011).

[88] V. Svrcek and M. Kondo, IEEE Photovoltaics Specialists Conference, 837 (2009).

[89] Z. Zhou, M. L. Steigerwald, R. A. Friesner, and L. Brus, Phys. Rev. B **71**, 245308 (2005).

[90] M. K. Sunkara, S. Sharma, R. Miranda, G. Lian, and E.C. Dickey, Appl. Phys. Lett. **79**, 1546 (2001).

[91] M. Hetzel, A. Lugstein, C. Zeiner, T. Wójcik, P. Pongratz, and E. Bertagnolli, Nanotechnology **22**, 395601 (2011).

[92] M. Fujii, M. Yoshida, Y. Kanzawa, S. Hayashi, and K. Yamamoto, Appl. Phys. Lett. **71**, 1198 (1997).

[93] L. Dal Negro, R. Li, J. Warga, and S. N. Basu, Appl. Phys. Lett. 92, 181105 (2008).

[94] F. Priolo, G. Franzo, D. Pacifici, V. Vinciguerra, F. Iacona, and A. Irrera, J. Appl. Phys. **89**, 264 (2001).

[95] W. C. Ding, D. Hu, J. Zheng, P. Chen, B. W. Cheng, J. Z. Yu and Q. M. Wang, J. Phys. D: Appl. Phys. 41 (2008).

[96] P. G. Kik, M. L. Brongersma, and A. Polman, Appl. Phys. Lett. **76**, 2325 (2000).

[97] P. G. Kik and A. Polman, J. Appl. Phys. **88**, 1992 (2000).

[98] V. Ioannou-Sougleridis, P. Dimitrakis, V.E. Vamvakas, P. Normand, C. Bonafos, S. Schamm, A. Mouti, G.B. Assayag, and V. Paillard, Nanotechnology **18**, 215204 (2007).

[99] S. Choi, S. Baek, M. Jang, S. Jeon, J. Kim, C. Kim, and H. Hwang, J. Electrochem. Soc. **152**, G345 (2005).

[100] F.L. Bregolin, M. Behar, U.S. Sias, and E.C. Moreira, J. Lumin. **131**, 2377 (2011).

[101] U. S. Sias, M. Behar, H. Boudinov, and E. C. Moreira, J. Appl. Phys. 102, 043513 (2007).

[102] N. Nakamura, K. Noda, and Y. Yamauchi, Nucl. Instrum. Meth. B **227**, 299-305 (2005).

[103] S.A. Almeida, S.R.P. Silva, B.J. Sealy, and J.F. Watts, Phil. Mag. Lett. **78**, 319 (1998).

[104] S. Almeida, S. Silva, B. Sealy, and J. Watts, Thin Solid Films **343-344**, 632 (1999).

[105] S.R.P. Silva, S.A. Almeida, and B.J. Sealy, Nucl. Instrum. Meth. B **147**, 388 (1999).

[106] J. Yanagisawa, M. Toda, T. Kitamura, H. Matsumoto, and Y. Akasaka, J. Vac. Sci. Technol. B **23**, 3205 (2005).

[107] J. B. Baxter and E. S. Aydil E S, Appl. Phys. Lett. **86**, 053114 (2005).

[108] X. F. Duan, Y. Huang, Y. Cui, J. F. Wang, and C. M. Lieber, Nature **409**, 66 (2001).

[109] N. Fukata, T. Oshima, T. Tsurui, S. Ito, K. Murakami, Sci. Technol. Adv. Mater. **6,** 628 (2005).

[110] X. Zhao, C. M. Wei, L. Yang, and M. Y. Chou, Phys. Rev. Lett. **92**, 236805 (2004).

[111] G. V. Bianco, M. M. Giangregorio, P. Capezzuto, M. Losurdo, T. H. Kim, A. S. Brown, G. Bruno, Mater Sci Eng **177**, 700 (2012).

[112] J. Westwater, D. P. Gosain, S. Tomiya, S. Usui, and H. Ruda, J. Vac. Sci. Technol. B **15**, 554 (1997).

[113] J. D. Holmes, K. P. Johnston, R. C Doty, and B. A. Korgel, Science **287**, 1471 (2000).

[114] Wu NL

[115] A. Lugstein, M. Steinmair, Y. J. Hyun, G. Hauer, P. Pongratz, and E. Bertagnolli, Nano Lett. **8**, 2310 (2008).

[116] Z. Pan, S. Dai, D. B. Beach, and D. H. Lowndes, Nano Lett. **3**, 1279 (2003).

[117] S. Conesa-Boj, I. Zardo, S. Estrade, Li Wei, Pierre Jean Alet, P. Roca i Cabarrocas, J. R. Morante, F. Peir, A. Fontcuberta i Morral, and J. Arbiol, J. Cryst. Growth **10**, 1534 (2010).

[118] O. Moutanabbir, S. Senz, R. Scholz, M. Alexe, Y. Kim, E. Pippel, Y. Wang, C. Wiethoff, T. Nabbefeld, F. Meyer zu Heringdorf, and M. Horn-von Hoegen, ACS Nano **5**, 1313 (2011).

[119] L. Yu, B. O'Donnell1, P. Alet, S. Conesa-Boj, F. Peir´o, J. Arbiol, and P. Roca i Cabarrocas, Nanotechnology **20**, 225604 (2009).

[120] M. Jeon, Y. Tomitsuka, and K. Kamisako, J. Ind. Eng. Chem. **14**, 836 (2008).

[121] A. Reguer and H. Dallaporta, Mat. Sci. Semicon. Proc. **12**, 44 (2009).

[122] J. Bae, N. N. Kulkarni, J. P. Zhou, J. G. Ekerdt, and C. Shih, J. Cryst. Growth **310**, 4407 (2008).

[123] Yi Cui, Lincoln J. Lauhon, Mark S. Gudiksen, Jianfang Wang, and Charles M. Lieber, Appl. Phys. Lett. **78**, 2214 (2001).

[124] A. Lugstein, M. Steinmair, Y. J. Hyun, G. Hauer, P. Pongratz, and E. Bertagnolli, Nano Lett. **8**, 2310 (2008).

[125] A. Lugstein, M. Steinmair, Y. J. Hyun, G. Hauer, P. Pongratz, and E. Bertagnolli, Nano Lett. **8**, 2310 (

[126] T. I. Kamins, R. S. Williams, Y. Chen, Y. L. Chang, and Y. A. Chang, Appl. Phys. Lett. **76**, 562 (2000).

[127] V. Svrcek and M. Kondo, IEEE Photovoltaics Specialists Conference, 837 (2009).

[128] Z. Zhou, M. L. Steigerwald, R. A. Friesner, and L. Brus, Phys. Rev. B **71**, 245308 (2005).

[129] M. K. Sunkara, S. Sharma, R. Miranda, G. Lian, and E.C. Dickey, Appl. Phys. Lett. **79**, 1546 (2001).

[130] M. Hetzel, A. Lugstein, C. Zeiner, T. Wójcik, P. Pongratz, and E. Bertagnolli, Nanotechnology **22**, 395601 (2011).

[131] I. Zardo, L. Yu, S. Conesa-Boj, S. Estrade, P. J. Alet, J. Roessler, M. Frimmer, P. Roca I Cararrocas, F. Peiro, J. Arbiol, J. R. Morante, and A. Fontcuberta I Morral, Nanotechnology **20**, 155602 (2009).

[132] P. C. Wu, M. Losurdo, T. Kim, M. Giangregorio, G. Bruno, H. O. Everitt, and A. S. Brown, Langmuir **25**, 924 (2009).

[133] P. C. Wu, T. Kim, A. S. Brown, M. Losurdo, G. Bruno et al., Appl. Phys. Lett. **90**, 103119 (2007).

[134] K. F. MacDonald, V. A. Fedotov, S. Pochon, K. J. Ross, G. C. Stevens et al., Appl. Phys. Lett. 80, 1643 (2002).

[135] M. Kolibal, T. Cechal, E. Brandejsova, J. Cechal and T. Sikola, Nanotechnology **19**, 475606 (2008).

[136] M.F. Meléndrez, G. Cárdenas, and J. Arbiol, J. Colloid Interf. Sci. **346**, 279 (2010).

[137] M. Hernandez, M. Cervera, E. Ruiz, J. L. Pau1, J. Piqueras, M. Avella, and J. Jimenez, Nanotechnology **21**, 455602 (2010).

[138] P. Philipp, L. Bischoff, and B. Schmidt, Nanotechnology **23**, 475304 (2012).

[139] S.O. Kucheyev, J.S. Williams, and S. J. Pearton, Mater Sci Eng **33**, 51 (2001).

[140] Vineis C J, Shakouri A, Majumdar A and Kanatzidis M G, Adv. Mater. **22,** 3970 (2010).

Chapter 2

Experimental Procedures

2.1 Overview

This chapter describes the experimental procedures used for the synthesis and characterization of the nanostructures studied in this thesis. For these investigations, amorphous 100 x 100 μm SiN_x membrane windows with thicknesses of 100, 200, or 500 nm (Structure Probe, Inc), similar to that shown in Fig. 2.1, were irradiated with normal-incidence Ga^+ ions using an FEI Nova 200 Nanolab dual-beam FIB system as described in section 2.2. Following irradiation, samples were rapid thermally annealed at 850-900°C for 4 - 28min as described in section 2.3. Transmission electron microscopy (TEM) imaging and electron diffraction were carried out in a JEOL 3011 operating at 300 kV. XEDS mapping and scanning TEM (STEM) imaging was performed in a JEOL 2010 TEM operating at 200 kV. For two-point-probe samples, Si wafers with 500 nm SiN_x (Structure Probe, Inc) or Si wafers with 2 μm SiO_2 and 500 nm SiN_x were irradiated similar to the membrane samples. Photolithography and subsequent metal contact deposition on the wafer based samples was performed in the Michigan SSEL as described in sections 2.7 and 2.8. Sections 2.9 and 2.10 detail the pump-probe setup used in collaboration with the Clarke group at the University of Michigan.

2.2 Focused Ion Beam Irradiation

Many of the SiN_x membrane samples described in this dissertation were raster-scan irradiated with a Ga^+ focused ion beam (FIB). This raster-scan FIB irradiation was done sequentially at 30 keV(dose:~$5x10^{17}$ cm^{-2}), 20 keV(dose:~$5\ x10^{17}$ cm^{-2}), 10 keV(dose: ~$5x10^{17}$ cm^{-2}), and 5 keV(dose: ~$5x10^{17}$ cm^{-2}), for a net dose of ~$2\ x10^{18}$ cm^{-2}. We explored sample fabrication strategies aimed at maximizing the surface layer [Ga], while maintaining the spatial resolution of the FIB. The expected FIB spot size is 25 nm (7nm) at 5 keV (30 keV).[1] In addition, Profile Code (a PC software program that computes Monte Carlo plots of ion implantation profiles) simulations of 30 and 5 keV Ga^+ ions implanted into Si_3N_4, shown in Fig. 2.1, reveal that 5 keV irradiation is predicted to lead to a larger near-surface [Ga] than that of 30 keV irradiation. Some samples were irradiated in a patterned mode, where the pitch is greater than the beam spot diameter. The difference between the raster-scan and patterned mode irradiation is shown in Fig. 2.2.

2.3 Thermal Annealing

The RTA experiments were carried out using a JetFirst – 150 RTA system at the Solid-State Electronic Laboratory (SSEL) of Electrical Engineering and Computer Science Department in the University of Michigan.

Figure 2.3 presents a diagram of the RTA system. During RTA, the sample is supported on a Si wafer held on thin quartz pins in thermal isolation inside a cell containing a controllable gas ambient. A tungsten-halogen lamp heats the sample through transparent windows coupled with highly reflective mirrors. The sample can be heated to ~1000°C for a time interval up to 10 minutes. RTA samples in this thesis were annealed in flowing N_2 gas at 850-900°C for 4 - 28min.

2.4 Transmission Electron Microscopy Sample Preparation

The SiNx membranes used for these experiments were 100 – 500 nm thick, thin enough to be transparent in both the 200 and 300 kV TEMs. No further preparation was required.

2.5 Transmission Electron Microscopy

The evolution of the SiN_x:Ga microstructures was studied using transmission electron microscopy (TEM). We used diffraction contrast imaging, high-resolution TEM (HRTEM), and scanning TEM (STEM), which are described below. All TEM experiments were conducted at the Michigan Electron Microbeam Analysis Laboratory (EMAL), using the JEOL 3011 and 2010F microscopes.

Diffraction contrast TEM imaging was conducted using a JEOL 3011 or 2010F transmission electron microscope operating at 300 and 200 keV, respectively. The

microscope was aligned such that the direct beam and a selected diffracted beam were centered in bright-field and dark-field modes, respectively. A schematic of this alignment is shown in Fig. 2.8. The objective aperture was then inserted to select the direct beam (000) in bright-field mode, while also selecting the diffracted beam (hkl) in dark-field mode. The TEM is then switched back into imaging mode where a bright-field (BF) image is visible in bright-field mode and a dark-field (DF) image is visible in dark-field mode. Only the selected beams will illuminate the image, causing diffracted beams to be bright in their diffracted DF image, while all diffracted areas of the sample will appear dark in the BF image, since only the transmitted (not-diffracted) beam is present. This contrast between the BF and DF images is known as "diffraction contrast". A detailed description of diffraction analysis techniques is presented in Appendix A.

To obtain STEM images, the microscope is initially aligned at 120K magnification. The microscope is then switched into STEM mode using a 1.0 nm probe size. BF images are obtained from a detector that collects beams with minimal scattering. DF images are obtained using a High Angle Annular Dark Field (HAADF) detector that collects beams defected at high angles. Atoms with a larger radius will deflect more electrons at a higher angle, therefore appearing brighter in the HAADF images. This contrast is commonly known as "Z contrast".

To obtain HRTEM images, the sample was tilted towards the nearest zone axis to try to maximize the contrast between the atom columns visible. The contrast visible in these images is due to small phase differences in the transmitted beam due to varying amounts of scattering within the sample. Areas with more scattering, will appear darker, while areas will less scattering will appear brightness, forming contrast known as "phase

contrast". The images were captured with Gatan Digital Micrograph through a CCD camera.

2.6 X-Ray Energy Dispersive Spectroscopy

The chemical composition of various samples was examined qualitatively by X-Ray Energy Dispersive Spectroscopy (XEDS), in a JEOL 2010 TEM operating at 200 keV. During electron beam irradiation, inner-shell electrons in the sample are excited to higher-energy states. Subsequent relaxation to a lower-energy state induces emission of an X-ray with energy equal to the difference between electronic energy levels. These energy levels are characteristic of an atom, and therefore the emitted X-rays are also characteristic of the excited atom. The number of X-rays emitted in a given time can be roughly related to the concentration of that element in the sample. In this TEM system, a Si(Li) diode under reverse bias was used to detect the energies of emitted X-rays.

2.7 Photolithography

Some Si wafer based samples for 2 point probe measurements utilized photolithography for contact deposition. Samples were initially placed on manual spinners and suctioned in place with a vacuum through a hole in the center of the chuck. To increase photoresist adhesion, a couple drops of hexamethyldisilazane (HDMS) were dropped using a plastic dropper onto the center of the sample. Then sample was then spun at 3000 rpm for 45 seconds. Then a few drops of the photoresist, SPR 220, were

dropped onto the sample using another clean dropper. The sample was again spun at 3000 rpm for 45 seconds. The target photoresist thickness after spinning was about 3 μm. The sample was then baked on a hot plate at 150ºC for 90 seconds.

The next segment of the processing is the exposure to light on the GCA AS200 AutoStep. The mask used is chrome mask on a soda lime glass substrate (designed by us and ordered from Photo Sciences Inc.). Figure 2.4 shows a sketch of the mask used, which is two 1 mm by 1mm squares with a 3 μm gap between them. The two squares will be exposed by the stepper and eventually become the contacts. A blank 4" Si wafer was used to roughly align the stepper. Then the wafer is removed and replaced with the sample. The sample is then aligned to the alignment marks and exposed. After exposure, the sample is again baked on a hot plate at 150ºC for 90 seconds.

The sample is then developed in MF-319 for 50 seconds, followed by a 5 minute deionized water rinse. The sample is then examined in an optical microscope to see if development is complete. If development is not complete, the sample is put in a MF-319 bath for an additional 10 seconds. These last two steps are repeated until development is completed. The sample is now ready for metal deposition.

2.8 Metal Deposition

Metal was deposited by either evaporation or sputtering. Evaporation was done in either the EnerJet Evaporator or the SJ-20 Evaporator in the Michigan SSEL. Au and Al were evaporated at a rate of 10 Å/sec. Sputtering was done in the Lab18_02 in the

Michigan SSEL. Al and Ni were sputtered at a rate of ~2.5 and ~3.5 Å/sec, respectively. Vacuum during all deposition was ~2e-6 Torr.

2.9 Time-Domain Pump-Probe Thermoreflectance Measurements

Pump-probe measurements were performed using a fs dual-laser system with lasers based on Er-doped fiber. A diagram of the transducers and the pump and probe lasers incident on a sample is shown in Fig. 2.5. Individual lasers provide output pulses of 0.8 nJ energy, 80 fs pulse duration at a fundamental wavelength of 1550 nm. One laser (slave) is locked to the other (master) using synchronization electronics (SE) that controls the frequency of the slave laser by adding or subtracting a fixed frequency offset. This procedure assures that the slave laser is locked to the repetition rate of the master laser at fixed frequency offset difference. The repetition rates for the lasers were ~ 100 MHz and the offset frequency is between 0.2 – 7 kHz. Maintaining this frequency offset allows for the use of asynchronous optical sampling (ASOPS), a technique used for performing pump-probe measurements.[2,3,4,5] Using a second harmonic generation module, the slave laser also produces pulses at 780 nm wavelength with 150 fs duration, which was used as the probe laser.[5] The master laser at a 1550 nm wavelength, 100 fs pulse duration and at 0.4 nJ pulse energy was used as the pump laser. Fig. 2.6 presents a schematic of this setup including the lasers, key optical components, and detectors. The 780 nm laser beam was split prior to reaching the sample using a beam splitter in order to obtain a reference signal. This reference signal is compared with the probe beam reflection on the sample using a balanced detector in order to reduce background noise. The maximum temporal

scanning interval is the inverse of the laser repetition rate or 10 ns. The temporal resolution of the system is optimized by using a real-time optical triggering method. As shown in Fig. 2.6, an optical cross-correlator combines a portion of the master beam reflected using a beam splitter with the fundamental wavelength from the slave laser. These two beams are focused with a parabolic mirror and sent through a sum frequency generator to produce a cross-correlation beam at 780 nm, which is incident on a detector to provide a trigger signal for the data acquisition electronics.

2.10 Pump-Probe Measurements of Acoustic Propagation

The acoustic measurements used the lasers described in section 2.9 and a reflection geometry where pump and probe beams are applied on the same surface (side) of the sample. A diagram of another experimental configuration suitable for acoustic propagation studies is shown in Fig. 2.7, which uses pump and probe beams applied on opposite sides of the sample to monitor phonon transmission through the sample. Both pump and probe beam are perpendicular to the sample, which necessitates the use of a beam splitter to capture the probe signal in the detector. The incident beam goes through the beam-splitter and reflects off the sample, returning to be reflected by the beam-splitter into the detector.

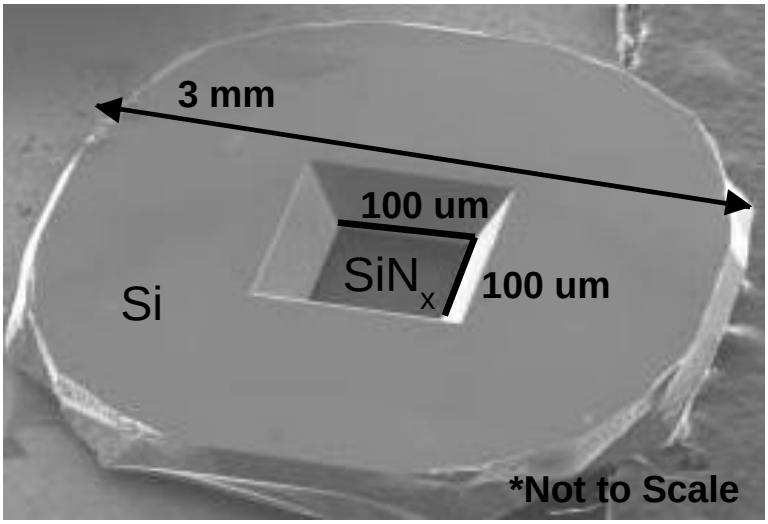

http://www.2spi.com/catalog/instruments/silicon-nitride.php

Fig. 2.1 Picture of a SiNx membrane from Structure Probe Inc. similar to that used for the experiments. Membranes used for our experiments had a 100 x 100 μm window of SiNx in the center of a 3 mm diameter Si wafer frame. We used membranes with thicknesses of 100, 200, or 500 nm.

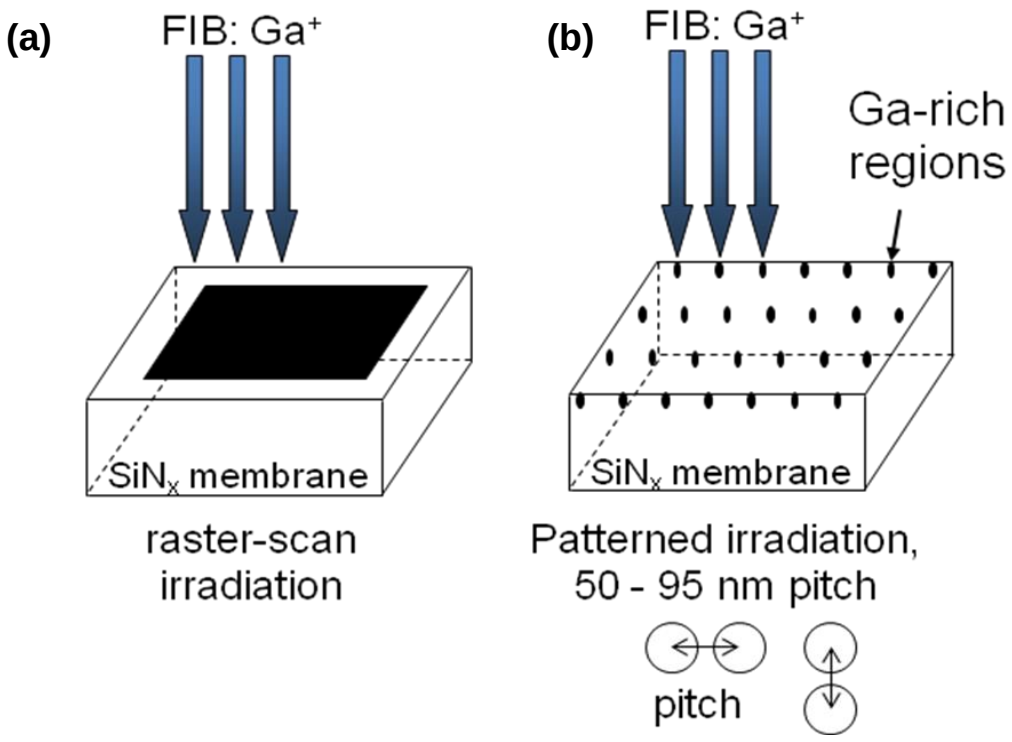

Fig. 2.2 Ion implantation was done either by (a) raster scan irradiation over a larger area with pitch = ½ beam spot diameter or by (b) patterned irradiation, where the pitch > beam spot diameter.

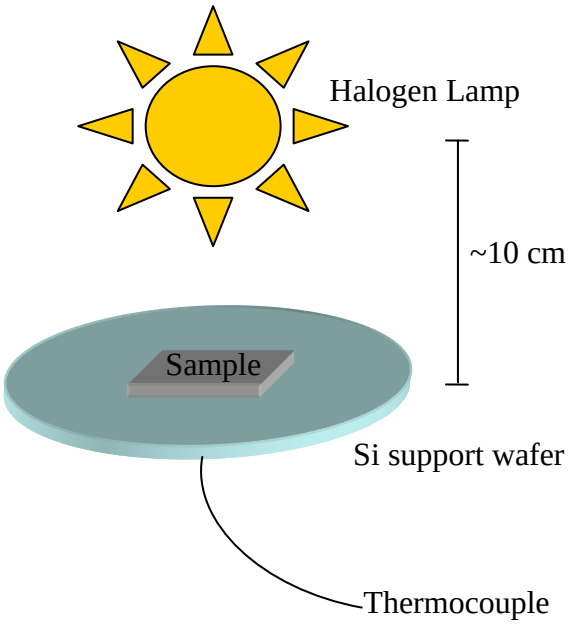

Fig. 2.3 Schematic of the rapid thermal annealing setup. The sample rests on a silicon wafer with a thermocouple contact on the center of the underside. The chamber is purged with flowing nitrogen gas while the sample is heated by a halogen lamp housed inside a quartz window.

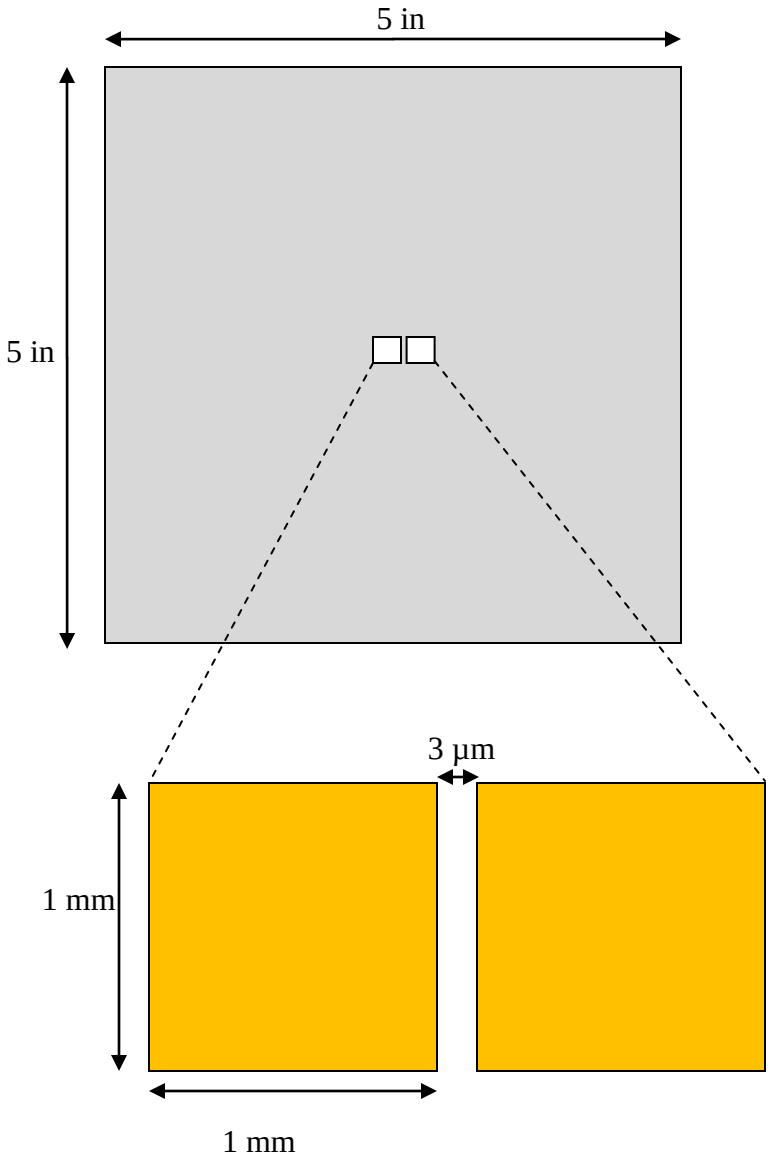

Fig. 2.4 Diagram of the mask used for photolithography. The mask consists of two 1 x 1 mm squares with a 3µm gap between. During development, the photoresist in the two squares will be removed, leaving open the location where the two metal contacts will be deposited.

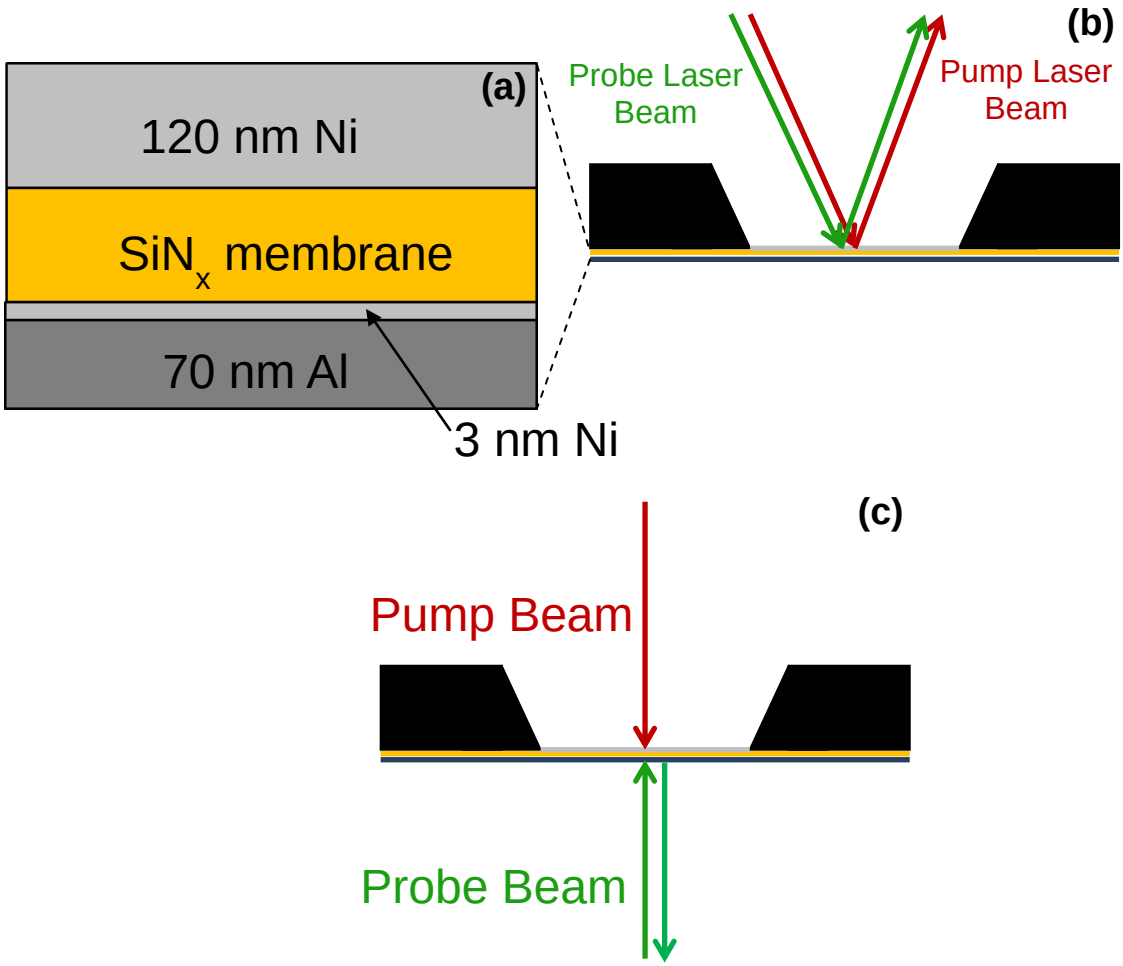

Fig. 2.5 Diagram of (a) transducers used for pump probe experiments and the lasers used for the pump and probe lasers incident on a sample in (b) reflection geometry and (c) transmission geometry.

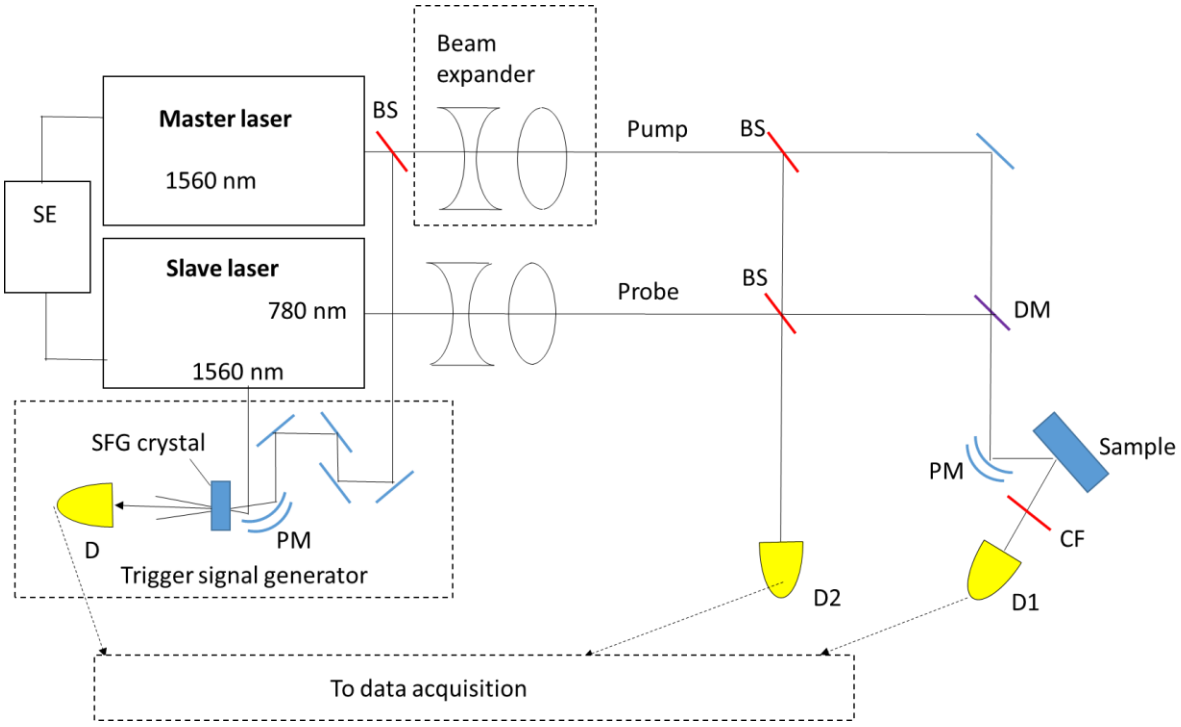

Fig. 2.6 Schematic of the time-domain pump-probe thermoreflectance setup: SE – Synchronization electronics; BS – beam splitter; PM – parabolic mirror; D, D1, D2 – detectors; SFG – sum-frequency generation; DM – dichroic mirror; CF – color filter

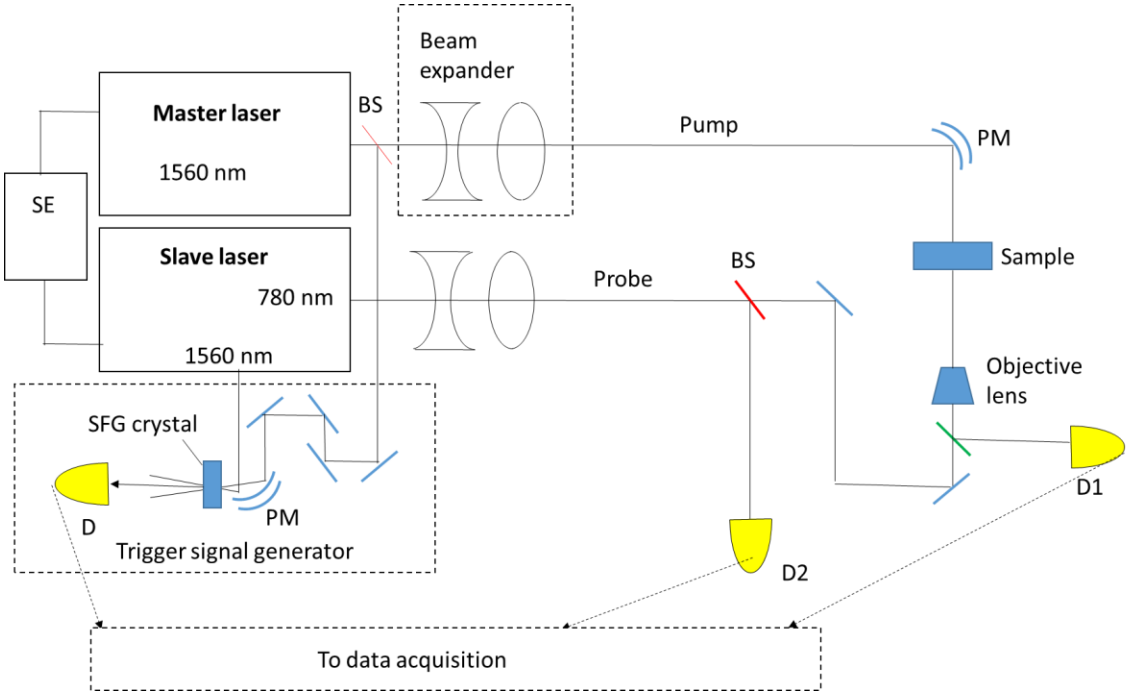

Fig. 2.7 Schematic of the transmission pump-probe setup. SE – Synchronization electronics; BS – beam splitter; PM – parabolic mirror; D, D1, D2 – detectors; SFG – sum-frequency generation.

2.11 References

[1] FEI Company, UHV Magnum Ion Column with BDS-200 User's Guide, (FEI Company, Hillsboro, OR, 2006), pp. 7-22–7-24.

[2] P. A. Elzinga, F. E. Lytle, Y. Jiang, G. B. King, and N. M. Laurendeau, Appl. Spectrosc. **41**, 2 (1987).

[3]A. F. Bartels, F. Hudert, C. Janke, T. Dekorsy, and K. Kohler, Appl. Phys. Lett. **88**, 041117 (2006).

[4] S. Adachi, S. Takeyama, and Y. Takagi, Opt. Commun. **117**, 71 (1995).

[5] V. A. Stoica, Y.Sheu, D. A. Reis, and R. Clarke, Opt. Express **16**, 2322 (2008).

Chapter 3

Formation Mechanisms of Embedded Nanocrystals in SiN_x

3.1 Overview

This chapter describes our investigations of the formation of embedded nanocrystals (NCs) as well as Ga-rich fractal morphologies using a range of high dose Ga^+ focused-ion beam irradiation of SiN_x membranes, followed by rapid thermal annealing (RTA). This chapter begins with background on Si NC formation and applications. We consider Profile Code simulations of Ga^+ implantation into SiN_x and then detail our experiments of FIB implantation into SiN_x membranes and subsequent RTA. We then discuss our main findings, namely the effect of redeposition on NC formation. During irradiation, redeposition is enhanced by developing side walls, leading to enhanced near-surface [Ga] and [Si]. Subsequent RTA leads to the formation of Si and Ga NCs embedded in SiN_x. When the ratio of the irradiated area to the sidewall area is increased, redeposition is limited, and SiN_x and GaN NCs are also apparent. We also discuss the catalytic effect of Ga on Si nucleation and growth. The chapter concludes with a summary.

3.2 Background

Due to the size dependence of their band gap energy, light emission, and free carrier confinement, Si NCs are promising for tandem solar cells,[1] fiber amplifiers,[2] and flash memory,[3] respectively. For solar cells, doping of Si NCs (P, B)[4,5] is essential, while for fiber amplifiers, Er doping has been shown to increase optical amplification.[6] For flash memory applications, B doping has been shown to enhance the threshold voltage shift.[7] Since Ga has been used as both a dopant of Si NCs[8,9] and as a catalyst for Si nanowire growth,[10,11] it may provide an opportunity for simultaneous doping and catalysis of Si NCs. Co-sputtering[12,13] and plasma-enhanced chemical vapor deposition (PECVD)[14,15] of Si-rich SiO_2 or SiN_x, followed by annealing, have been used to nucleate embedded Si NCs throughout the film thickness. Recently, Si irradiation in conjunction with annealing, has been used to fabricate Si NCs at select depths within both SiO_2 and SiN_x.[16,17,18,19,20,21] Local regions of excess Si have also been achieved by breaking Si-N bonds in SiN_x using Ti^+, B^+, and Ga^+ ions.[22,23,24,25,26] Ga^+ implantation into N-rich ($x > 1.5$) α-SiN_x:H_y leads to preferential Ga displacement of Si, resulting in Ga-N, Ga-Ga, and Si-H bond formation.[23,24,25] In another report, 0.06 to 5 keV Ga^+ implantation into SiN induces the formation of an amorphous GaN surface layer,[26] subsequently used for seeding the epitaxial growth of GaN.[27] Although the ion-induced formation of Si NCs in SiN_x has been examined, the mechanisms for their Ga induced nucleation and growth have yet to be reported.[23-27] Here, we report on the formation mechanisms of embedded NCs using Ga^+ focused ion-beam (FIB) irradiation into SiN_x, followed by RTA. We

discuss the effect of redeposition on NC formation and the catalytic effect of Ga on Si NC nucleation and growth.

3.3 Simulations

To explore strategies for maximizing the [Ga] in a minimal volume, we considered predictions of the depth profile of implanted Ga using Ion Beam Profile Code simulations. Profile Code simulations use empirical formulas for concentration profiles based upon results from Stopping and Range of Ions in Matter (SRIM) Monte Carlo simulations and experimental data to calculate implantation profiles, as detailed in Appendix E.[28] We adjusted the sputtering coefficients in Profile Code for 30 and 5 keV implantations to 1.2 and 0.39, respectively, based on AFM measurements detailed in Appendix E. Figure 3.1 shows plots of ion concentration vs. depth for both the 5 and 30 keV ions. These plots reveal that the 5 keV irradiation is predicted to lead to a ~50% higher near-surface [Ga] than that of 30 keV irradiation. To maintain the spatial resolution of the FIB, we also explored sample fabrication strategies aimed at maximizing the [Ga] in a minimal volume. The expected FIB spot size is 25 nm (7nm) at 5 keV (30 keV).[29] To accomplish this, we used a masking layer method that combines the higher near-surface [Ga] from the 5 keV implantation with the precision of the 30 keV spatial resolution, as detailed in section 3.4.

3.4 Experiments

For these investigations, amorphous SiN_x membrane windows (Structure Probe, Inc) were irradiated with normal-incidence Ga^+ ions using an FEI Nova 200 Nanolab dual-beam FIB system. Several SiN_x membranes were irradiated using 5-30 keV Ga^+ ions, with net doses of $1.7x10^{18}$ cm^{-2} to $8.3x10^{18}$ cm^{-2}, using a continuous raster scan mode, where p (pitch) = ½ d (spot size), and/ or a "patterned" mode, with p = 100 nm and d = 35 nm. Following FIB irradiation, samples were rapid thermal annealed in 1000 sccm N_2 environment for 1-28 minutes at 900˚C.[30] Brightfield (BF) and darkfield (DF) transmission electron microscopy (TEM) imaging and selected area diffraction (SAD) were carried out in a JEOL 3011 (operating at 300 keV) and in a JEOL 2010F (operating at 200 keV). For SAD, apertures were used to select regions with ~0.1 or ~2 µm diameter. Therefore, samples include the following: "Multi-E unpatterned" were raster-scan FIB irradiated sequentially at 30 keV(dose:~$5x10^{17}$ cm^{-2}), 20 keV(dose:~5 $x10^{17}$ cm^{-2}), 10 keV(dose: ~$5x10^{17}$ cm^{-2}), and 5 keV(dose: ~$5x10^{17}$ cm^{-2}), for a net dose of ~2 $x10^{18}$ cm^{-2}, followed by 28 min of RTA. "High E patterned" were patterned at 30 keV (doses: $1.7x10^{18}$ cm^{-2} to $8.3x10^{18}$ cm^{-2}). "Multi-E patterned w/ mask" samples were prepared as follows. First, 0.5 µm of PECVD SiO_2 was deposited onto a SiN_x membrane, which was then FIB patterned at 30keV Ga^+ (dose: ~$3x10^{18}$ cm^{-2}), followed by 5keV Ga^+ raster-scan FIB irradiation (dose: ~5 $x10^{17}$ cm^{-2}). Finally, a layer of 0.5 µm SiO_2 was deposited and subsequently etched in buffered HF for 3 min, leaving a patterned area with increased local [Ga] near the SiN_x surface. A diagram of this process is shown in Fig. 3.2.

3.5 Raster-Scan Irradiation of SiN_x

3.5.1 Nanocrystal Formation: Ga; Si; Si_3N_4; GaN

For the "multi-E unpatterned" sample, we examined SAD patterns from across the sample using apertures which select areas with ~0.1 μm (Figs. 3.3(a), 3.3(c), and 3.3(d)) and ~2 μm (Fig. 3.3(b)) diameters. In Fig. 3.3(a), d-spacings of 2.43 +/- 0.04 and 2.78 +/- 0.04 Å are apparent, corresponding to within 1% of the (101) and (100) interplanar spacings of wurtzite (WZ) GaN (triangles). Other d-spacings of 3.78 +/- 0.04, 2.67 +/- 0.04, and 1.89 +/- 0.04 Å from 3 different NCs (squares, circles, and diamonds) are apparent; these correspond to within 1% of the (110), (101), and (220) interplanar spacings of Si_3N_4. The SAD pattern in Fig. 3.3(b) contains polycrystalline rings with d-spacings of 3.96 +/- 0.04 Å, 3.15 +/- 0.04 Å, 2.44 +/- 0.04 Å, and 1.96 +/- 0.04 Å; corresponding to within 2% of the (110) and (100) Si_3N_4, (111) Si, (101) WZ GaN, and (220) Si and (220) Si_3N_4 reflections, respectively (Table 3.1).[31] In Fig. 3.3(c), d-spacings of 4.21 +/- 0.04 Å and 2.65 +/- 0.04 Å are observed, corresponding to within 2% of the (021), (diamond) and (400), (square) interplanar spacings of Ga. The SAD pattern in Fig. 3.3(d) contains a spot pattern with d-spacings of 3.92 +/- 0.04 Å and 3.34 +/- 0.04 Å, corresponding to within 3% of the (110) and (200) interplanar spacings of Si_3N_4. Collectively, these SAD patterns indicate the formation of Ga, Si, GaN, and Si_3N_4 NCs within SiN_x. The formation of Ga-Ga, Ga-N, and Si-H bonds, but not Si-Si bonds, has been reported for Ga implantation into N-rich α-SiN_x:H_y.[23,24,25] Si-Si bonds have been achieved by breaking Si-N bonds using Ti^+ or B^+ implantation into Si_3N_4.[22] Our SiN_x is Si-rich, similar to that of Si implanted Si_3N_4,[18,19,20] which induces the formation of Si NCs upon annealing.

To further examine these nanostructures, we employed diffraction contrast TEM and high-angle annular dark-field (HAADF) scanning TEM (STEM). Figure 3.4(a) (3.4(b)) presents a dark-field diffraction contrast (HAADF) TEM (STEM) image, with a crystal exhibiting diffraction contrast in Fig. 3.4(a) encircled. The dark-field image in Fig. 3.4(a) was obtained using the Si_3N_4 110 beam. Presented in Figs. 3.5(a), 3.5(c), and 3.5(b) are HAADF STEM images of the "multi-E unpatterned" sample collected from the edge, center, and an intermediate location between the edge and center of the implanted SiN_x membrane window, respectively as indicated in Fig. 3.5(d). These images show a complex microstructure with larger (~100s of nm) brighter areas, typically surrounded by larger darker areas. Within these larger brighter areas are smaller (~30nm) brighter and darker features. Using the line-cut indicated in Fig. 3.5(b), the spatial profiles of Si, N, and Ga concentration are shown in Fig. 3.5(e). Interestingly, it appears that the larger brighter areas are Ga- and N-rich, while the darker areas are Si-rich. An investigation across the entire membrane reveals that most of the Si-rich dark regions are near the edges of the SiN_x membrane window, which is framed by Si. Thus, the excess Si near the edges is likely due to redeposition from the Si frames. Most of the larger Ga- and N-rich brighter regions contain smaller bright (24 +/- 8 nm) and dark (35 +/- 5 nm) NCs, which are expected to be Ga- and Si-rich, respectively (Fig. 3.5(a)). Combined, these images reveal that the Si_3N_4 diffraction spots correspond to the brighter Ga- and N-rich areas, suggesting that the Si_3N_4 crystals are Ga-doped. The smaller Si-rich NCs within these Si_3N_4 crystals may be precipitates due to the Si-rich composition of the SiN_x membrane

relative to Si_3N_4. The formation of Ga-rich precipitates within these Si_3N_4 crystals is likely due to the high implanted Ga^+ dose in their vicinity.

3.5.2 Ga-rich Fractal Formation

We now consider the effect of dose on the nanostructure formation in the raster-scan irradiated samples. Figure 3.6 presents HAADF STEM images of samples with a dose of (a) 1.14, (b) 1.22, (c) 1.29, (d) 1.37, (e) 1.45, (f) 1.52, (g) 1.60, (h) 1.67, and (i) $1.75 \times 10^{18}/cm^2$ following RTA for 16 min. Due to Z-contrast, i.e. electron scattering that scales with atomic number, the HAADF detector collects more electrons from Ga atoms than from Si and N, leading to Ga-rich regions that appear brighter in the STEM images. These bright Ga-rich regions in Figs. 3.6(a) – 3.6(i) appear self-similar, with multiple side braches, suggesting a fractal geometry. Using the footprint of the Ga-rich fractals, we quantified the Ga surface coverage as a function of dose. As shown in Fig. 3.7(a), the Ga surface coverage increases with ion dose. The Ga-rich structures in Figs. 3.6(a) – 3.6(f) have many thin, long arms, while the structures in Figs. 3.6(g) – 3.6(i) feature short, thick arms. Thus, a morphological transition from multiple thin, long arms to fewer short, thick arms occurs at a dose of ~ $1.6 \times 10^{18}/cm^2$. For example, typical thin (~40 nm) and thick (~100 nm) arms are identified by arrows in Figs. 3.6(a) and 3.6(g), respectively. To quantify this transition, we consider the fractal dimension, D_f, where:

$$D_f = -\ln(n)/\ln(\epsilon) \qquad (3.1)$$

where n is the minimum number of open sets of diameter ϵ needed to include the entire fractal set, as described in Appendix C.3. D_f ranges from 1.0 for a linear geometry to 2.0 for a completely filled, uniform 2D plane. For complex branched fractals, D_f lies

between 1.0 and 2.0. For example, for multiple-branched fractal aggregates which fill space nearly uniformly during diffusion limited aggregation (DLA), D_f is ~1.71.[32,33] Interestingly, for our studies as shown in Fig. 3.7(b), D_f increases with surface coverage, from ~1.65 to ~1.75, similar those of GaN fractals on Al_2O_3[34] and Ga_2O_3 fractals on stainless-steel.[35] Evidently, as the surface coverage increases, the morphology transitions from DLA-like to a completely, uniform 2D plane.

To determine the crystallinity in the regions with fractal morphology, we examined SAD patterns collected using apertures which select areas with ~2 μm diameter, such as the circular region indicated in Fig. 3.6 (e). The corresponding SAD patterns in Fig. 3.7(c) contain polycrystalline rings with d-spacings of 2.48 +/- 0.04 and 4.05 +/- 0.04 Å, corresponding to within 3% of GaN (110) or Ga (331) and Si_3N_4 (101) or (110) interplanar spacings, respectively. These interplanar spacings correspond to the strongest reflections from GaN, Ga, and Si_3N_4 crystals, respectively. This SAD pattern suggests the presence of randomly-oriented GaN, Ga, and Si_3N_4 NCs within an amorphous matrix, similar to that observed for the "multi-E unpatterned" sample in section 3.4.1. Thus, the fractals consist of NCs within an amorphous matrix, a microstructure characteristic of random successive nucleation (RSN),[36] to be described next.

In RSN, heat released during crystallization (i.e. latent heat of crystallization) induces local nucleation and fractal growth. Since the thermal diffusivity in Si_3N_4 (~$2x10^{-6}$ m^2/s)[37] is several orders of magnitude larger than the expected Ga diffusivity (~$1x10^{-18}$ m^2/s for Ga diffusivity in c-Si[38]), successive nucleation of individual NCs in a branched fractal geometry during annealing is expected to be energetically favorable.[36]

In section 4.4, Ga NPs as small as 3 nm in diameter were discussed. It is likely that the fractal branches are composed of many small nuclei. Since the fractal branches range from ~40 to ~100 nm in thickness, it is likely that the transition in branch thickness is due to an increase in nucleation sites with ion dose. A similar branch thickness transition was recently reported for Ge-rich fractals in a Au matrix.[36]

3.6 Patterned Irradiation of SiN_x

3.6.1 Ga and Si Nanocrystal Formation

We now consider the effects of redeposition on NC formation. Fig. 3.8(a) presents an overview BF TEM image of the "high-E patterned" sample after 8 min of RTA, while Figs. 3.8(b) and 3.8(c) present overview BF TEM images of the "multi-E patterned w/ mask" sample following RTA for 8 min and 16 min, respectively. For each overview image, a high resolution (HR) TEM of an implanted area, designated by a rectangle, and typical corresponding SAD patterns are shown in Figs. 3.8(g) - 3.8(i). For the "high-E patterned" sample, NCs are not observed in the HRTEM (Fig. 3.8(d)), as further revealed by the amorphous SAD in Fig. 3.8(g). For the "multi-E patterned w/ mask" sample, following 8 min RTA, crystallites with average diameters of ~5 nm were observed within the implanted area, as shown in Fig. 3.8(e). Following 16 min RTA, the NCs within the implanted areas have coalesced into 21 +/- 6 nm diameter Si NCs (Fig. 3.8(f)). Additionally, 13 +/- 4 nm diameter regions of significant Z-contrast indicate the formation of NCs outside the implanted areas (Fig. 3.8(c)). To identify the NCs, we

consider the SAD spots in Fig. 3.8(i), with d-spacings of 1.943 +/- 0.04 Å, 2.745 +/- 0.04 Å, 2.441 +/- 0.04 Å; corresponding to within 3% of the interplanar spacings of (220) Si, (330) Ga, and (331) Ga (Table I). It is interesting to note that SiN_x and WZ GaN NCs are only observed in the "multi-E unpatterned" samples, and not in this "multi-E patterned w/ mask" sample. During irradiation, redeposition is enhanced by developing side walls, leading to enhanced near-surface [Ga] and [Si], while N likely escapes as N_2.[39] A diagram of these redeposition effects in shown in Fig. 3.9. Similar redeposition effects were reported by Yamaguchi *et. al.*[40] for Ga FIB implantation into Si. Thus, for the "multi-E unpatterned" samples with higher ratios of the scanned to side wall area, redeposition is less significant, leading to a higher [N], thereby enabling the nucleation of GaN and SiN_x NCs. These GaN NCs are likely formed by homogeneous nucleation and growth processes during annealing, similar to the case of GaN NC nucleation in N^+ implanted GaAs,[41,42] recently described in terms of a TTT diagram.[43] In our case, it is likely that GaN NCs nucleated in the zincblende form and transformed to the WZ phase during the 28 min of RTA at 900˚C.

3.6.2 Catalytic Effects of Ga

We now discuss the influence of excess near-surface Ga on NC formation. It is interesting to note that NCs are observed in the "multi-E patterned w/ mask" sample, where [Ga] is higher, but not in the "high E patterned" sample, suggesting that Ga is functioning as a catalyst for Si NC formation. For Si-ion implanted SiN_x, Si NCs < 10 nm diameter with a density up to ~$2x10^4$ μm^{-2} were reported after subsequent annealing

at 350˚C to 950˚C for 30 to 60 min.[18,20] In contrast, Ga-ion induced Si NCs from the "multi-E patterned w/ mask" sample were ~5nm (~20nm) with a density of ~$8x10^3$ μm^{-2} (~$2x10^4$ μm^{-2}) after 8 min (16 min) of annealing, as shown in Fig. 3.8(e) (Fig. 3.8(f)), suggesting Ga-induced catalysis of Si NC nucleation and growth.

We now discuss the influence of excess Ga on NC formation through a comparison of "low E patterned" and "high E patterned" samples. Figure 3.10 presents (a) a BF image, (b) a corresponding DF image, and (c) SAD pattern collected from the "low E patterned" sample following 4 min of RTA at 900˚C. The lighter areas in Fig. 3.9(a) are the implanted areas, while the darker areas are likely due to the presence of embedded Ga-rich NCs. Larger (smaller) 23+/- 5 nm (7 +/- 2 nm) NCs are present inside (outside) the implanted areas. For example, the region circled in both the BF (Fig. 3.10(a)) and the DF (Fig. 3.10(b)) images, is likely a NC. The corresponding SAD patterned in Fig. 3.10(c) contains spotty rings, with d-spacings of 3.158 +/- 0.04 Å, 1.963 +/- 0.04 Å, and 1.577 +/- 0.04 Å; corresponding to within 1% of the (111), (220), and (222) interplanar spacings of Si (Table I). In addition, the dark hue (Z-contrast) present in Fig. 3.10(a) suggests the presence of Ga in these Si NCs, making them Si_xGa_{1-x}. It is interesting to note that NCs are observed in the "low E patterned" sample but not in the "high E patterned" sample, where [Ga] is higher, suggesting that Ga is function as a catalyst for Si NC formation. This catalytic effect is further revealed by comparing the NC sizes within the "low E patterned w/out mask" sample. Larger Si NCs (23 +/- 5 nm) are only present in the patterned spots while smaller NCs (7 +/- 2 nm) are present throughout the sample (Fig. 3.10(b)). Both sizes of Si NCs have undergone the same RTA, suggesting a higher growth rate in the implanted spots compared to the matrix.

This difference may be the result of irradiation damage and/or increased [Ga], where the increased [Ga] may be due to the collection of surface Ga in the topographical pits during RTA and/or from the selective irradiation of Ga into the patterned spots. This catalytic effect has been attributed to the low temp (~29.8 ˚C) eutectic Ga forms with Si,[44] allowing for Si precipitation from a Ga–Si alloy at low temperatures, and has also been observed for Si nanowire growth.[90,91,45,46] Thus, Ga enhances nucleation and growth of Si NCs.

3.7 Conclusions

In summary, we have investigated the formation of embedded NCs in SiN_x using Ga+ focused-ion beam irradiation of SiN_x membranes, followed by rapid thermal annealing (RTA). During irradiation, redeposition is enhanced by developing side walls, leading to enhanced near-surface [Ga] and [Si]. Subsequent RTA leads to the formation of Si and Ga NCs embedded in SiN_x. Ga functions as a catalyst for Si nucleation and growth, potentially reducing the annealing time required for Si NC formation. For samples with higher ratios of the scanned to side wall area, redeposition is less significant, leading to higher [N], thereby enabling the nucleation of GaN and SiN_x NCs, both of which may facilitate the integration of GaN-based optoelectronics with Si substrates.[26,47] When the irradiation dose is decreased, Ga-rich fractals are apparent, with surface coverage and fractal dimension dependent on irradiation dose.

d-Spacing (Å) (measured)		Powder Diffraction Standard (Å)			
multi-E patterned w/ mask	multi-E unpatterned	Si (hkl)	WZ GaN (hkl)	Ga (hkl)	SiN (hkl)
					4.309 (101)
	4.21 +/- 0.04				3.876 (110)
	3.916 +/- 0.04				3.357 (200)
	3.344 +/- 0.04				
3.136 +/- 0.04	3.148 +/- 0.04	3.135 (111)			
2.745 +/- 0.04	2.78 +/- 0.04		2.756 (100)	2.78 (330)	
	2.65 +/- 0.04		2.589 (002)	2.62 (150)	
2.441 +/- 0.04	2.43 +/- 0.04		2.433 (101)	2.45 (331)	
2.25 +/- 0.04				2.23 (421)	
1.943 +/- 0.04	1.965 +/- 0.04	1.920 (220)		1.93 (441)	1.938 (220)
1.57 +/- 0.04		1.568 (222)			
1.121 +/- 0.04		1.109 (422)			

Table 3.1 Interplanar spacings of samples “multi-E patterned w/ mask” and “multi-E unpatterned” measured by SAD, in comparison to powder diffraction standards (see Ref. 30).

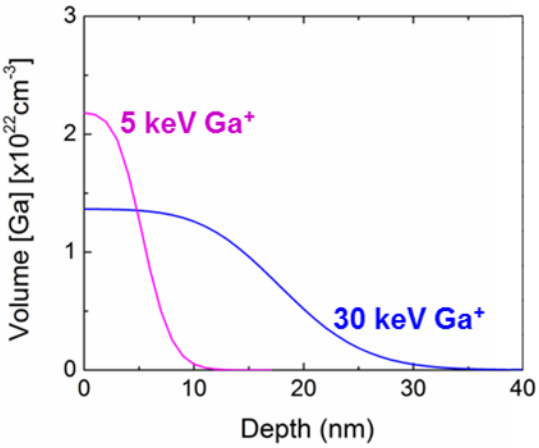

Fig. 3.1 Profile Code simulations of Ga^+ ion implantation into Si_3N_4 at 5 keV, $5e17^{-2}$ dose and 30 keV, $1.7e18^{-2}$ dose.

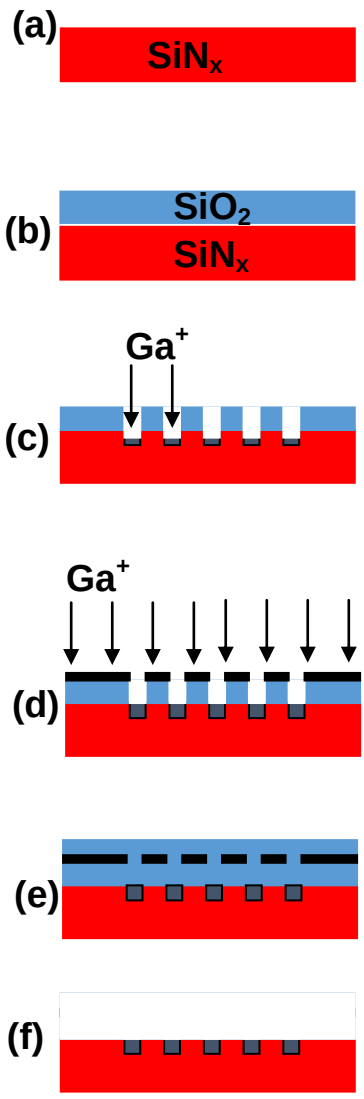

Fig. 3.2 Diagram of processing used to increase local [Ga] through the use of a SiO_2 masking layer. (b) First, 0.5 µm of PECVD SiO_2 was deposited onto a SiN_x membrane, which was then (c) FIB patterned at 30keV Ga^+ (dose: ~3x10^{18} cm^{-2}), followed by (d) 5keV Ga^+ raster-scan FIB irradiation (dose: ~5 x10^{17} cm^{-2}). (e) Finally, a layer of 0.5 µm SiO_2 was deposited and subsequently (f) etched in buffered HF for 3 min, leaving a patterned area with increased local [Ga] near the SiN_x surface.

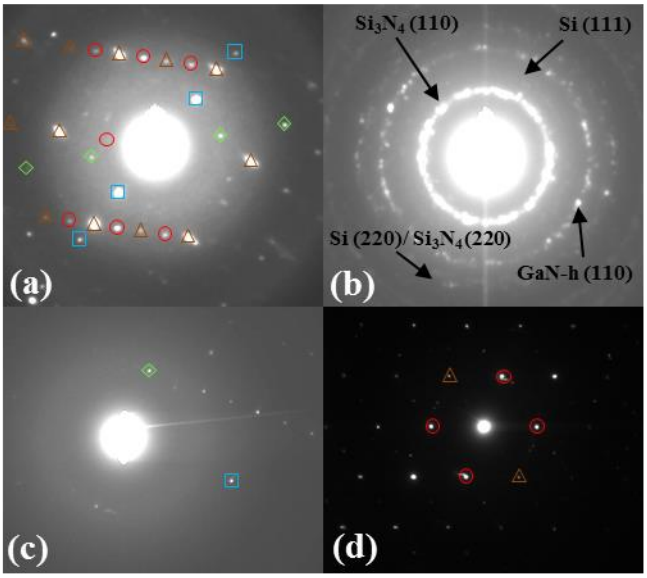

Fig. 3.3 Diffraction in (a) is identified as WZ GaN (triangles) and Si_3N_4 (squares, circles, and diamonds). The SAD pattern in (b) contains polycrystalline rings with spacings corresponding to within 2% of the (111) and (220) Si, (101) WZ GaN, and (110) and (220) Si_3N_4 reflections (Table 3.1). The SAD pattern in (c) contains a spot pattern from Ga, where a diamond marks the (021) and a square the (400) type reflection. The SAD pattern in (d) contains a spot pattern from Si_3N_4, where circles mark (110) and triangles the (200) type reflections.

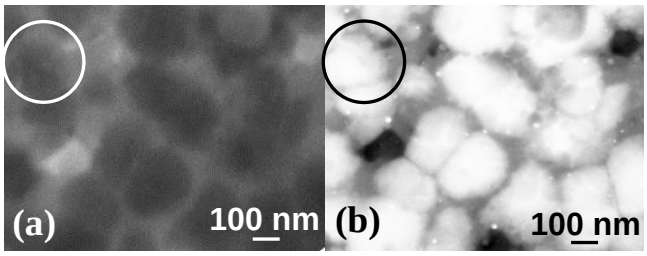

Fig. 3.4 (a) Diffraction contrast and (b) HAADF of the same encircled Si_3N_4 NC suggest that the NC is Ga doped.

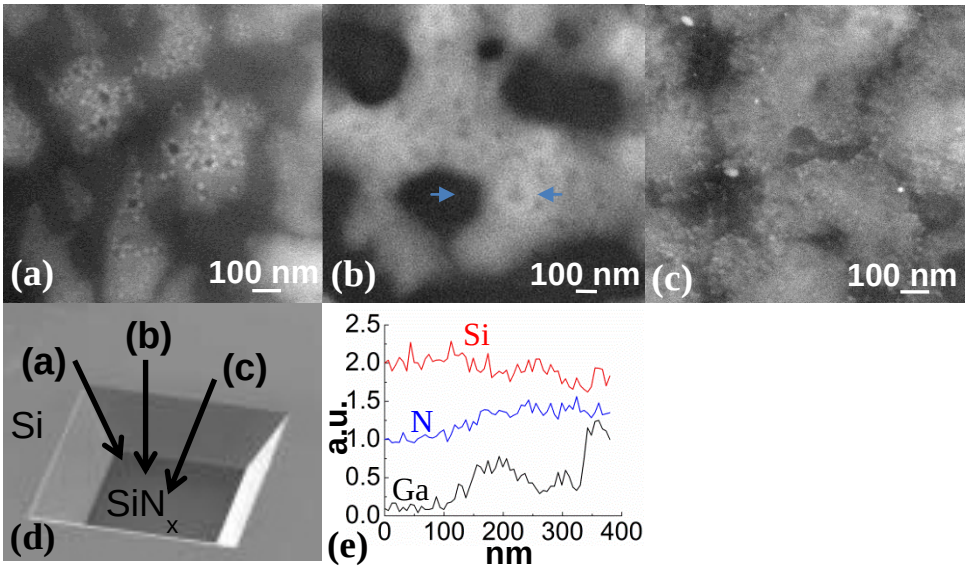

Fig. 3.5 (a), (b), and (c) are high angle annular DF (HAADF) STEM images collected from the edge, center, and in-between the edge and center, respectively, as shown in (d) of the implanted SiN_x membrane window of the "multi-E unpatterned" sample. Using the line-cut indicated in (b), the spatial profiles of Si, N, and Ga concentration are shown in (e).

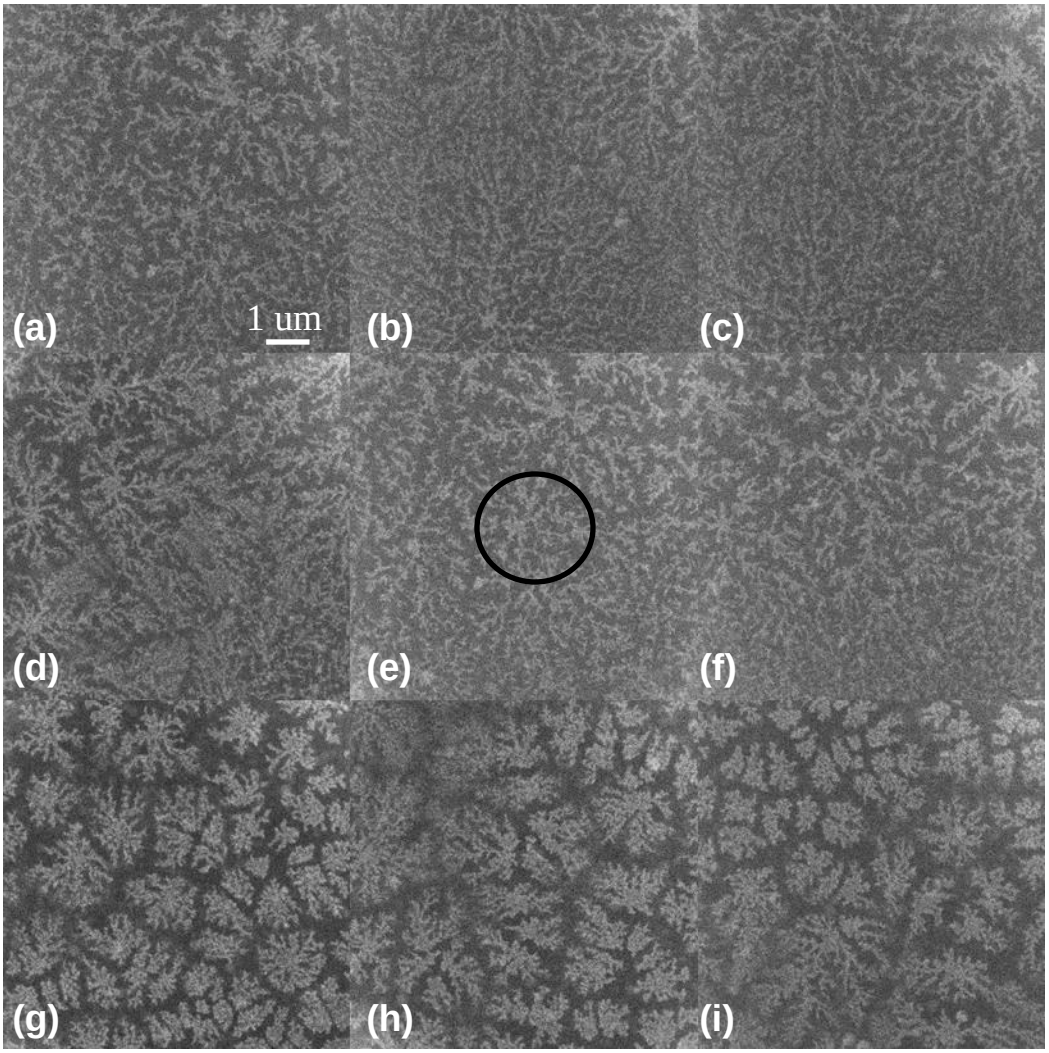

Fig. 3.6 HAADF STEM images of samples with a dose of (a) 1.14, (b) 1.22, (c) 1.29, (d) 1.37, (e) 1.45, (f) 1.52, (g) 1.60, (h) 1.67, and (i) $1.75 \times 10^{18}/cm^2$ following RTA for 16 min.

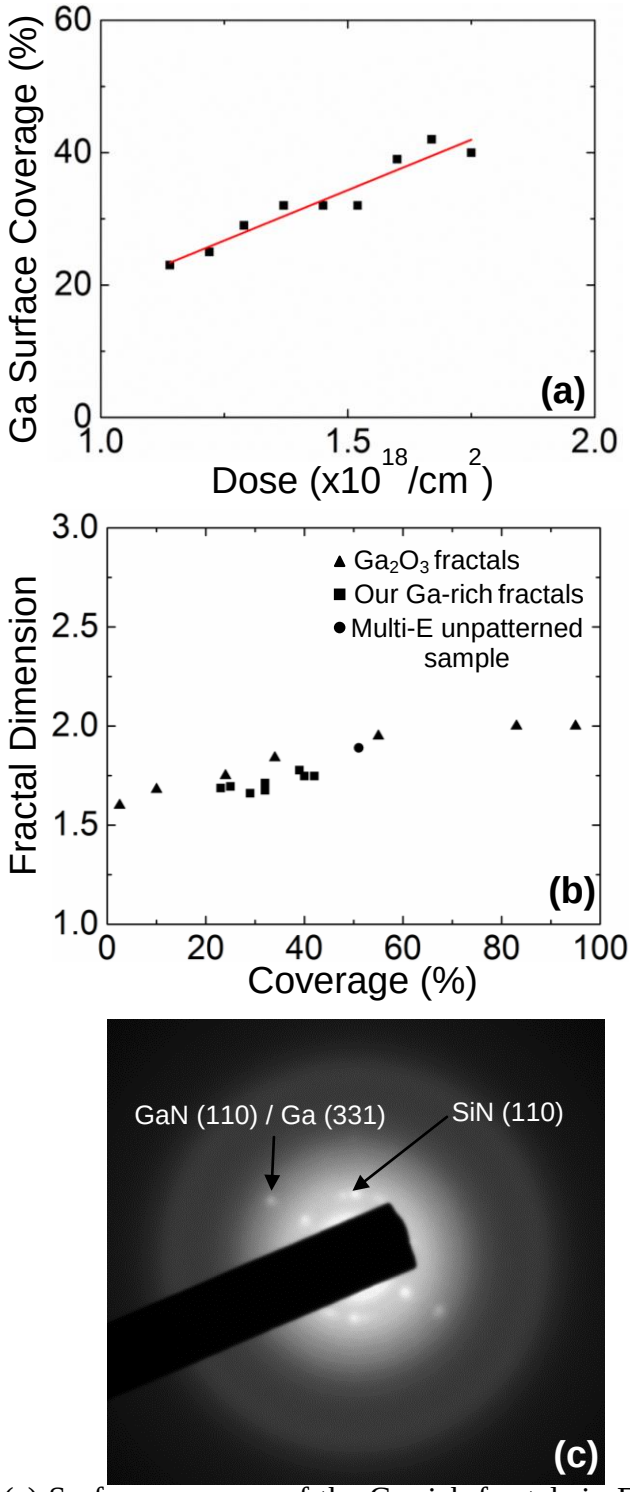

Fig. 3.7 (a) Surface coverage of the Ga-rich fractals in Fig. 3.5 as a function of dose. (b) Fractal dimension vs. coverage for our Ga-rich fractals (squares) and the Ga_2O_3 fractals (triangles).[35] The fractal dimension is also shown for the center area of the "multi-E unpatterned" sample (circle). (c) SAD pattern from our Ga-rich fractals.

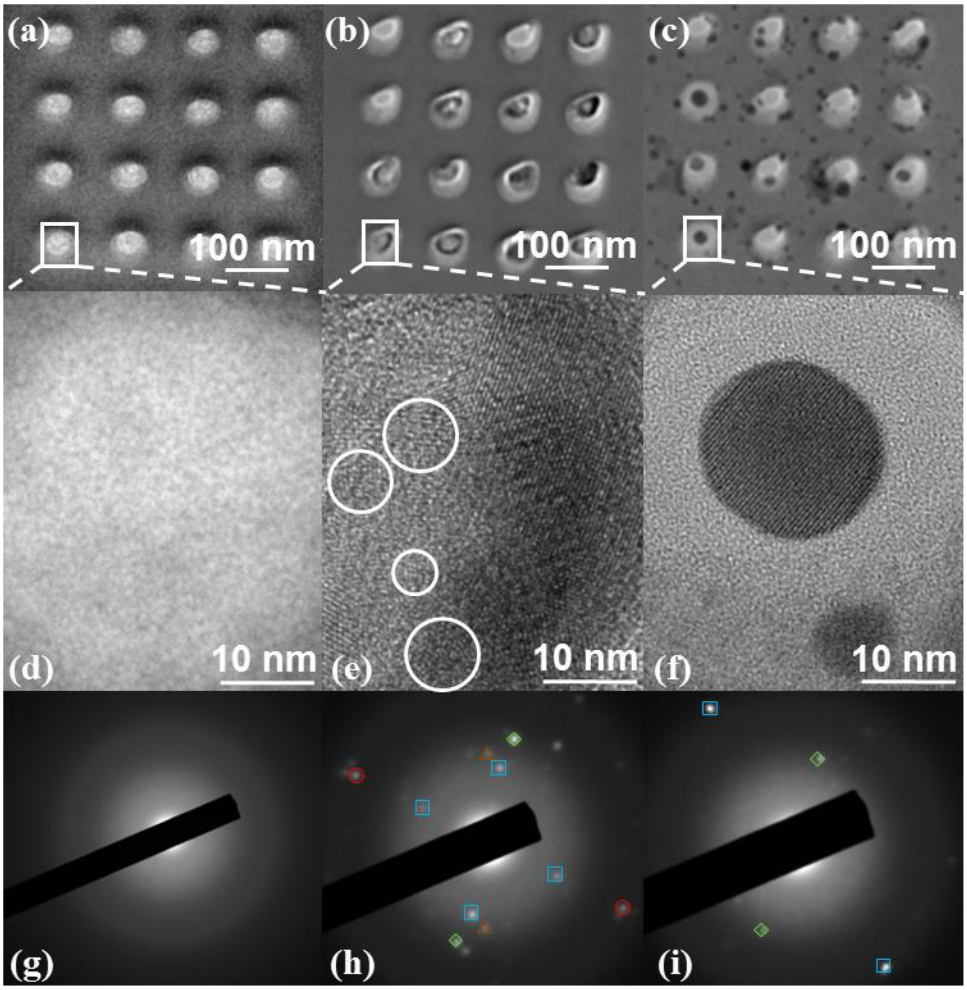

Fig. 3.8 (a) BF, (d) HRTEM, and (g) SAD from Si NCs nucleated in a "high-E patterned" sample. (b) ((c)) TEM BF image of a "multi-E patterned w/ mask" sample with (e) ((f)) corresponding high resolution TEM and (h) ((i)) typical SAD from an implanted spot after 8 (16) min of RTA at 900˚C. SAD spots in (h) are identified as Ga (330) (squares), Ga(331) (triangles), Ga (660) (circles), and Si (220) (diamonds). SAD spot in (i) are identified as Si (220) (diamonds) and Si (422) (squares).

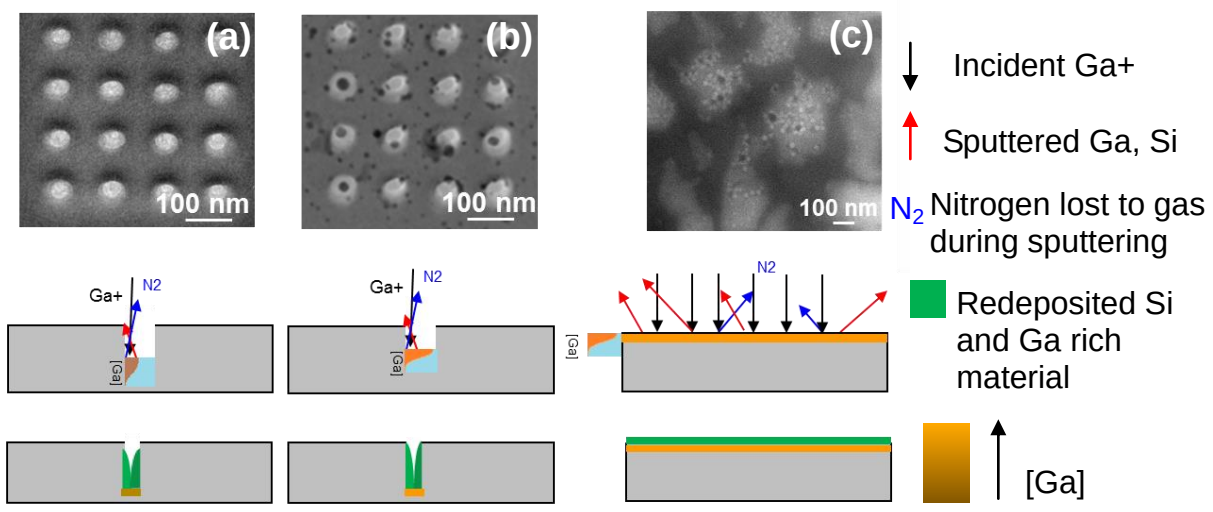

Fig. 3.9 Diagram showing enhanced redeposition for a surface with a (a) high aspect ratio, low [Ga], (b) high aspect ratio, high [Ga], and (c) low aspect ratio, high [Ga]. The orange areas depict areas implanted with Ga, while the green areas depict redeposited material that is Si- and Ga-rich.

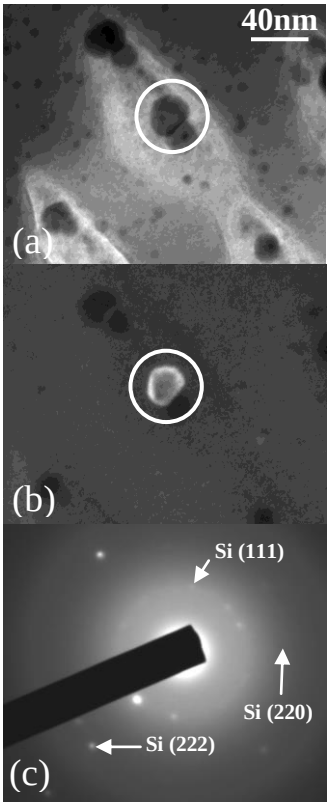

Fig. 3.10 (a) Bright-field, (b) corresponding dark-field, and (c) SAD from Si NCs nucleated in a "high E patterned" sample with a local Ga source.

3.8 References

[1] E. C. Cho, S. Park, X. Hao, D. Song, G. Conibeer, S. C. Park, and M. A. Green, Nanotechnology **19**, 245201 (2008).

[2] L. Pavesi, L. Dal Negro, C. Mazzoleni, G. Franzo, and F. Priolo, Nature **408**, 440 (2000).

[3] S. Tiwari, F. Rana, H. Hanafi, A. Hartstein, E. F. Crabbe, and K. Chan, Appl. Phys. Lett. **68** 1377 (1996).

[4] R. Lechner, A. R. Stegner, R. N. Pereira, R. Dietmueller, M. S. Brandt, A. Ebbers, M. Trocha, H. Wiggers, and M. Stutzmann, J. Appl. Phys. **104**, 053701 (2008).

[5] T. L. Chan, M. L. Tiago, E. Kaxiras, and J. R. Chelikowsky, Nano Lett. **8**, 596 (2008).

[6] Y. Yin, W. Xu, G. Ran, G. Qin, and B. Zhang, Funct. Mater. Lett. **4**, 255 (2011).

[7] Y.-H. So, S. Huang, G. Conibeer, and M. A. Green, Eur Phys. Lett. **96**, 17011 (2011).

[8] V. Svrcek and M. Kondo, IEEE Photovoltaics Specialists Conference, 837 (2009).

[9] Z. Zhou, M. L. Steigerwald, R. A. Friesner, and L. Brus, Phys. Rev. B **71**, 245308 (2005).

[10] M. K. Sunkara, S. Sharma, R. Miranda, G. Lian, and E.C. Dickey, Appl. Phys. Lett. **79**, 1546 (2001).

[11] M. Hetzel, A. Lugstein, C. Zeiner, T. Wójcik, P. Pongratz, and E. Bertagnolli, Nanotechnology **22**, 395601 (2011).

[12] M. Fujii, M. Yoshida, Y. Kanzawa, S. Hayashi, and K. Yamamoto, Appl. Phys. Lett. **71**, 1198 (1997).

[13] L. Dal Negro, R. Li, J. Warga, and S. N. Basu, Appl. Phys. Lett. 92, 181105 (2008).

[14] F. Priolo, G. Franzo, D. Pacifici, V. Vinciguerra, F. Iacona, and A. Irrera, J. Appl. Phys. **89**, 264 (2001).

[15] W. C. Ding, D. Hu, J. Zheng, P. Chen, B. W. Cheng, J. Z. Yu and Q. M. Wang, J. Phys. D: Appl. Phys. 41 (2008).

[16] P. G. Kik, M. L. Brongersma, and A. Polman, Appl. Phys. Lett. **76**, 2325 (2000).

[17] P. G. Kik and A. Polman, J. Appl. Phys. **88**, 1992 (2000).

[18] V. Ioannou-Sougleridis, P. Dimitrakis, V.E. Vamvakas, P. Normand, C. Bonafos, S. Schamm, A. Mouti, G.B. Assayag, and V. Paillard, Nanotechnology **18**, 215204 (2007).

[19] S. Choi, S. Baek, M. Jang, S. Jeon, J. Kim, C. Kim, and H. Hwang, J. Electrochem. Soc. **152**, G345 (2005).

[20] F.L. Bregolin, M. Behar, U.S. Sias, and E.C. Moreira, J. Lumin. **131**, 2377 (2011).

[21] U. S. Sias, M. Behar, H. Boudinov, and E. C. Moreira, J. Appl. Phys. 102, 043513 (2007).

[22] N. Nakamura, K. Noda, and Y. Yamauchi, Nucl. Instrum. Meth. B **227**, 299-305 (2005).

[23] S.A. Almeida, S.R.P. Silva, B.J. Sealy, and J.F. Watts, Phil. Mag. Lett. **78**, 319 (1998).

[24] S. Almeida, S. Silva, B. Sealy, and J. Watts, Thin Solid Films **343-344**, 632 (1999).

[25] S.R.P. Silva, S.A. Almeida, and B.J. Sealy, Nucl. Instrum. Meth. B **147**, 388 (1999).

[26] J. Yanagisawa, M. Toda, T. Kitamura, H. Matsumoto, and Y. Akasaka, J. Vac. Sci. Technol. B **23**, 3205 (2005).

[27] J. Yanagisawa, Nucl. Instrum. Meth. B **257**, 348 (2007).

[28] *Profile Code* (Implant Sciences Corp., Wakefield, MA, 1992).

[29] FEI Company, UHV Magnum Ion Column with BDS-200 User's Guide, (FEI Company, Hillsboro, OR, 2006), pp. 7-22–7-24.

[30] Annealing was performed in a Jet First-150 Rapid Thermal Processor with a 30˚C/sec ramp rate.

[31] International Centre for Diffraction Data: Newtown, PA, 2005; PDF#00-027-1402, PDF#01-073-7289, PDF#00-052-0591 (accessed Jan 4, 2010).

[32] B. Davidovitch, A. Levermann, and I. Procaccia, Phys. Rev. E **62**, R5919 (2000).

[33] Mandelbrot, Benoit, *Fractals and Chaos* (2004).

[34] D. Pile, Nat. Photonics **3**, 252 (2009).

[35] J. M. Chabala, Phys. Rev. B **47**, 11346 (1992).

[36] J. Hou and Z. Wu, Phys. Rev. B **40**, 1008 (1989).

[37] X. Zhang and C. Grigoropoulos, Rev. Sc. Instrum. **66**, 1115 (1994).

[38] S. Haridoss, F. Beniere, M. Gauneau, and A. Rupert, J. Appl. Phys. **51**, 5833 (1980).

[39] S.O. Kucheyev, J.S. Williams, and S. J. Pearton, Mater Sci Eng **33**, 51 (2001).

[40] Yamaguchi, H.,Shimase, A., Haraaichi, S. and Miyauchi, T, J Vac Sci Technol B **3**, 71 (1985).

[41] B. Boudart, J. C. Pesant, J. C. de Jaeger, and P.A. Dhamelincourt, J. Raman Spectrosc. **31**, 615 (2000).

[42] V. Baranwal, R. Krishna, F. Singh, A. Tripathi, A. C. Pandey, and D. Kanjilal, Appl. Surf. Sci. **253**, 5317 (2007).

[43] A. W. Wood, R. R. Collino, P. T. Wang, Y. Q. Wang, and R. S. Goldman, Appl. Phys. Lett. **100**, 203113 (2012).

[44] C. D. Thurmond and M. Kowalchik, Bell Syst. Tech. J. **39**, 169 (1960).

[45] S. Sharma and M. K. Sunkara, Nanotechnology, **15**, 130 (2004).

[46] I. Zardo, L. Yu, S. Conesa-Boj, S. Estrade, P. J. Alet, J. Roessler, M. Frimmer, P. Roca I Cararrocas, F. Peiro, J. Arbiol, J. R. Morante, and A. Fontcuberta I Morral, Nanotechnology, **20**, 155602 (2009).

[47] S. Guha and N. Bojarczuk, Appl. Phys. Lett. **72**, 415 (1998).

Chapter 4

Formation and Coarsening of Near-Surface Ga Nanoparticles on SiN_x

4.1 Overview

This chapter describes our investigations of the formation of coarsening of near-surface Ga nanoparticles (NPs) in SiN_x using low and medium dose Ga^+ focused-ion beam irradiation of SiN_x membranes, followed by rapid thermal annealing (RTA). This chapter opens with background information, including applications of Ga NPs. Then, we consider Profile Code simulations of Ga^+ implantation into SiN_x. Then, experimental details of our implantations of Ga^+ into SiN_x membranes are described. We then discuss the effects of surface curvature, annealing, and dose on the NP growth. For surfaces with minimal curvature, diffusive growth is apparent, leading to nearly close packed arrays with NP diameters as small as 3 nm and densities as high as ~$4x10^{12}$ cm^{-2}. The diffusive flux increases with annealing temperature, leading to NP coarsening by Ostwald ripening. For surfaces with increased curvature, the driving force for diffusion towards the valleys also increases, leading to Ga NP coalescence and a bi-modal distribution of NP sizes. The chapter concludes with a summary.

4.2 Background

Due to the size dependence of their band gap energy and light emission, silicon nanowires (NWs) are promising for solar cells[1] and light emitting devices.[2] Nanoparticles (NPs) of various metals have been used to catalyze the VLS growth of Si NWs,[3,4,5,6,7,8,9,10,11,12,13,14,15,16,17] with the NW diameter and growth direction typically dependent on the NP diameter.[17,18] Due to its ability to serve as both a dopant and low temperature catalyst, Ga has emerged as a promising candidate for seeding for Si NW growth.[19,20,21] Ga NPs have been formed by wide variety of methods including molecular beam epitaxy,[5,11,22,23,24] Ga atomic beam deposition,[25,26] chemical liquid deposition,[27] and evaporation[14,28] on several substrates including Si,[16] SiC,[5] GaAs,[11,22] Al_2O_3,[24] GaN,[23] SiO_2,[10,15,25] Si_3N_4,[15] and glass.[14] In most cases, the distribution of NP sizes and positions are not well controlled, and only the late stage growth mechanisms are understood. To achieve a site selective array of uniformly-sized, high density NPs, a detailed understanding of both the early and late stage growth mechanisms is needed. Recently, Ga^+ focused-ion-beam (FIB) irradiation, followed by annealing, has been proposed as a means to achieve small Ga NPs within selected areas; however, the observed distributions of NPs indicate that NP coalescence has already occurred.[19,29] In other work, Ga^+ implantation into N-rich ($x > 1.5$) α-SiN_x:H_y leads to preferential Ga displacement of Si, resulting in Ga-N, Ga-Ga, and Si-H bond formation.[30,31,32] Therefore, we examine the early stage growth mechanisms of Ga NPs using Ga^+ FIB irradiation of SiN_x, followed by rapid thermal annealing (RTA). To examine the influence of a Ga-

saturated surface layer (~10 nm deep) on Ga NP growth, we used a combination of low and high dose irradiation. When surface curvature is minimal, diffusive growth is enhanced by high dose irradiation and RTA. For surfaces with increased curvature, surface diffusion (due to the chemical potential gradient) is enhanced, leading to NP coalescence and a bimodal distribution. When the pitch is less than the lateral spread of the implanted ions, coalescence is limited, and nearly close-packed Ga NP arrays with diameters as small as 3 nm, and densities up to ~$4x10^{12}$ cm^{-2}, are observed.

4.3 Simulations

To examine the influence of a Ga-saturated surface layer on early stage NP growth, we considered Profile Code simulations of low ($8x10^{14}$ cm^{-2}) and high ($5x10^{17}$ cm^{-2}) dose irradiation. 5 keV high dose irradiation ($5x10^{17}$ cm^{-2}) allows us to saturate the top ~10 nm of the SiN_x surface with Ga, as shown by the Profile Code simulations in Fig. 4.1. The 30 keV low dose irradiation ($8x10^{14}$ cm^{-2}) allows us to have a minimal Ga concentration ~21 ± 7 nm below the surface, as shown by the Profile Code simulations in Fig. 4.1. Using 30 keV also allows us to maintain the spatial resolution of the FIB during patterning, since the expected FIB spot size is 25 nm (7 nm) at 5 keV (30 keV).[33]

4.4 Experimental Details

For these investigations, amorphous SiN_x membrane windows (Structure Probe, Inc) were irradiated with normal-incidence Ga^+ ions using an FEI Nova 200 Nanolab

dual-beam FIB system. 15 x 15 μm regions of SiN_x membranes were irradiated with low dose patterned irradiation with or without prior medium dose raster-scan irradiation. The medium-dose irradiation consisted of sequential $5x10^{17}cm^{-2}$ dose irradiations at 30 keV (dose rate: ~$9x10^{16}$ $cm^{-2}s^{-1}$), 20 keV (dose rate: ~$6x10^{16}$ $cm^{-2}s^{-1}$), 10 keV (dose rate: ~$3x10^{16}$ $cm^{-2}s^{-1}$), and 5 keV (dose rate: ~$2x10^{16}$ $cm^{-2}s^{-1}$), using a continuous raster scan mode, with p (pitch) = ½ d (spot size). The low-dose patterned irradiation consisted of arrays with p = 50, 60, 70, and 95 nm and d = 40 nm implanted at 30 keV with a dose rate of ~$3x10^{11}$ $cm^{-2}s^{-1}$ using a serpentine scan mode without beam blanking,[33] with a dose of $8x10^{14}$ cm^{-2} in each implanted spot.

Patterning was accomplished using various pitches including those less than, equal to, and greater than the lateral spread of the implanted ions (~56 nm for d = 40 nm).[34,35] For pitches less than or equal to the lateral spread of the implanted ions, the close proximity of the irradiated spots is expected to lead to minimal surface topography. On the other hand, for pitches greater than the lateral spread of the implanted ions, the valley depth is expected to be increased by localized sputtering, leading to gradients in the surface curvature. Following FIB irradiation, the samples were subjected to RTA in 1000 sccm N_2 environment for 16 minutes at 850 or 900˚C.[36] The samples are named "XYZ", where X is the pitch, Y is whether the sample had medium dose irradiation ("high") or just the low dose patterned irradiation ("low"), and Z is the annealing temp in ˚C, i.e. "50high850", "60high850", "70high850", "95high850", "50high900", "50low", "95low", and "50low900". Energy Dispersive X-Ray Spectroscopy (EDX), Bright-field (BF) and dark-field (DF) transmission electron microscopy (TEM) imaging, scanning TEM (STEM), and selected area diffraction (SAD) were carried out in a in a JEOL 2010F

operating at 200 keV. For SAD, apertures were used to select regions with ~0.1 μm diameter. To find the NP size distributions, SPIP was used, as described in appendix D.1. The standard error for these distributions was typically 1-2%, up to ~5%.

4.5 Formation of Ga Nanoparticles

Figures 4.2(a) and 4.2(b) present high-angle annular DF (HAADF) STEM images from 95low and 50low, with corresponding SAD patterns as insets. High-resolution views of the 50low are shown in Fig. 4.2(c), the HAADF STEM image of the region designated by a rectangle in Fig. 4.2(b), and in Fig. 4.2(d), a HRTEM cross-sectional image. For 95low, the HAADF image in Fig. 4.2(a) appears featureless, consistent with the diffuse ring observed in the corresponding SAD pattern. For 50low, Figs. 4.2(b) and 4.2(c) reveal a high density of ~3 nm diameter bright features. The corresponding SAD pattern in the inset of Fig. 4.2(c) contains a diffuse ring, suggesting that the bright features in Fig. 4.2(b) correspond to amorphous NPs. Furthermore, the presence of dark features on the left side of the HRTEM cross-sectional image in Fig. 4.2(d) suggests that the near-surface NPs are Ga-rich. This is confirmed by EDX data, shown in Fig. 4.2(e), where the spatial profiles of Si, N, and Ga concentration along the line in Fig. 4.2(c) reveal nearly constant values of [Si] and [N], with an increase in [Ga] in the vicinity of a NP. Thus, the NPs observed in Figs. 4.2(b), 4.2(c), and 4.2(d) are Ga-rich, similar to those observed on GaAs,[37] Si,[19] and C.[29]

To examine the mechanisms for Ga-rich NP precipitation, we compare the topographic profiles of the unannealed samples. Figures 4.2(f) and 4.2(g) present AFM

images from 95low and 50low, with corresponding average height profiles in Figs. 4.2(h) and 4.2(i), respectively. The second derivatives of the height profiles in Figs. 4.2(h) and 4.2(i) reveal hills and valleys, with the lowest curvature gradient for the p = 50 nm case. Since the surface with lower (higher) curvature gradient has a high (negligible) concentration of NPs, the driving force for NP formation is likely not surface diffusion. Instead, the overall higher Ga^+ irradiation dose likely leads to clustering of the implanted Ga atoms below the surface, similar to that predicted for Ge ions implanted into SiO_2.[38]

4.6 Ga Nanoparticle Coarsening Mechanisms

4.6.1 Influence of Dose and Annealing

To examine the effect of the vertical [Ga] gradient on annealing-induced NP growth, we separately vary the annealing temperature and the irradiation dose. First, we examine the influence of annealing at 900ºC, as captured in Figs. 4.3(a) and 4.3(b), which consist of HAADF STEM images of 50low and 50low900, respectively. These images show many bright Ga-rich NPs, whose size distributions and their Gaussian fits are shown in the plot of frequency vs. NP diameter in Fig. 4.3(c). Upon annealing, the average NP size increases from 3.0 ± 0.6 to 7.7 ± 2.2 nm, while the density decreases from ~4.0×10^{12} cm^{-2} to ~1.0×10^{12} cm^{-2}. Thus, the surface coverage increases from 28% to 46%. Since the surface coverage and NP size have both increased during RTA, it is hypothesized that a combination of Ga precipitation and coalescence has occurred, characteristic of early stage growth.[39]

The effect of high-dose irradiation prior to low dose patterning, is revealed by comparing the HAADF STEM images of 50low900 and 50high900, shown in Fig. 4.4(a) and 4.4(b), respectively, which show larger NPs for the sample prepared with raster scan irradiation. The Ga NP size distributions and their Gaussian fits are shown in the plot of frequency vs. NP diameter in Fig. 4.4(c). The saturation of the surface with Ga due to the pre-patterning raster-scan irradiation induced an increase of NP size from 7.7 ± 2.2 nm to 11.9 ± 2.7 nm, and a decrease in density from ~1.0x10^{12} cm^{-2} to ~5.5 x10^{11} cm^{-2}. This enhancement in vertical Ga diffusion is likely due to the larger vertical [Ga] gradient for the higher dose sample.

The influence of RTA temperature is captured in Figs. 4.5(a) and 4.5(b), which consist of HAADF STEM images of the 50high850 and 50high900 samples, prepared using high dose patterned irradiation (p = 50 nm), followed by RTA at 850˚C and 900˚C, respectively. These images show many bright Ga NPs, whose size distributions and their Gaussian fits are shown in the plot of frequency vs. NP diameter in Fig. 4.5(c). For RTA at 850˚C, a log-normal size distribution is observed, suggesting that NP growth is dominated by dynamic coalescence.[40] When the RTA temperature is increased from 850 to 900 ˚C, the NP size increases from 5.3 ± 1.6 to 11.9 ± 2.7 nm, while the density decreases from 2.7x10^{12} cm^{-2} to 5.5x10^{11} cm^{-2}, and the surface coverage remains constant at ~61%. This apparently mass-conservative NP coarsening with increasing RTA temperature suggests that the nucleation process is essentially complete, with additional NP growth due to Ostwald ripening. This RTA-temperature-dependent transition from dynamic coalescence to Ostwald ripening is further confirmed by the self-similarity of the normalized size distributions shown in the inset of Fig. 4.5(c), where the frequency, f,

is the number of NP within the specified range divided by the total number of NPs; d is the NP diameter; and d_m is the mean NP diameter. Similar coalescence was observed for post-deposition annealing of Ga on GaAs, where a uniform Ga cluster size distribution was attributed to Ostwald ripening.[39]

4.6.2 Influence of Surface Curvature

We now describe the effect of surface curvature gradients on annealing-induced Ga NP growth. Figures 4.7(a) and 4.7(b) present AFM images from the 50high850 and 95high850 samples patterned with p = 50 and 95 nm, respectively. Fig. 4.7(c) (Fig. 4.7(d)), the average cuts of tip height along the line in Fig. 4.7(a) (4.7(b)), reveals ~1nm (~3nm) valley depths with lower (higher) curvature for the 50high850 (95high850) sample. The influence of minimal surface curvature gradient on NP formation is captured in Figs. 4.8(a) and 4.8(c), which consist of HAADF STEM images of 50high850 and 60high850 with NP formation following 'high' dose patterned irradiation (p = 50 nm and p = 60 nm), respectively, followed by RTA @ 850˚C. Figure 4.8(a) shows many bright isotropically distributed Ga NPs, while Fig. 4.8(c) shows Ga NPs within the path scanned during patterning. The Ga NP size distributions and their Gaussian fits are shown in the plot of frequency vs. NP diameter in Fig. 4.8(e). For pitches less than or equal to the lateral spread (p = 50 and p = 60 nm), the NP size distribution is mono-modal, with average sizes of 5.3 ± 1.6 and 5.2 ± 2.2 nm, and densities of ~2.7 and ~1.6×10^{12} cm^{-2}, respectively. The influence of increased surface curvature gradient is captured in Fig. 4.8(b) (4.8 (d)), which consists of a HAADF STEM image of 70high850

(95high850) following 'high' dose patterned irradiation (p = 70 nm (p = 95 nm)), followed by RTA @ 850˚C. These images show larger NPs within the patterned spots, with smaller NPs surrounding the spots. The NP size distributions and their bi-modal Gaussian fits, are shown in the plot of frequency vs. of NP diameter in Fig. 4.8(e). The smaller NPs are 6.0 ± 1.8 (p = 70 nm) and 7.0 ± 1.5 (p = 95 nm), similar to the 50high850 and 60 high850 samples. The larger NP within the implanted spots are 12.6 ± 2.6 (p = 70 nm) and 12.9 ± 2.3 (p = 95 nm). It is interesting to note that larger NPs are observed in the areas with larger curvature within 95high850. Since 95high850 has a larger curvature gradient than 50high850, its chemical potential gradient and driving force for diffusion towards the valleys will be larger, leading to enhanced Ga NP growth and coalescence.

Fig. 4.9 presents low magnification STEM images of (a) 50low, (b) 50low900, (c) 50high900, (d) 50high850, (e) 60high850, (f) 70high850, and (g) 95high850. All of these images show that the NP arrays have long range order that is consistent across the sample.

4.7 Conclusions

In summary, we have investigated the formation of near-surface Ga NPs in SiN_x using low dose Ga^+ focused-ion beam irradiation of SiN_x membranes, followed by RTA. Dose-limited diffusive growth, with mono-modal size distributions, is observed for beam spot separations (pitch) less than the lateral spread of implanted ions. RTA at elevated temperature leads to NP coarsening by Ostwald ripening. High dose irradiation prior to patterning increases the vertical [Ga] gradient, leading to enhanced diffusion and NP

coarsening. When the pitch exceeds the lateral spread of implanted ions, the increased surface curvature gradient enhances diffusion, leading to enhanced Ga NP coalescence and a bi-modal distribution of NP sizes. We identify a regime of limited surface curvature, where limited coalescence lead to arrays with NP sizes as small as ~3 nm and densities as high as ~$4x10^{12}$ cm^{-2}.

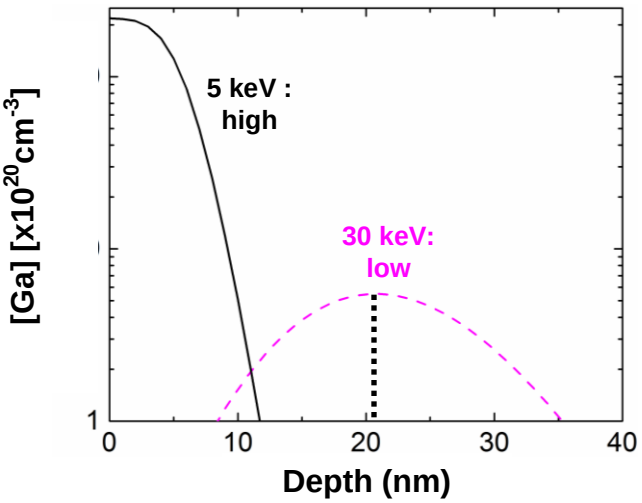

Fig. 4.1 Profile Code simulations of Ga^+ ion implantation into Si_3N_4 at 5 keV reveal that high dose ($5x10^{17}$ cm^{-2}) 5 keV irradiation is predicted to lead to a large near-surface [Ga]. Low dose ($8x10^{14}$ cm^{-2}) 30 keV irradiation is expected to have a range and straggle of ~21 and ~7 nm, respectively, with minimal Ga accumulation at the surface due to sputtering

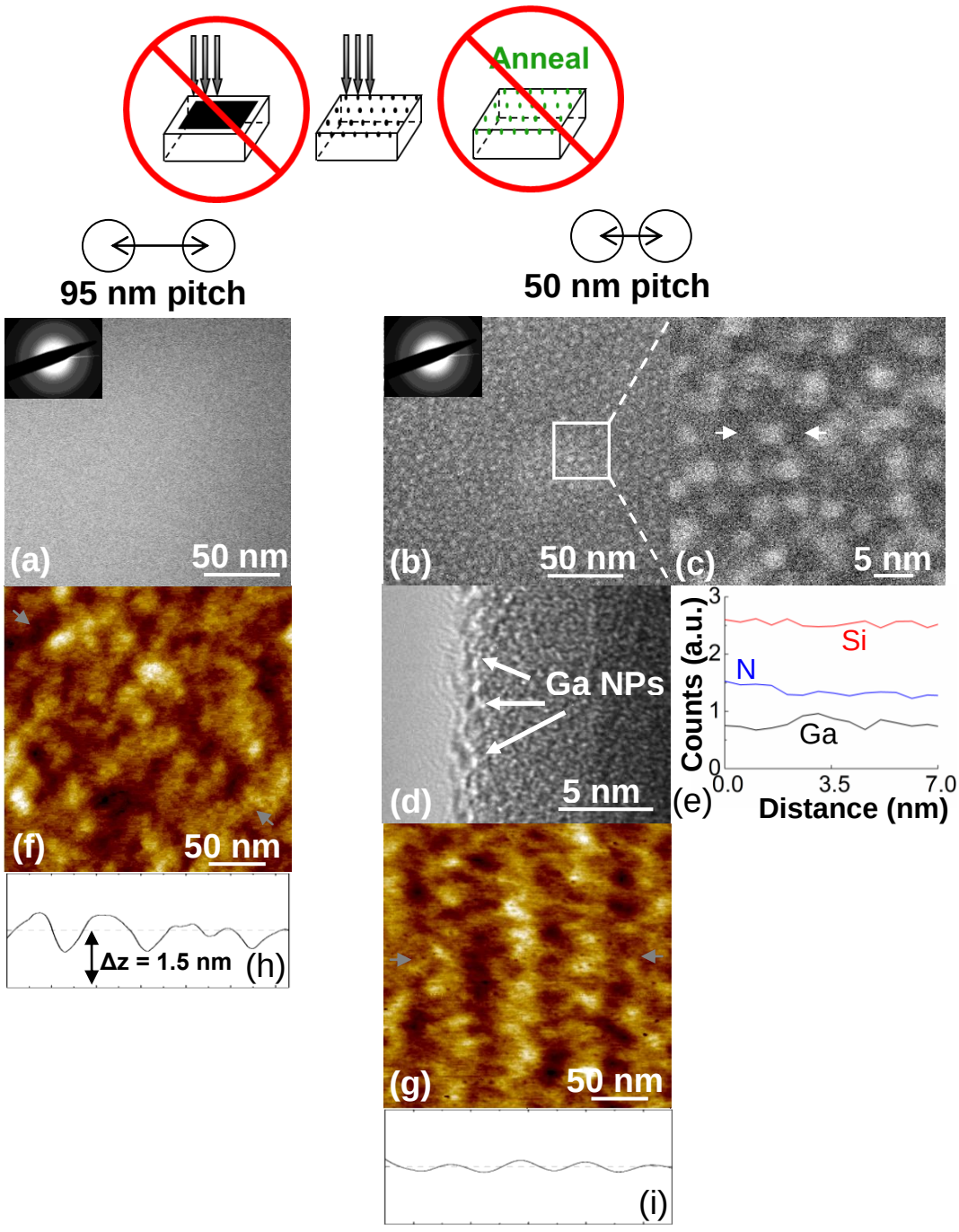

Fig. 4.2 (a) HAADF STEM image of 95low. (b) HAADF STEM image with inset SAD pattern and (c) corresponding HR HAADF STEM image along with a (d) HR TEM cross-sectional image from 50low showing many bright Ga NPs. Using the line-cut indicated in (c), the spatial profiles of Si, N, and Ga concentration are shown in (e). These spatial profiles were captured with a beam with a spot size of 1 nm. AFM images corresponding to 95low and 50low are shown in (f) and (g), with average height profiles in (h) and (i).

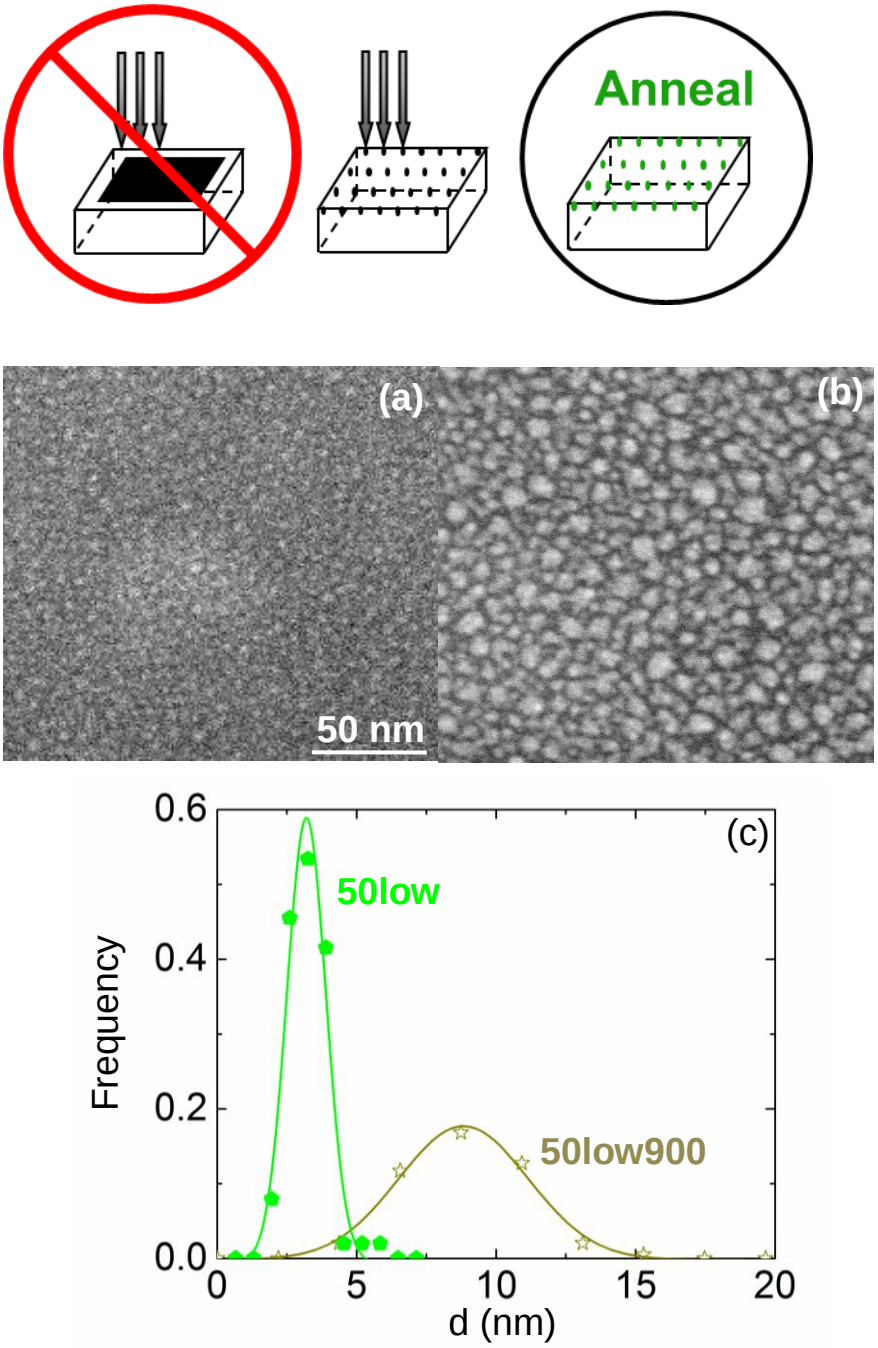

Fig. 4.3 HAADF STEM images from the (a) 50low and (b) 50low900 samples reveal that Ga-rich NP size increases with annealing. (c) The NP size distribution for 50low (filled pentagons) and 50low900 (empty stars) samples and their fits to a Gaussian and log-normal distribution are shown as lines with R^2 values of 0.990 and 0.951, respectively.

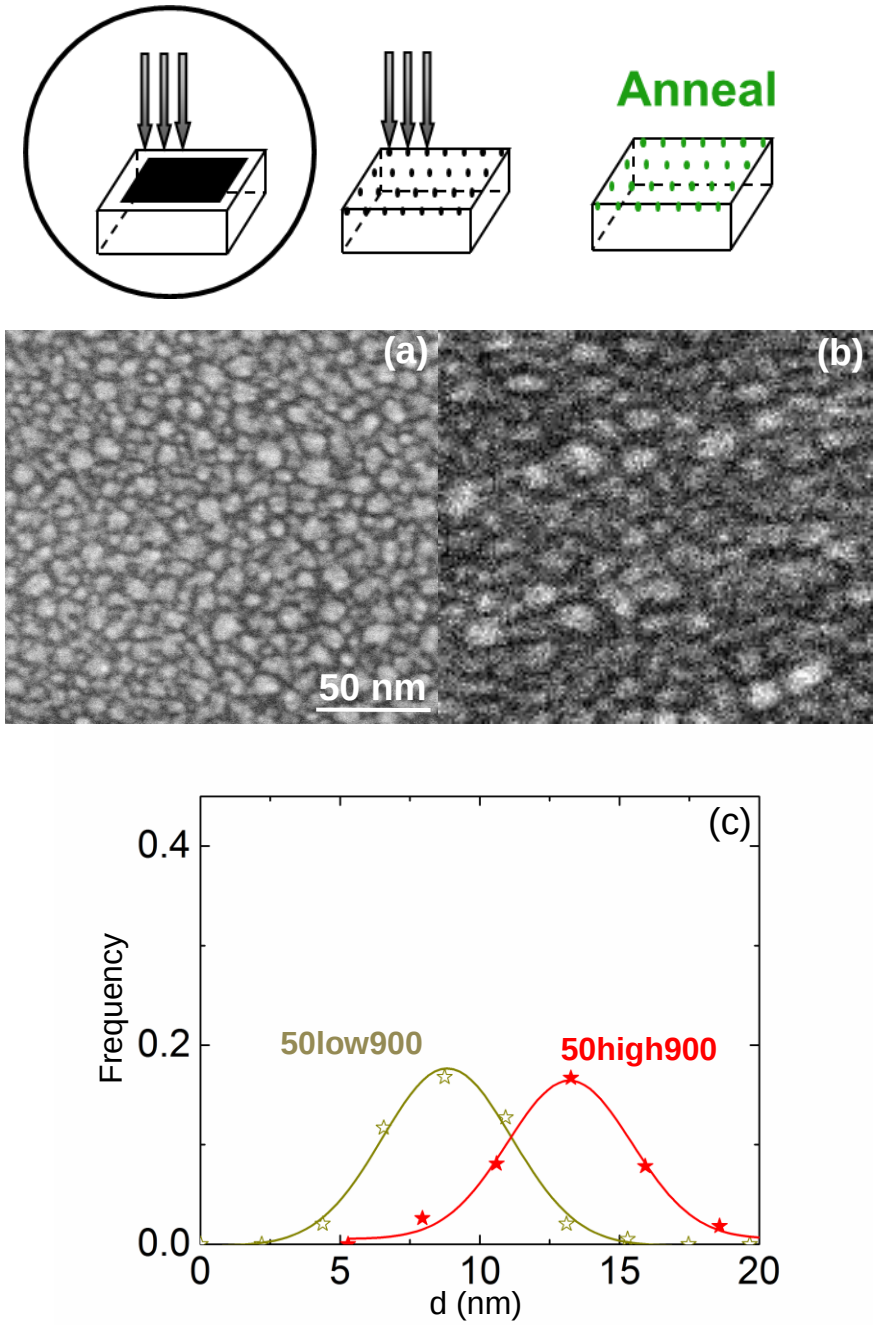

Fig. 4.4 HAADF STEM images of (a) 50low900, (b) 50high900, (c) NP size distributions from 50low900 and 50high900 samples reveal that Ga-rich NP size increases with the addition of raster-scan irradiation as shown by the data points marked with empty and filled stars, respectively, and their fits to a Gaussian distribution are shown as lines with R^2 values of 0.985 and 0.984, respectively.

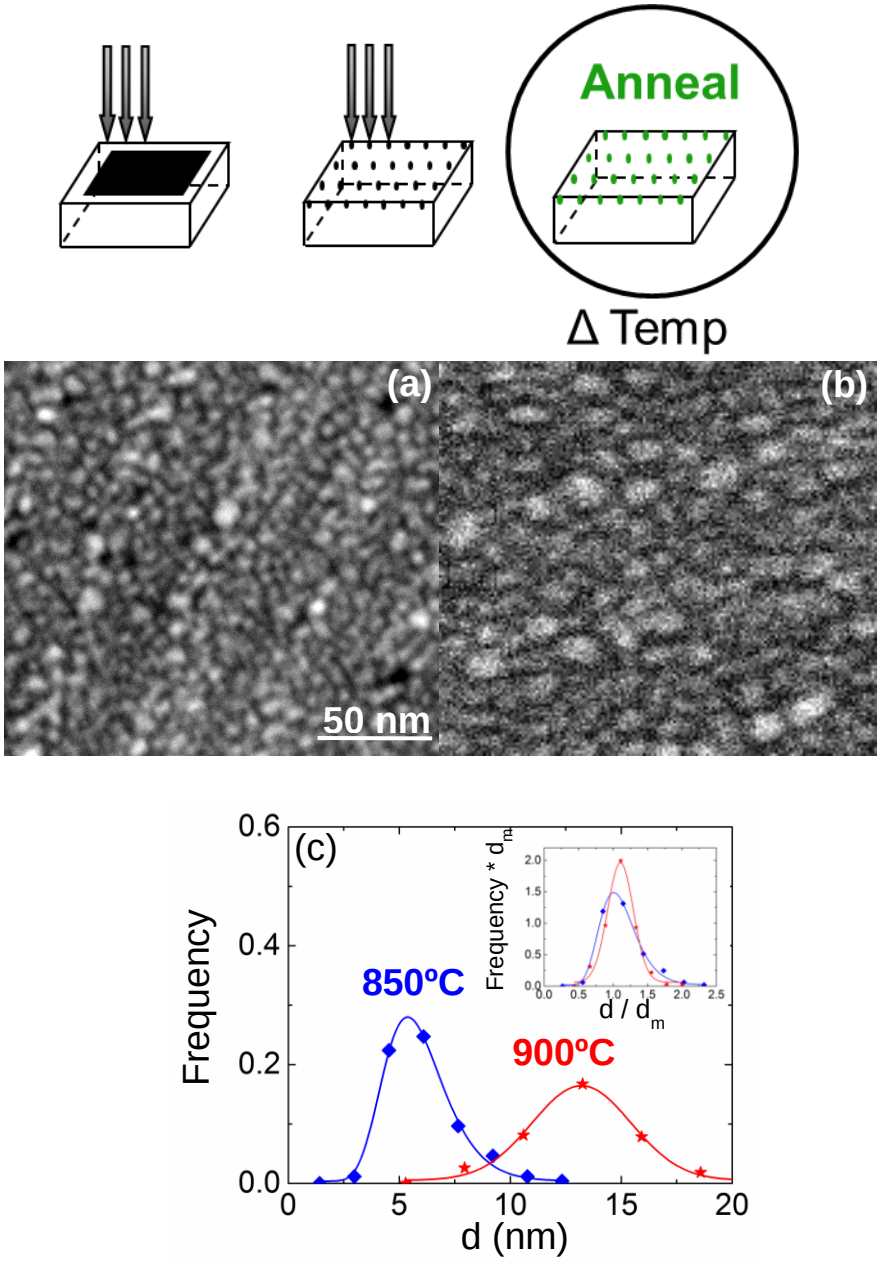

Fig. 4.5 HAADF STEM images from the (a) 50high850 and (b) 50high900 samples reveal that Ga-rich NP size increases with annealing. The NP size distribution for 50high850 (filled diamonds) and 50high900 (filled stars) and their fits to a Gaussian distribution are shown as lines with R^2 values of 0.984 and 0.985, respectively, are shown in (c). The normalized NP distribution for 50high850 (filled diamonds) and 50high900 (filled stars) are shown as in inset in (c).

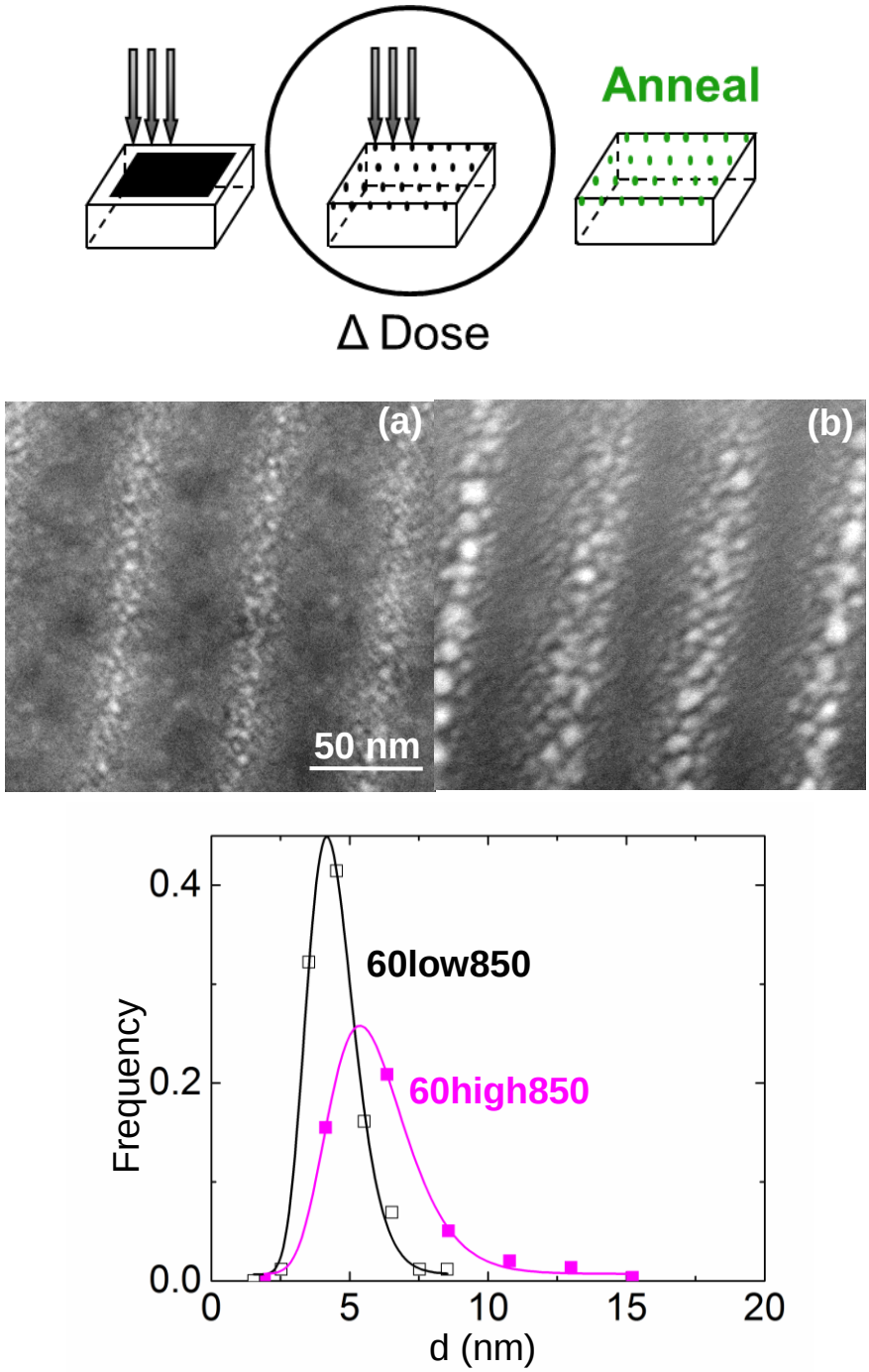

Fig. 4.6 HAADF STEM images from the (a) 60low850 and (b) 60high850 samples reveal that Ga-rich NP size increases with patterned irradiation dose. (c) Corresponding NP size distributions with data points marked with empty and filled squares, respectively, and their fits to a log-normal distribution are shown as lines with R^2 values of 0.990 and 0.992, respectively.

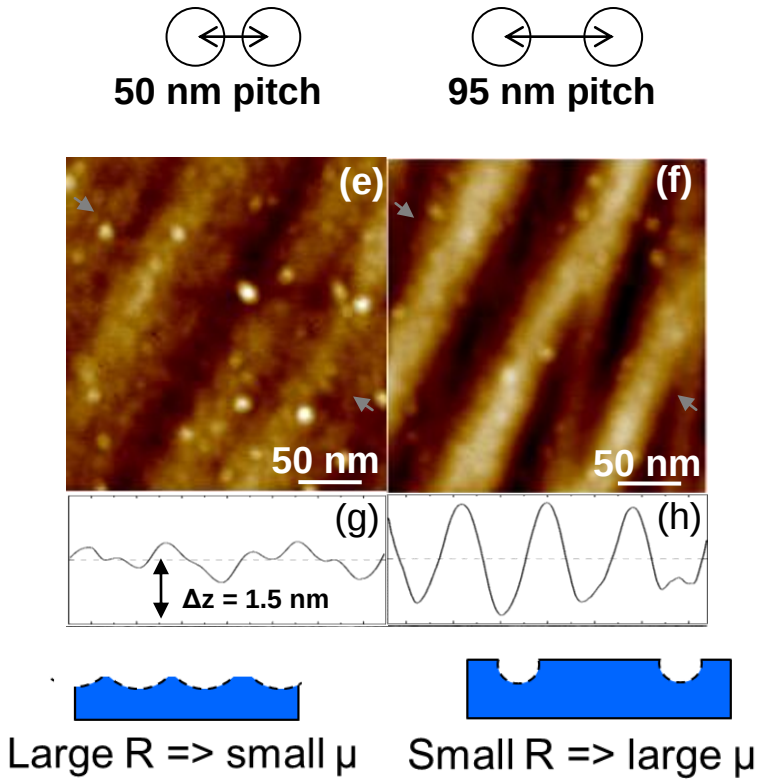

Fig. 4.7 AFM images from (a) 50high850 and (b) 95high850 with average height profiles below in (c) and (d), respectively.

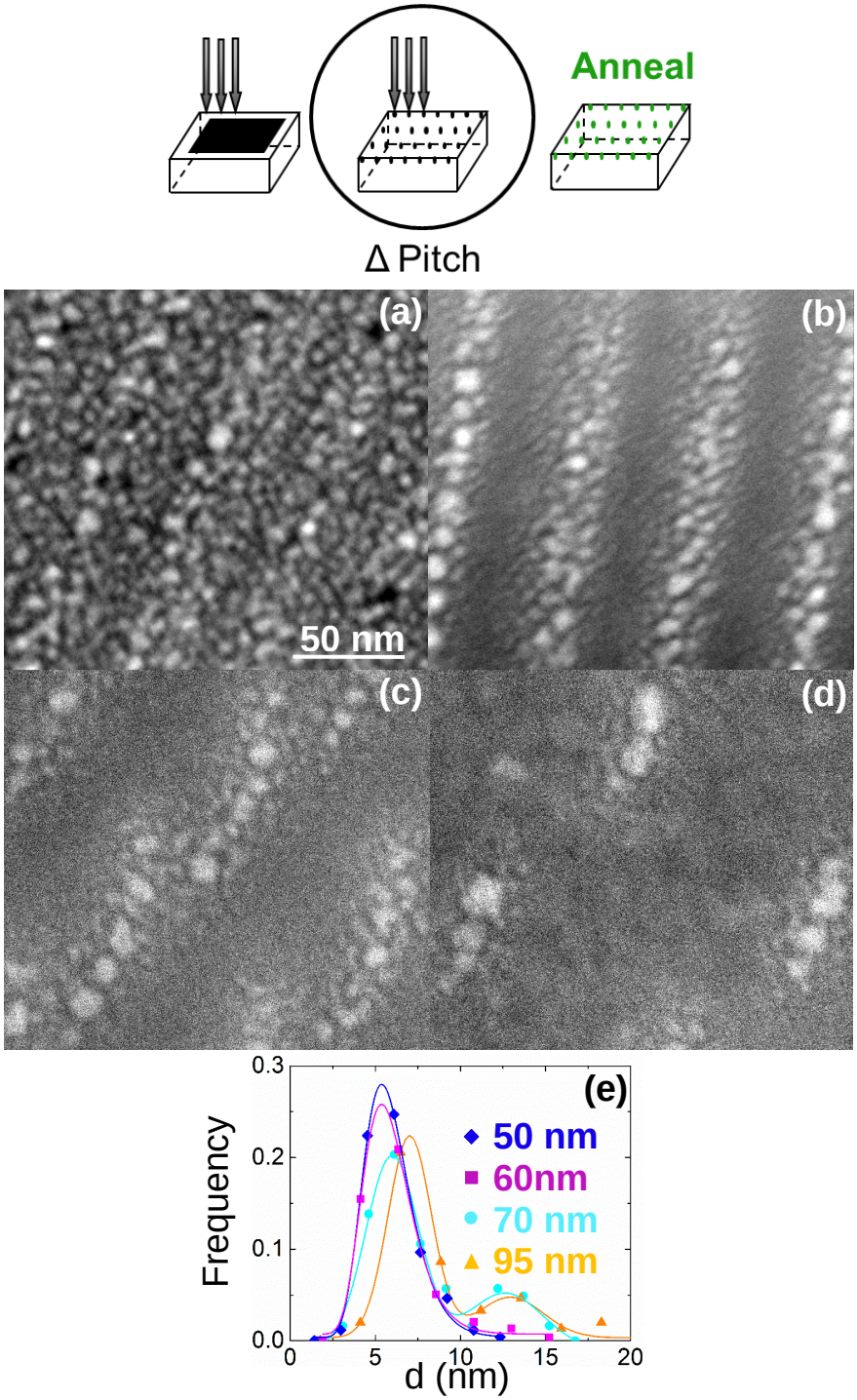

Fig. 4.8 HAADF STEM images of (a) 50high850, (c) 60high850, (b) 70high850, and (d) 95high850. (e) The NP size distribution for 50high850 and 60high850 and their fits to a log-normal distribution are shown as lines with R^2 values of 0.990, 0.992. (e) The NP size distribution for 70high850 and 95high850 and their fits to a bi-modal Gaussian distribution are shown as lines with R^2 values of 0.930 and 0.980, respectively.

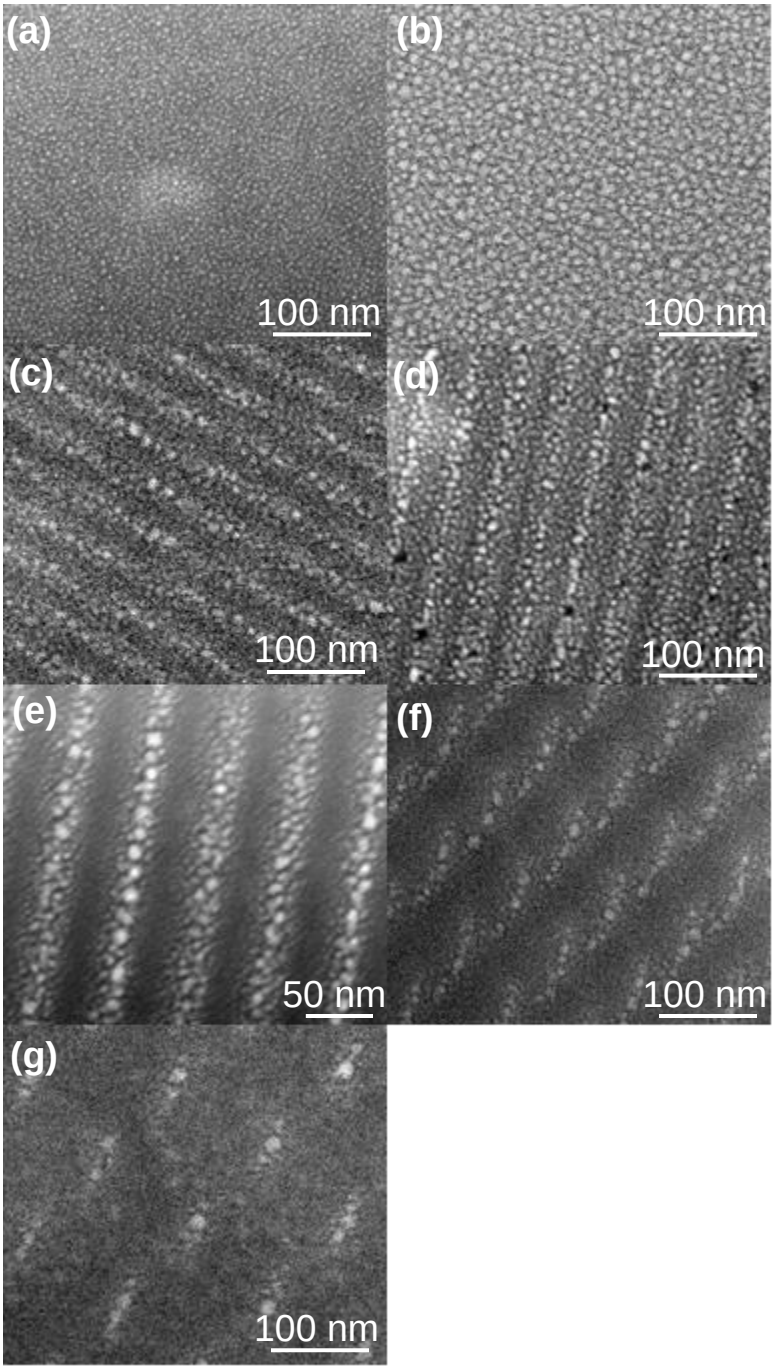

Fig. 4.9 Low magnification STEM images of (a) unannealed ref., (b) annealed ref., (c) 50high900, (d) 50high850, (e) 60high850, (f) 70high850, and (g) 95high850.

4.8 References

[1] J. B. Baxter and E. S. Aydil, Appl. Phys. Lett. **86**, 053114 (2005).

[2] X. F. Duan, Y. Huang, Y. Cui, J. F. Wang, and C. M. Lieber, Nature **409**, 66 (2001).

[3] N. Fukata, T. Oshima, T. Tsurui, S. Ito, K. Murakami, Sci. Technol. Adv. Mater. **6,** 628 (2005).

[4] X. Zhao, C. M. Wei, L. Yang, and M. Y. Chou, Phys. Rev. Lett. **92**, 236805 (2004).

[5] G. V. Bianco, M. M. Giangregorio, P. Capezzuto, M. Losurdo, T. H. Kim, A. S. Brown, G. Bruno, Mater Sci Eng **177**, 700 (2012).

[6] J. Westwater, D. P. Gosain, S. Tomiya, S. Usui, and H. Ruda, J. Vac. Sci. Technol. B **15**, 554 (1997).

[7] J. D. Holmes, K. P. Johnston, R. C Doty, and B. A. Korgel, Science **287**, 1471 (2000).

[8] Y. Wu, Y. Cui, L. Huynh, C. Barrelet, D. Bell, and C. Lieber, Nano Lett. **4**, 433 (2004).

[9] A. Lugstein, M. Steinmair, Y. J. Hyun, G. Hauer, P. Pongratz, and E. Bertagnolli, Nano Lett. **8**, 2310 (2008).

[10] Z. Pan, S. Dai, D. B. Beach, and D. H. Lowndes, Nano Lett. **3**, 1279 (2003).

[11] S. Conesa-Boj, I. Zardo, S. Estrade, Li Wei, Pierre Jean Alet, P. Roca i Cabarrocas, J. R. Morante, F. Peir, A. Fontcuberta i Morral, and J. Arbiol, J. Cryst. Growth **10**, 1534 (2010).

[12] O. Moutanabbir, S. Senz, R. Scholz, M. Alexe, Y. Kim, E. Pippel, Y. Wang, C. Wiethoff, T. Nabbefeld, F. Meyer zu Heringdorf, and M. Horn-von Hoegen, ACS Nano **5**, 1313 (2011).

[13] L. Yu, B. O'Donnell1, P. Alet, S. Conesa-Boj, F. Peir´o, J. Arbiol, and P. Roca i Cabarrocas, Nanotechnology **20**, 225604 (2009).

[14] M. Jeon, Y. Tomitsuka, and K. Kamisako, J. Ind. Eng. Chem. **14**, 836 (2008).

[15] A. Reguer and H. Dallaporta, Mat. Sci. Semicon. Proc. **12**, 44 (2009).

[16] J. Bae, N. N. Kulkarni, J. P. Zhou, J. G. Ekerdt, and C. Shih, J. Cryst. Growth **310**, 4407 (2008).

[17] Y. Cui, L. J. Lauhon, M. S. Gudiksen, J. Wang, and C. M. Lieber, Appl. Phys. Lett. **78**, 2214 (2001).

[18] A. Lugstein, M. Steinmair, Y. J. Hyun, G. Hauer, P. Pongratz, and E. Bertagnolli, Nano Lett. **8**, 2310 (2008).

[19] M. Hetzel, A. Lugstein, C. Zeiner, T. Wójcik, P. Pongratz, and E. Bertagnolli, Nanotechnology **22**, 395601 (2011).

[20] V. Svrcek and M. Kondo, IEEE Photovoltaics Specialists Conference, 837 (2009).

[21] Z. Zhou, M. L. Steigerwald, R. A. Friesner, and L. Brus, Phys. Rev. B **71**, 245308 (2005).

[22] I. Zardo, L. Yu, S. Conesa-Boj, S. Estrade, P. J. Alet, J. Roessler, M. Frimmer, P. Roca i Cararrocas, F. Peiro, J. Arbiol, J. R. Morante, and A. Fontcuberta i Morral, Nanotechnology **20**, 155602 (2009).

[23] P. C. Wu, M. Losurdo, T. Kim, M. Giangregorio, G. Bruno, H. O. Everitt, and A. S. Brown, Langmuir **25**, 924 (2009).

[24] P. C. Wu, T. Kim, A. S. Brown, M. Losurdo, G. Bruno and H. O. Everitt, Appl. Phys. Lett. **90**, 103119 (2007).

[25] K. F. MacDonald, V. A. Fedotov, S. Pochon, K. J. Ross, G. C. Stevens, N. I. Zheludev, W. S. Brocklesby, and V. I Emel'yanov, Appl. Phys. Lett. 80, 1643 (2002).

[26] M. Kolibal, T. Cechal, E. Brandejsova, J. Cechal and T. Sikola, Nanotechnology **19**, 475606 (2008).

[27] M.F. Meléndrez, G. Cárdenas, and J. Arbiol, J. Colloid Interf. Sci. **346**, 279 (2010).

[28] M. Hernandez, M. Cervera, E. Ruiz, J. L. Pau1, J. Piqueras, M. Avella, and J. Jimenez, Nanotechnology **21**, 455602 (2010).

[29] P. Philipp, L. Bischoff, and B. Schmidt, Nanotechnology **23**, 475304 (2012).

[30] S.A. Almeida, S.R.P. Silva, B.J. Sealy, and J.F. Watts, Phil. Mag. Lett. **78**, 319 (1998).

[31] S. Almeida, S. Silva, B. Sealy, and J. Watts, Thin Solid Films **343-344**, 632 (1999).

[32] S.R.P. Silva, S.A. Almeida, and B.J. Sealy, Nucl. Instrum. Meth. B **147**, 388 (1999).

[33] FEI Company, UHV Magnum Ion Column with BDS-200 User's Guide, (FEI Company, Hillsboro, OR, 2006), pp. 7-22–7-24.

[34] J. F. Ziegler, J. P. Biersack, and U. Littmark, *The Stopping Range of Ions in Matter* (Pergamon, New York, 1985).

[35] Since the implanted spot size is ~40 nm, and the SRIM simulated lateral spread of the implanted ions is ~8 nm, the effective beam footprint is ~56 nm.

[36] Annealed in a Jet First-150 Rapid Thermal Processor with a 30˚C/sec ramp rate.

[37] K. A. Grossklaus and J. M. Millunchick, J. Appl. Phys. **109**, 014319 (2011)

[38] C.W. Yuan, D. O. Yi, I. D. Sharp, S. J. Shin, C.Y. Liao, J. Guzman, J.W. Ager III, E. E. Haller, and D. C. Chrzan, Phys. Rev. Lett **102**, 146101 (2009).

[39] M. Zinke-Allmang, L. C. Feldman, and M. H. Grabow, Surf. Sci. Rep. **16**, 377 (1992).

[40] C. G. Granqvist and R. A. Buhrman, J. Appl. Phys. **47**, 2200 (1976).

Chapter 5

Pump-Probe Measurements of Acoustic Phonon Propagation

5.1 Overview

We have investigated the influence of nanostructure within a SiN_x membrane on the damping of coherent acoustic resonances induced by pump laser excitation. This chapter opens with background information on acoustic phonon scattering experiments in reflection geometry. We then describe our pump-probe transmission experiments of SiN_x membranes. We then discuss the acoustic phonon resonances within the 10-100 GHz range exhibited by SiN_x membranes that are implanted and/or annealed. In this frequency range, the acoustic damping increases linearly with phonon frequency. Similar acoustic phonon damping was observed for the as-received, annealed, and as-implanted SiNx membranes whose thickness exceeds 200nm. For the thinner SiNx membranes, an increase in acoustic phonon damping is observed for both as-received membranes and those which were implanted and annealed to form nano crystallites. The chapter concludes with a summary.

5.2 Background

Nanophononic and nanomechanical systems are of interest for studying heat transfer at the nanoscale. In these small scale systems, the mean free path of the elastic phonons is similar to the size of the nanocrystals, resulting in enhanced scattering of the waves by the grain boundaries.[1] Some of the most responsive electromechanical sensors are based on acoustic vibrations within nanocrystals.[2,3] Previous work has examined GHz range resonance of Au nanoparticles on SiO_2, where the oscillation frequency was shown to vary linearly with the size of the nanoparticles.[4] The thermal conductivity of various nanostructures including nanowires and nanocomposites is reduced due to phonon scattering at boundaries. Thus, a multilayer structure of Ge nanoparticles on Si layers led to decreased thermal conductivity below the amorphous limit.[5] In another study, resonant acoustic waves in Si membranes were examined, but only the fundamental mode is observed.[6] In other work, resonant acoustic modes in a semiconductor membrane were observed to be dependent on the repetition-rate frequency offset in an ASOPS configuration (see section 2.9).[7] The damping of the acoustic waves is indirectly observed to be smaller in this case, but the measurement technique only allowed a temporal resolution of 1 ns. In order to better understand the resonant acoustic waves, a larger time window between pump pulses needs to be examined. In our experiment, we examine the acoustic resonance damping of phonons in SiN_x membranes due to pump excitation in an extended time interval of 10 ns. We discuss the effect of

membrane thickness, membrane-transducer interface, and membrane nanostructure on the coherent acoustic phonon damping.

5.3 Experimental Details

For these investigations, amorphous 500 nm thick SiN_x membranes (Structure Probe, Inc) were irradiated with normal-incidence Ga^+ ions using an FEI Nova 200 Nanolab dual-beam FIB system. The SiN_x membranes were saturated with Ga^+ ions through sequential $5x10^{17}$ cm^{-2} dose irradiations at 30 keV (dose rate: ~$9x10^{16}$ $cm^{-2}s^{-1}$), 20 keV (dose rate: ~$6x10^{16}$ $cm^{-2}s^{-1}$), 10 keV (dose rate: ~$3x10^{16}$ $cm^{-2}s^{-1}$), and 5 keV (dose rate: ~$2x10^{16}$ $cm^{-2}s^{-1}$), using a continuous raster scan mode, with p (pitch) = ½ d (spot size). After irradiation, this "as-implanted" sample had a thickness of ~200 nm. The "implanted-annealed" sample was subsequently annealed at 900ºC for 16 minutes. For comparison, we also examined 100 and 200 nm thick membranes samples that were unirradiated, which we will refer to as the "100 nm" and "200 nm" reference, respectively.

Following implantation and annealing, 120 nm of Ni was sputtered, as described in section 2.8, on the top side of the membranes, while 3/70 nm of Ni/Al was deposited on the bottom side. After metal deposition the samples were mounted in the sample holder in a vertical position in the Y-Z plane, where the pump laser beam is incident on the x-axis. We examined the time-domain thermoreflectance of the annealed 200nm reference, "as-implanted", and "implanted-annealed" samples using the setup described

in section 2.9. We also examined the transverse and longitudinal acoustic resonances exhibited in all of the samples using the pump-probe setup described in section 2.10.

5.4 Time-Domain Thermoreflectance Data

The goal was to study the effect of ion implantation and annealing formation of nanoparticles on the thermal conductivity of SiN_x membranes. Figure 5.1 presents plots of the time-domain thermoreflectance of the 200nm reference, "as-implanted", and "implanted-annealed" samples. In this type of the measurement the sample reflectivity is related to the refractive index, which is dependent on the temperature, as well as the strain and carrier concentration. Thus measurements of time-resolved reflectivity can be used to evaluate the sample temperature time-dependence, which is illustrated in Fig. 5.1 where the thermal decay following excitation by the pump laser is monitored as a function of time. The large temperature increase in the first nanosecond is due to the thermal excitation from the pump laser. This is followed by a relaxation due to heat dissipation inside the membrane. In the first few nanoseconds following excitation, longitudinal acoustic waves are observed. The measured decay of the reflectivity curve is a result of thermal diffusion, and can be related to the thermal conductivity. A smaller slope indicates a slower decay, and thus a lower thermal conductivity. The curves in the plot are nearly parallel, revealing that the slopes are similar and suggesting that the phonon scattering and thermal conductivity are similar, which indicates that the desired sensitivity for the implantation modification of thermal conductivity is not obtained. Nevertheless, it is important to consider several heat transfer competing effects that can

influence the observed result. The phonon scattering may be due to multiple factors including scattering at the interface between the metal and the SiN_x layer, within the SiN_x layer, or both. Also, because the implanted layer is only ~10 nm thick, the contribution to scattering of this small fraction of the total sample, may be insignificant. Therefore in order to better understand the mechanisms for the phonon scattering within these samples, we examined the samples in a pump-probe configuration that monitors the acoustic phonon transmission through the membrane.

5.5 Pump Probe Transmission Data

For the pump-probe measurements of acoustic propagation, the experimental setup is described in section 2.10. The unimplanted 100nm reference and 200 nm reference, as well as the 200 nm annealed, implanted-unannealed, and the implanted annealed samples were examined with this setup. For each of these samples signal was collected in ~10 different spots across the 100 x 100 μm surface. As an example, the waveforms collected from the implanted-annealed sample are presented in Fig. 5.2. These waveforms are nearly sinusoidal with varying phase and amplitude. These larger amplitude and small frequency waves are attributed to transverse waves formed by the coherent acoustic phonons reflecting off the lateral boundaries of the 100 x 100 μm membrane. Since the phase and amplitude of the transverse waves varies so much across a single sample, it is not simple to compare transverse waves from different samples. The focus of the present work is to clarify the behavior of the longitudinal waves that propagate across the sample, which benefits from the simpler boundary conditions (planar surfaces and interfaces between the metal layers and SiNx layer) and are expected to be much more uniform. The longitudinal waves from the implanted-annealed sample are shown in Fig. 5.3 (a) along with an FFT of the longitudinal waves in Fig. 5.3 (b). To take the FFT of the longitudinal waves, the transverse waves were first subtracted using a smoothening to obtain the background function and then subtracting it from the experimental data before performing FFT analysis. The peak frequencies and full-width-at-half-max were measured for each measured waveform, and then averaged for each

sample at each frequency. In Fig. 5.4 the FWHM as a function of frequency is plotted for the 100 nm reference (a), 200 nm reference (b), 200 nm annealed, (c), the 200 nm as-implanted (d), and the 100 nm implanted-annealed (e). The FWHM is used to compare the damping of these samples, as it is proportional to the damping of the phonons at the probed frequencies.

5.5.1 Membrane Thickness Dependence of Coherent Acoustic Phonon Damping

We now examine the effect of membrane thickness on phonon damping. We compare the 100 nm reference (Fig. 5.4 (a)) and the 200 nm reference (Fig. 5.4 (b)). The plots of FWHM as a function of frequency are fit with a linear fit that has a slope of 0.041 ± 0.007 and 0.032 ± 0.003 for the 100 nm and 200 nm reference samples, respectively. It is apparent that the damping increases with frequency for both thicknesses, but at a significantly faster rate for the 100 nm sample. The fundamental mode frequency is larger for the thinner 100 nm reference sample (~13.5 GHz) compared to the fundamental mode of the 200 nm reference (~10 GHz). The ratio of these fundamental mode frequencies is the inverse of the ratio of the thicknesses of the 100 nm and 200 nm reference, which are ~293 nm and ~393 nm thick, respectively. Comparing the FWHM at higher frequencies, it is apparent that the FWHM at ~60 GHz is ~ 2.3 GHz for the 100nm sample, while only ~1.6 GHz for the 200 nm sample. From these comparisons, it is apparent that the damping at higher frequencies is dependent on the thickness of the membrane. This may be due to the increased number of transducer-

membrane interfaces per unit time that the phonons must cross in the thinner sample, or it may be due to increased damping within the transducer layers.

5.5.2 Effect of Annealing on Coherent Acoustic Phonon Damping

To examine the effect of annealing prior to implantation on phonon damping, we compare the 200 nm reference with the 200 nm unimplanted-annealed sample. Both samples also have a similar total thickness of ~393 nm (including transducers), which is confirmed by the similarity of the fundamental frequency modes, which are both ~ 10 GHz. The plots of FWHM as a function of frequency are shown with a linear fits that have slopes of 0.029 ± 0.003 and 0.032 ± 0.004 for the 200 nm reference (Fig. 5.4 (b)) and the 200 nm unimplanted-annealed (Fig. 5.4 (c)) samples, respectively. The similar slopes indicate that the increase in damping with frequency is similar after annealing. Before and after annealing the FWHM at ~60 GHz is still ~1.6 GHz, suggesting that the annealing didn't have a significant effect on the damping. These results also suggest that annealing did not significantly change the transducer-membrane interface, since no increase in damping, and therefore no increase in phonon scattering at the interface was detected.

5.5.3 Effect of Ga+ Ion Irradiation on Coherent Acoustic Phonon Damping

To examine the effect of Ga^+ irradiation on phonon damping, we compare the 200 nm reference and the 200 nm as-implanted samples. The plots of FWHM as a function of

frequency are fit with a linear fit that has a slope of 0.029 ± 0.003 and 0.032 ± 0.003 for the 200 nm reference (Fig. 5.4 (b)) and the 200 nm as-implanted (Fig. 5.4 (d)) samples, respectively. The similar slopes indicate that the increase in damping with frequency is similar after irradiation. Both samples also have a similar total thickness of ~393 nm (including transducers), which is confirmed by the similarity of the fundamental frequency modes, which are both ~ 10 GHz. Before and after irradiation the FWHM at ~60 GHz is still ~2 GHz, suggesting that the irradiation didn't have a significant effect on the damping. Also of note is that the interface between the irradiated SiN_x and the transducer did not lead to a detectable increase in damping, and therefore no increase in phonon scattering at the interface.

5.5.4 Effect of Nanocrystals on Coherent Acoustic Phonon Damping

To examine the effect of nanocrystals on phonon damping, we compare the 100 nm reference and the 100 nm implanted-annealed samples. The plots of FWHM as a function of frequency are fit with a linear fit that has a slope of 0.041 ± 0.007 and 0.044 ± 0.003 for the 100 nm reference (Fig. 5.4 (a)) and the 100 nm implanted-annealed (Fig. 5.4 (e)) samples, respectively. By comparing the FWHM at ~70 GHz, a ~20% increase in damping for the implanted-annealed sample (~3 GHz) compared to the 100 nm reference (~2.5 GHz) is apparent. Fig. 5.4(f) presents a HAADF STEM image from the implanted-annealed sample, where Ga-doped Si_3N_4 NCs with dimensions in the 200 – 400 nm range are apparent. These NCs were discussed earlier in section 3.5. The increased damping is

likely due to the similarity of the NC size and the phonon wavelength. The phonon wavelength in Si_3N_4 is expected to be ~1 μm at 10 GHz and ~100 nm at 100 GHz.

5.6 Conclusions

In summary, we have examined the effect of membrane nanostructure on coherent acoustic phonon damping. Damping was similar for the 200 nm unimplanted sample, the unimplanted-annealed sample, as well an as-implanted sample. For the thinner 100 nm samples, a ~30% increase in damping was observed. Interestingly, the scaling of damping with frequency is linear, which seems to be different than the exponential dependence in other studies.[6,8,9,10,11,12] More efforts are needed in the future to elucidate this behavior. Nevertheless, the present studies not only show a linear-like relationship between the damping and acoustic mode frequency, but also demonstrate a clear damping dependence on the SiN_x membrane thickness. More work will also be needed to detect the effect of implantation and nanostructure modification on damping. Both the FWHM as a function of frequency and the FWHM data suggest increased damping for the nanocrystalline sample relative to the amorphous samples. The increase is associated with the similarity in length scale of the NC dimensions and the mean free path of the acoustic phonons in the observed spectra. Further experiments could directly correlate nanostructures to damping of specific acoustic phonon frequencies, enabling engineering of the phonon mean free path that can allow for thermal conductivity minimization.

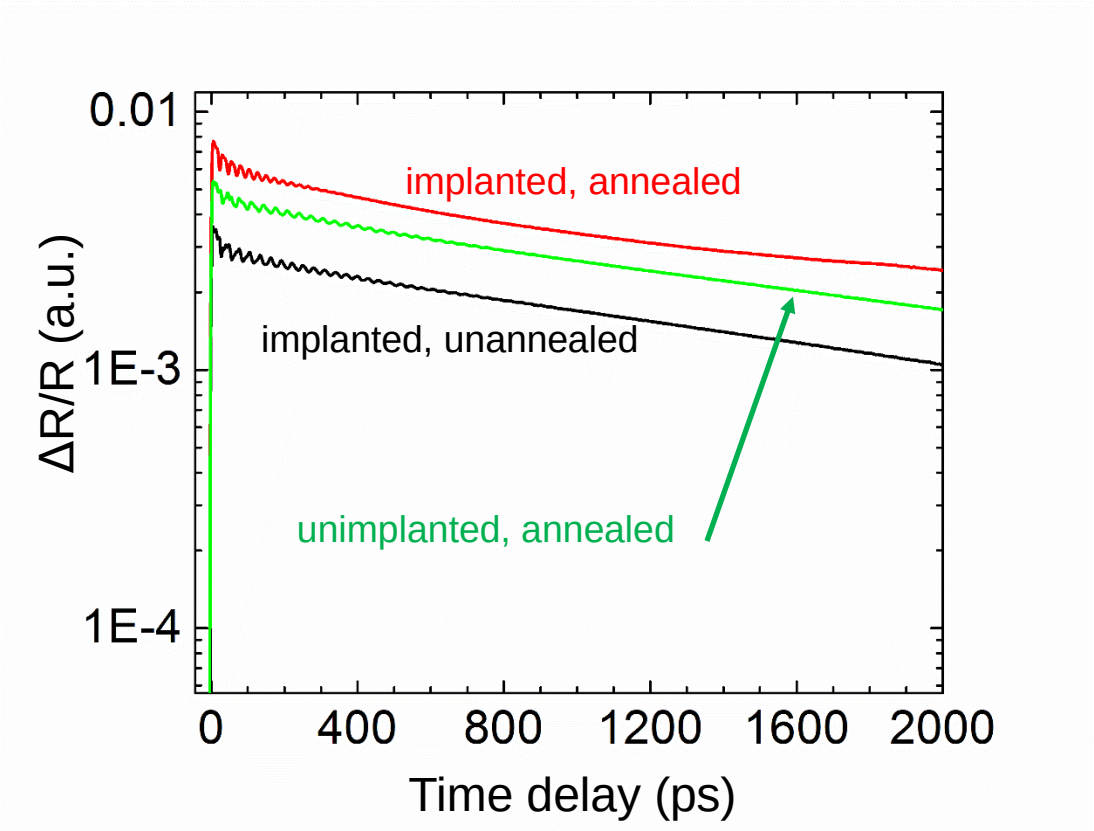

Fig. 5.1 Time-domain Thermoreflectance from the implanted-annealed (red), unimplanted-annealed (green), and implanted-unannealed (black) samples.

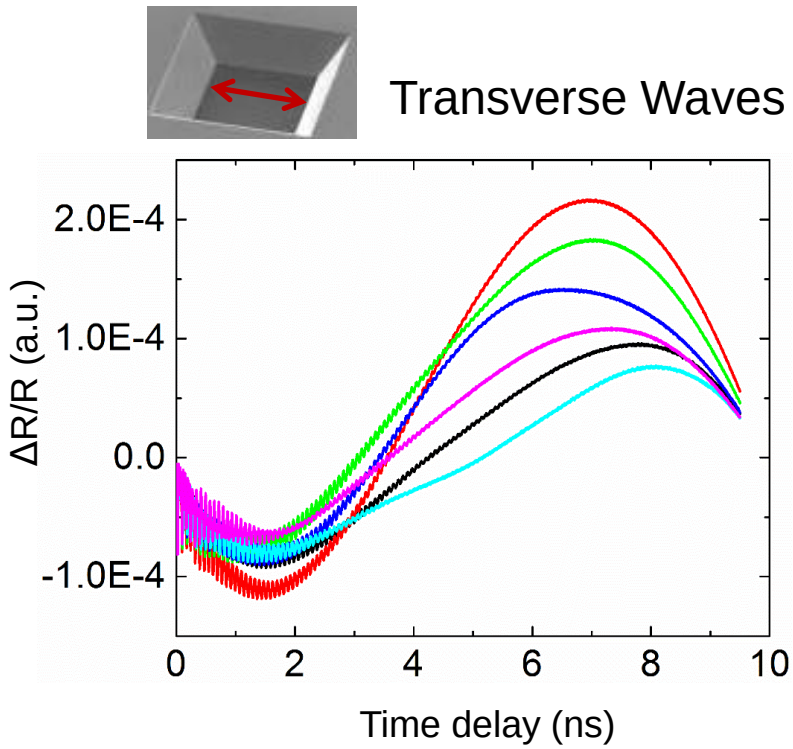

Fig. 5.2 Pump-probe transmission spectra from six different spots across the surface of the implanted-annealed sample. Shifts in phase and amplitude are apparent.

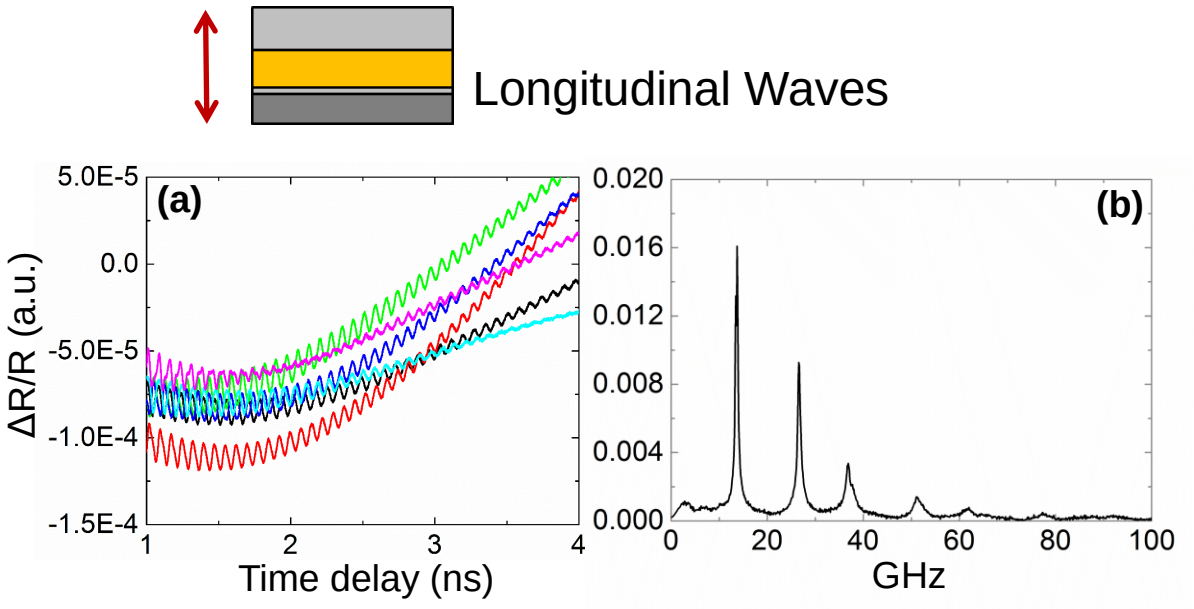

Fig. 5.3 (a) A portion of the pump-probe transmission spectra shown in Fig. 5.2, which shows the high frequency coherent longitudinal phonon waves. (b) A sample FFT from one of the longitudinal waveforms after the transverse waveform has been subtracted.

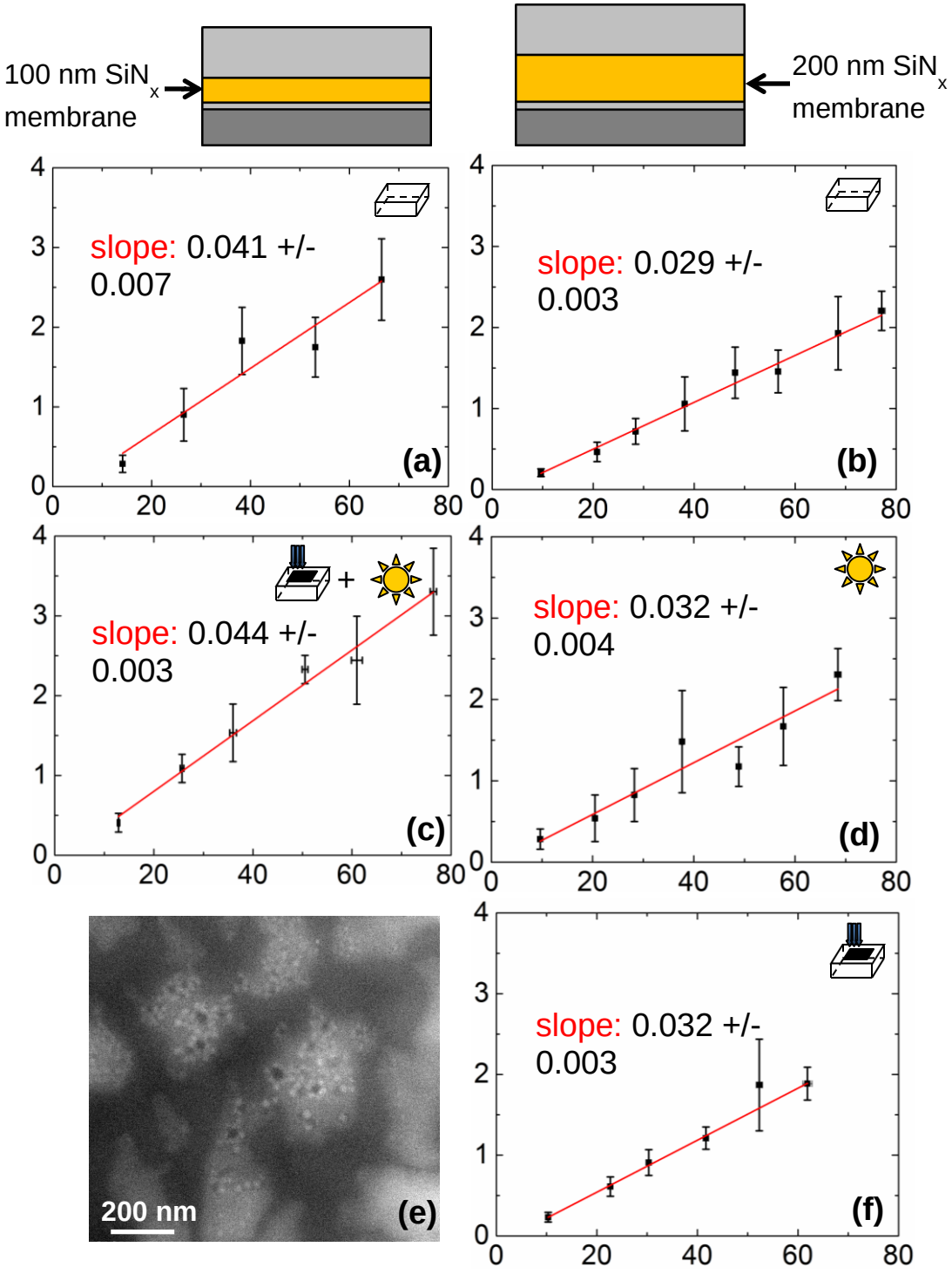

Fig. 5.4 Plots of FWHM (GHz), which is proportional to damping, as a function of frequency (GHz) for the (a) 100 nm reference, (b) 200 nm reference, (c) 100nm implanted-annealed, (d) 200 nm unimplanted-annealed, and (f) 200 nm as-implanted samples. (e) HAADF STEM image of the nanostructure of the 100 nm implanted-annealed sample.

5.7 References

[1] H. Casimir, Physica (Amsterdam) 5, 495 (1938).

[2] Lu, C. *Application of Piezoelectric Quartz Crystal Microbalance*; Elsevier: London, 1984.

[3] Ballantine, D. S.; et al. *Acoustic WaVe Sensors*; Academic Press: San Diego, CA, 1997.

[4] Y. Guillet and B. Audoin, Phys. Rev. B **86**, 035456 (2012).

[5] G. Pernot et al., Nature Mater. 9, 491 (2010).

[6] J. Cuffe, O. Ristow, E. Chávez, A. Shchepetov, P-O. Chapuis, F. Alzina, M. Hettich, M. Prunnila, J. Ahopelto, T. Dekorsy, and C. M. Sotomayor Torres, Phys. Rev. Lett. **110**, 095503 (2013).

[7] A. Bruchhausen, R. Gebs, F. Hudert, D. Issenmann, G. Klatt, A. Bartels, O. Schecker, R, Waitz, A. Erbe, E. Scheer, J.-R. Huntziner, A. Mlayah, and T. Dekorsy, Phys. Rev. Lett. **106**, 077401 (2011).

[8] D. B. Hondongwa, B. C. Daly, T. B. Norris, B. Yan, J. Yang, and S. Guha Phys. Rev. B 83, 121303 (2011).

[9] G. Baldi, V. M. Giordano, G. Monaco, F. Sette, E. Fabiani, A. Fontana, and G. Ruocco, Phys. Rev. B **77**, 214309 (2008).

[10] G. Baldi, V. M. Giordano, G. Monaco, and B. Ruta, Phys. Rev. Lett. **104**, 195501 (2010).

[11] J.-Y. Duquesne and B. Perrin, Phys. Rev. B **68**, 134205 (2003).

[12] F. Hudert, A. Bruchhausen, D. Issenmann, O. Schecker, R. Waitz, A. Erbe, E. Scheer, T. Dekorsy, A. Mlayah, and J.-R. Huntzinger, Phys. Rev. B **79**, 201307(R) (2009).

Chapter 6

Summary and Suggestions for Future Work

6.1 Summary

In this thesis, the formation and spatial positioning of Si, SiN, Ga, and GaN nanoparticles embedded within SiN_x by Ga^+ focused ion beam (FIB) irradiation and rapid thermal annealing (RTA) were investigated. The effect of Ga^+ irradiation on the vibration of SiN membrane based acoustic resonators was also investigated.

In Chapter 3, we discussed the formation of embedded Si, SiN, Ga, and GaN nanocrystals (NCs) in SiN_x using Ga+ focused-ion beam irradiation of SiN_x membranes, followed by rapid thermal annealing (RTA). During irradiation, redeposition is enhanced by developing side walls, leading to enhanced near-surface [Ga] and [Si], while N likely escapes as N_2.[1] We examine TEM images and SAD patterns of the NCs formed for samples with different amounts of redeposited material. We also discuss the sizes of the NCs after different annealing times at 900ºC and the catalytic effect of Ga on Si NC formation.

In Chapter 4, we presented investigations of low dose Ga implantations into SiN_x and the resultant Ga NPs. We examine the many mechanisms that control the size and distribution of the resulting Ga NPs. The effect of dose and annealing on Ga NP growth

are examined with a comparison of STEM images and NP sizes and distributions. We also examine the effect of pitch on the nucleation and growth of Ga NPs. For beam spot separations (pitch) less than the lateral spread of implanted ions, dose-limited diffusive growth is apparent. When the pitch exceeds the lateral spread of implanted ions, the surface roughness increases, and Ga NP coalescence is apparent, leading to a bi-modal distribution of NP sizes. We compare STEM and AFM images to understand the effect of surface curvature on the resulting NP distribution. We also compare the NP sizes and distributions for these samples.

In Chapter 5, we examined the effect of membrane nanostructure on coherent acoustic phonon damping. Damping was similar for the amorphous samples, which included unimplanted samples with different thicknesses as well an as-implanted sample. Following implantation and annealing, a ~50% increase in damping was observed. Both the FWHM as a function of frequency and the FWHM increased relative to the amorphous samples. The increase is associated with the similarity in length scale of the NC dimensions and the mean free path of the acoustic phonons in the observed spectra. Further experiments could directly correlate nanostructures to damping of specific acoustic phonon frequencies, enabling mean free path engineering and thermal conductivity minimization.

6.2 Suggestions for Future Work

6.2.1 Electrical Measurements of SiN_x:Ga Nanocomposites

Nanostructures are predicted[2,3] to lead to materials with enhanced thermoelectric figure-of-merit, *ZT*, compared to bulk materials. *ZT* can be defined as:

$$ZT = \frac{S^2 T \sigma}{\kappa} \tag{6.1}$$

where σ is resistivity, *S* is the Seebeck coefficient, and κ is thermal conductivity. Preliminary samples have been made to measure the electrical conductivity.

For these investigations, amorphous 500 nm SiN_x/ 200 µm Si wafer pieces or amorphous 500 nm SiN_x/ 2 µm SiO_2/ 200 µm Si wafer pieces were irradiated with normal-incidence Ga^+ ions using an FEI Nova 200 Nanolab dual-beam FIB system. The SiN_x layer was saturated with Ga^+ ions through sequential $5x10^{17}$ cm^{-2} dose irradiations at 30 keV (dose rate: ~$9x10^{16}$ $cm^{-2}s^{-1}$), 20 keV (dose rate: ~$6x10^{16}$ $cm^{-2}s^{-1}$), 10 keV (dose rate: ~$3x10^{16}$ $cm^{-2}s^{-1}$), and 5 keV (dose rate: ~$2x10^{16}$ $cm^{-2}s^{-1}$), using a continuous raster scan mode, with p (pitch) = ½ d (spot size).

Contacts for 2-points probe electrical measurements were deposited as described in section 2.8. Various contact recipes were used for these experiments. These include (1) 10 nm TiN / 100 nm Ti/ 100 nm Au, (2) 100 nm Al/ 100 nm Au, and (3) 1 nm TiN/ 100 nm Ti/ 100 nm Au. None of these contacts resulted in significant conductivity, an example of which is shown in Fig. 6.1. The high resistivity may be due to the high resistivity of the SiN_x:Ga nanostructure, the contact resistance, or both. Further experiments are necessary to access the potential utility of SiN_x:Ga as a thermoelectric material.

6.2.2 Transmission Measurements of SiN_x Membranes

In Chapter 5, we described transmission geometry pump-probe measurements of transverse coherent acoustic phonons in the SiNx membranes. A variation in the amplitude and phase of the transverse waves across the surface of the 100 x 100 μm membranes is apparent. It is hypothesized that the amplitude and phase variations are due to constructive and destructive interference of the transverse waves reflecting from the membrane edges. Therefore, it is of interest to systematically vary the distance between pump excitation and membrane edges in order to "map" the transverse waves. This mapping could be used to compare the transverse acoustic phonon resonances of the existing thin SiNx membranes, potentially revealing effects of the microstructure on the damping of acoustic phonons. It is also expected that this measurement will reveal the influence of the membrane boundaries on the amplitude and phase of the transverse acoustic phonons.

6.2.3 Ga-Rich Fractals: Chemistry, Crystallinity, and Acoustic Phonon Resonances

In Chapter 3, we described the formation of Ga-rich fractals using FIB implantation followed by RTA. From the Z-contrast of the HAADF STEM images, it is apparent that the fractals are Ga-rich, but the exact composition is unknown. SAD patterns collected in the regions with fractal morphology suggest the presence of various NCs. However, the crystallinity of the fractals themselves remains unknown. Therefore, we suggest investigations of the chemistry and crystallinity of the fractals using SAD,

BF/DF, and EDX for a variety of irradiation doses both before and after RTA. Knowledge of the chemistry and structure of the fractals both before and after RTA will allow us to further compare our morphology transitions with those reported for Ga_2O_3 and Ge fractals.

Since the fractal regions contain structures with a variety of dimensions ranging from ~40 nm to several microns, they may enable preferential scattering of acoustic phonons in SiN_x. Thus, it would also be interesting to examine the influence of the fractal geometry and fractal dimension on the acoustic phonon resonances within these samples.

6.2.4 Growth of Si Nanowires from Ga Nanoparticles

In Chapter 4, we described processes for controlling the size, density, and distribution of Ga NPs as small as ~3.0 nm ± 0.6 nm with a density up to 4.0 x 10^{12}/cm^2. For the 50 nm pitch as-implanted reference sample (Fig. 4.1(a)), the AFM of this sample in Fig. 4.1(e) suggests that the NPs may be within small divots in the surface. This may enable uniform, vertical growth of Si nanowires. Si nanowires have been previously been grown from Ga NPs following implantation and annealing.[19,4] However, understanding of the early stage growth mechanisms of Ga NPs was not well understood, so a Ga NP distribution with low density and large size range was used for Si nanowires growth. As mentioned in section 1.7, in order to enhance the properties of the laser, the QDs need to have very high density (>5×10^{10}/cm^2), while a uniform size distribution is important for achieving quantum confinement within each of the semiconductor NCs,

while also ensuring a narrow energy range for the light emitted. The NPs described in Chapter 4 meet these requirements, so the remaining question is whether Si nanowire growth from these NP can be demonstrated. With a size of 3 nm, quantum effects may be observable, as a strong increase in quantum confinement is expected for diameters less than 2.2 nm.[110]

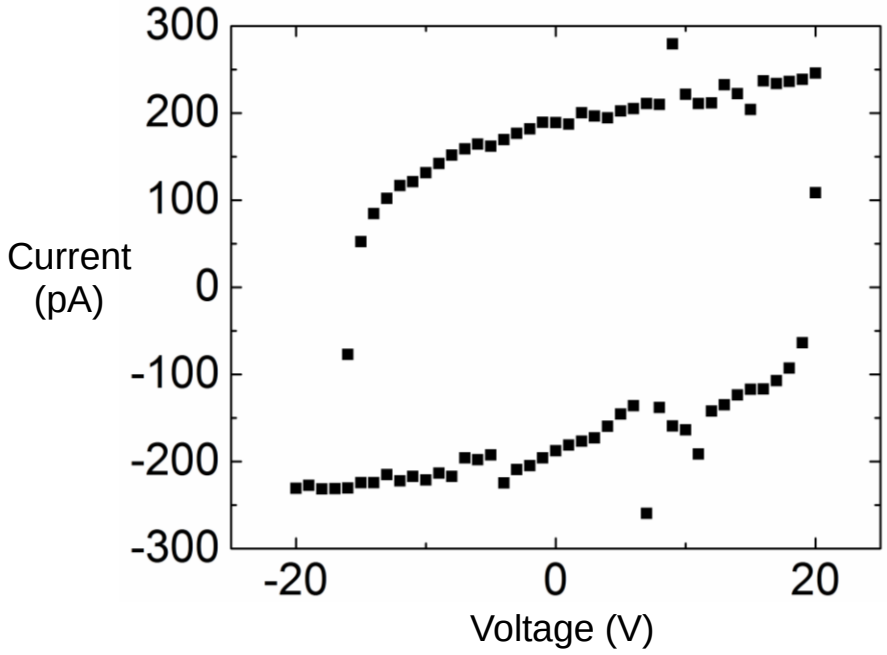

Fig. 6.1 Dual sweep IV measurement showing current (pA) as a function of Voltage (V) for one of the 2-point-probe samples.

6.3 References

[1] S.O. Kucheyev, J.S. Williams, and S. J. Pearton, Mater Sci Eng **33**, 51 (2001).

[2] L. D. Hicks and M. S. Dresselhaus, *Phys. Rev. B* **47**, 12727 (1993).

[3] L. D. Hicks and M. S. Dresselhaus, *Phys. Rev. B* **47**, 16631 (1993).

[4] P. Philipp, L. Bischoff, and B. Schmidt, Nanotechnology **23**, 475304 (2012).

Appendices

Appendix A

Selected Area Electron Diffraction Analysis

When electrons are incident at a scattering angle θ to the planes of a crystalline solid with interplanar spacing *d*, constructive interference is described by Bragg's equation:[1,2]

$$2d\sin\theta = \lambda \tag{A.1}$$

where λ is the wavelength of the electrons. The angle between the incident and diffracted electron beam is 2θ, as shown in Fig. A.1. For a polycrystalline specimen, the diffracted electron beams will form a cone with semi-angle 2θ, as shown in Fig. A.2. The diffracted beams are incident on the TEM phosphor screen, forming a circle with radius R, such that

$$R/L = \tan 2\theta \tag{A.2}$$

where *L* is the distance between the specimen and the TEM phosphor screen. The angle 2θ is very small while the accelerating voltage is on the order of tens of kilovolts.[1] We therefore can approximate $\sin\theta$ as θ and $\tan 2\theta$ as 2θ. Combining Eq. A.1 and Eq. A.2, we find that:

$$Rd = \lambda L \tag{A.3}$$

where λ and L are constants associated with the TEM. We can then solve for d by measuring R. We measure R from the captured diffraction pattern images using the method described below.

The diffraction image is loaded into ImageJ, software that denotes pixel coordinate values. Before any R values can be measured, we must find the location of the center of the diffraction pattern. For diffraction spot patterns, multiple sets of opposite spots can be connected with a line. These lines will cross in the center of the diffraction pattern. For polycrystalline ring patterns, concentric circles can be drawn in Microsoft Word, from which the center point can be found. Once the center point is identified, it is marked with a red dot. The image is then saved and then opened in ImageJ. Linecuts are then taken of the diffraction pattern from the center point to any other point on the image. The linecut is a plot of intensity as a function of R. From this plot we can find the intensity peaks that correspond to the diffraction spots or rings.

These R values must now be converted into d-spacings. Because λ and L are constants, two arbitrary reflections are related by the equation:

$$R_1 d_1 = R_2 d_2 = \lambda L. \tag{A.4}$$

And therefore:

$$d_2 = \frac{R_1 d_1}{R_2} \tag{A.5}$$

In order to solve for d_2, we use a reference diffraction pattern to define d_1 and R_1. It is desirable to have a reference that is in the TEM at the same time as the unknown, such that a small movement of the XY motion of the sample holder is the only difference between conditions used to obtain the unknown diffraction pattern and the reference diffraction pattern. For our case we used the edge of the SiN_x membrane window, which

is single crystal Si. d_1 and R_1 were then found using the reference diffraction pattern along with the standard values listed with the International Centre for Diffraction Data (ICDD).

The crystal structure (e.g. Si, Ga, Si_3N_4, ZB GaN, or WZ GaN) is then determined by comparing the calculated d_2 values with the d spacings from the ICDD. The observed d-spacings are also compared with the predicted highest intensity reflections, also listed in the ICDD, and the predicted ordering of the diffraction spots with respect to each other. An example of the predicted intensities and ordering of diffraction reflections for Si are presented in Table A.1.

d (Å)	h	k	l	I (normalized)
3.1355	1	1	1	100
1.9201	2	2	0	55
1.6375	3	1	1	30
1.3577	4	0	0	6
1.2459	3	3	1	11
1.1086	4	2	2	12
1.0452	5	1	1	6

Table A.1 The d-spacings and predicted intensities and ordering of reflections for Si diffraction.

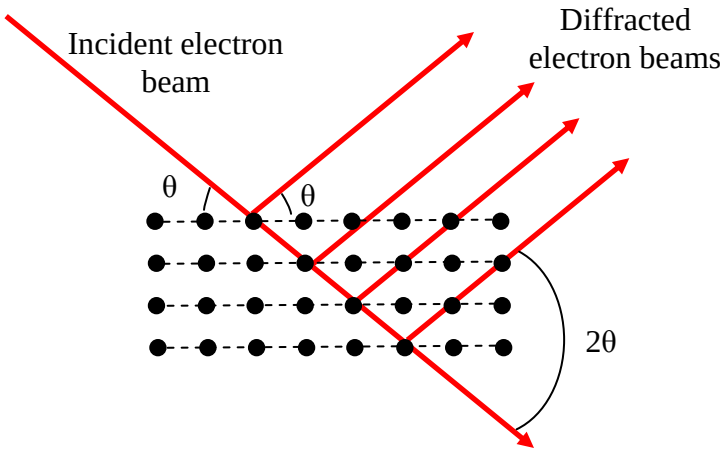

Fig. A.1 A schematic of Bragg electron diffraction from crystal planes.

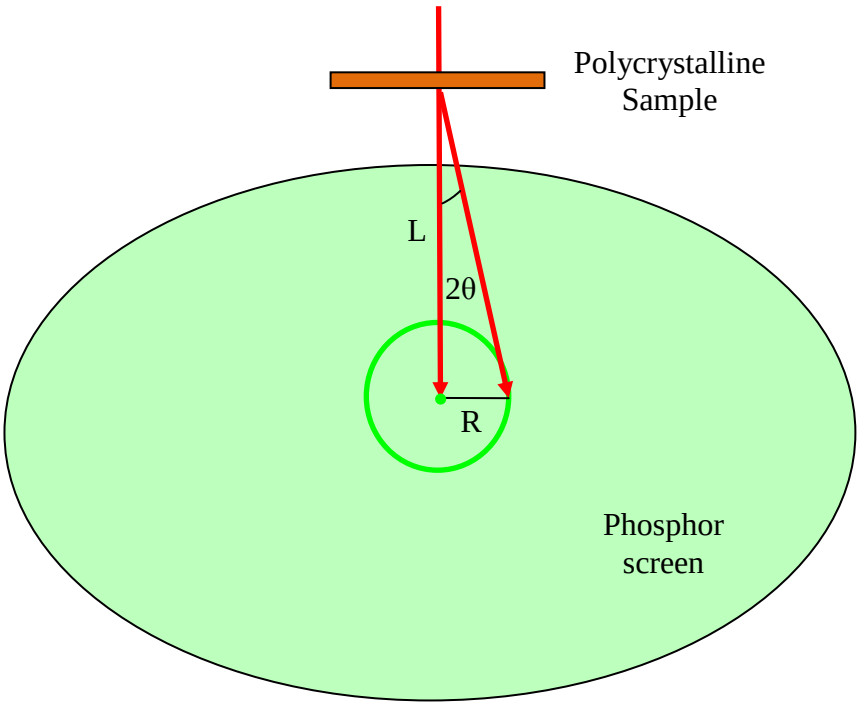

Fig. A.2 Schematic of electron diffraction from a polycrystalline sample. The incident electron beam is diffracted from the sample, forming a cone with semi-angle 2θ. This cone forms a circle of radius R on the phosphor screen.

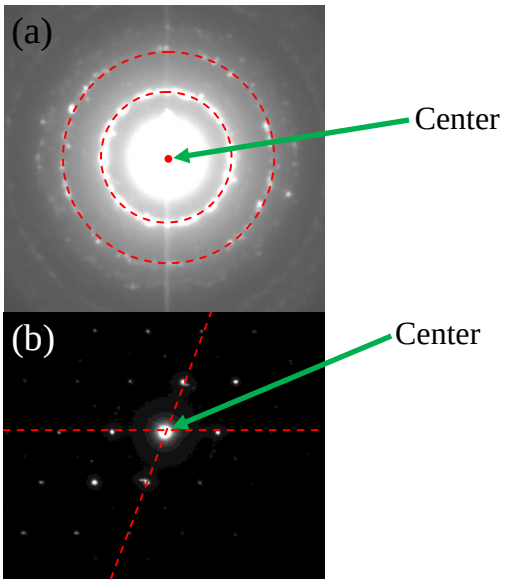

Fig. A.3 Examples of finding the center of a diffraction image (a) using polycrystalline rings and (b) using diffraction spots from single crystals.

References

---

[1] T. B Rymer, *Electron Diffraction* (Methuen & Co. Ltd., London 1970) p.7.

[2] D. B. Williams and C. Barry Carter, eds. *Transmission Electron Microscopy* (Springer Science+Business Media, Inc. New York, 1996), Chapter 35.

Appendix B

Index of Samples

This appendix is a series of tables of all the samples discussed within this thesis. Table B.1 is the Ga-rich fractal samples discussed in section 3.4.2. Table B.2 is the other samples discussed in Chapter 3. Table B.3 is the Ga NP samples discussed in Chapter 4. Table B.4 is the SiN_x:Ga samples used for pump-probe measurements and discussed in Chapter 5.

Table B.1 Ga-rich Fractal Samples

Figure	**Raster-Scan Irradiation Dose ($x10^{17}/cm^2$)**				**Annealing Time @ 900°C**
	30 keV	**20 keV**	**10 keV**	**5 keV**	
3.4(a)	2.85	2.85	2.85	2.85	16 min
3.4(b)	3.05	3.05	3.05	3.05	16 min
3.4(c)	3.23	3.23	3.23	3.23	16 min
3.4(d)	3.43	3.43	3.43	3.43	16 min
3.4(e)	3.63	3.63	3.63	3.63	16 min
3.4(f)	3.8	3.8	3.8	3.8	16 min
3.4(g)	4	4	4	4	16 min
3.4(h)	4.18	4.18	4.18	4.18	16 min
3.4(i)	4.38	4.38	4.38	4.38	16 min

Table B.2 Other SiN_x:Ga Samples from Chapter 3

Figure	**Patterned Dose ($x10^{17}/cm^2$)**	**Raster Scan Irradiation Dose ($x10^{17}/cm^2$)**				**Annealing Time @ 900°C**
	30 keV	**30 keV**	**20 keV**	**10 keV**	**5 keV**	
3.3	none	5.0	5.0	5.0	5.0	28 min
3.7(a)	30	-	-	-	-	8 min
3.7(d)	30	-	-	-	5.0	8 min
3.7(g)	30	-	-	-	5.0	16 min
3.8	30				5.0	16 min

Table B.3 Ga NP Samples from Chapter 4

Figure	**Raster-scan Irradiation Dose ($x10^{18}/cm^2$)**	**Pitch Array**		**Total Dose ($/cm^2$)**	**Annealing**	**NP size/ density**
		Pitch	**Dose in each implanted spot ($x10^{14}/cm^2$)**			**$(nm)/(cm^{-2})$**
4.1(a)	None	50	8.0	4.0 $x10^{14}$	None	3±0.6/4.4e12
4.1(c)	None	95	8.0	1.1 $x10^{14}$	None	None
4.2(a)	None	50	8.0	4.0 $x10^{14}$	16 min @ 900ºC	7.7±2.2/1e12
4.2(c)	2.0	50	8.0	2.0 $x10^{18}$	16 min @ 900ºC	11.9±2.7/5.5e11
4.2(b)	2.0	60	2.0	2.0 $x10^{18}$	16 min @ 850ºC	
4.2(d)	2.0	60	8.0	2.0 $x10^{18}$	16 min @ 850ºC	5.2±2.2/1.6e12
4.4(a)	2.0	50	8.0	2.0 $x10^{18}$	16 min @ 850ºC	5.3±1.6/2.7e12
4.4(c)	2.0	70	8.0	2.0 $x10^{18}$	16 min @ 850ºC	8.0 and 12.6
4.4(d)	2.0	95	8.0	2.0 $x10^{18}$	16 min @ 850ºC	7.0 and 12.9
3.5(a)	2.0	---	-----	2.0 $x10^{18}$	28 min @ 900ºC	24±8

Table B.4 SiN_x:Ga Samples for Pump Probe Measurements in Chapter 5

Figure	**Final SiN_x Membrane Thickness (nm)**	**Raster-scan Irradiation Dose ($x10^{18}/cm^2$)**	**Annealing**
5.4(a)	100	none	None
5.4(b)	200	none	None
5.4(c)	200	none	16 min @ 900ºC
5.4(d)	200	2.0	None
5.4(e)	100	2.0	16 min @ 850ºC

Appendix C

Mechanisms of Diffusion

This appendix contains equations for atomic diffusion, curvature-enhanced atomic diffusion, and thermal diffusivity.

For atomic diffusion due to a concentration gradient, the flux, F, is:

$$F = -D\,\Delta C/\Delta x \tag{C.1}$$

where D is the diffusivity, C is the concentration, and x is the position.

For atomic diffusion due to a curvature gradient, the flux, F, is:

$$F = (-D*C)/(RT) * \Delta\mu/\Delta x \tag{C.2}$$

Where D is the diffusivity, C is the concentration, R is the gas constant, T is the temperature, μ is the chemical potential, and x is the position. The chemical potential due to a curvature gradient is given by:

$$\mu = -2\gamma\frac{\Omega}{R} \tag{C.3}$$

where μ is the chemical potential, γ is the surface energy, Ω is the volume added to the surface, and R is the radius of curvature.[1]

For the transport of heat the flux, F, is:

$$F = -\kappa\,(-\Delta T/\Delta x) \tag{C.4}$$

Where κ is the thermal conductivity, T is the temperature, and x is the position. The thermal conductivity can also be expressed in terms of the thermal diffusivity, α:

$$\kappa = \alpha\rho c_p \tag{C.5}$$

where ρ is the density and c_p is the specific heat capacity.

[1] G. Cao, *Nanostructures and Nanomaterials: Synthesis, Properties and Applications* (Imperial College Press, London, 2004).

Appendix D

Microstructural Analysis of HAADF STEM Images

This appendix describes microstructural analysis of the nanostructure and areal fractions in chapters 3 and 4, and the fractal dimensions in section 3.4.2. In all cases, SPIP 6.0.14[1] was used to analyze HAADF STEM images, with pixels ranging from 0 to 255, indicating grey-scales due to Z-contrast, with 256 appearing bright.

D.1 Nanoparticle/Nanocrystal Size

To analyze the nanoparticle/nanocrystal sizes of these bright Ga-rich nanostructures within our HAADF STEM images, a number of steps were performed. 'Threshold' based detection using the 'Particle and Pore Analysis' tool was used to detect our nanoparticle/nanocrystals.[1] First, bright features with an area larger than $(5/2)^2\pi$ = 19.63 pixels were considered as potential NPs. In order to find the threshold for each nanocrystal, the threshold was increased, starting from 80, by increments of 1 until SPIP detected the NP as a single NP. If the threshold is too low, SPIP will combine close nanoparticle/nanocrystals into one or not detect the NP. Once the proper threshold value was reached, the diameter of the diameter of the NP, as measured by SPIP, was recorded. An example of this process is shown in Fig. D.1. The threshold was increased from 80 (Fig. D.1.(a)) to 120 (Fig. D.1(b)) to 130 (Fig. D.1(c)) and finally to 137 (Fig. D.1(d)), where a value of 17.44 pixels was measured by SPIP to be the diameter of the NP. Using this method, the diameters of the NPs across an image were collected.

We also examined using different background subtractions to normalize the image contrast. Ideally, the images would be normalized such that a uniform threshold can be used for all the NPs. Using different subtractions such as an average x-y profile, quadratic fit, and planar fit; the diameter of the NPs was found to be within 8% of the diameter of the NPs in the unaltered image. But, despite these background subtractions, the threshold values still varied greatly across the sample. These continued variations in threshold can be attributed to the variety of NP brightness, which may result from variations in the [Ga] within the NPs.

Once the diameters of the NPs were collected, the diameters were split into bins with a size equal to the standard deviation and plotted in Origin,[2] software by OriginLab Corporation. By fitting this data in Origin, the standard error of the average NP size was found, where the standard error is defined as the square root of the variance of the data. Thus, we found that the standard error of the fits was expected to be up to 5% of the average NP size.

D.2 Areal Coverage

The areal coverage was found using a process similar to that in section D.1.[1] In order to find the threshold for areal coverage, the threshold was increased, starting from 80, by increments of 1 until the threshold which best identifies the overall nanostructure within the image is selected. An example is shown in Fig. D.2. The value for 'Coverage' shown in the bottom pane in SPIP was then recorded as the areal coverage.

D.3 Fractal Dimension

We consider the fractal dimension, D_f, where:

$$n(\epsilon) = \epsilon^{-Df} \quad \text{(D.1)}$$

where n is the minimum number of open sets of diameter ϵ needed to include the entire fractal set. To find the fractal dimension, we used the ImageJ function which calculates the fractal dimension of a monochrome image.[3] First, using ImageJ we converted the image to a monochrome image, where the dark pixels are set to 0 (on the grey scale), and the bright pixels to 255. Using this function we were able to calculate the fractal dimension of our images. Since we analyzed 2D images, the fractal dimension should be between 1 and 2, with 1 being a simple 2D image and 1.9 being a complex 2D image.[4,5]

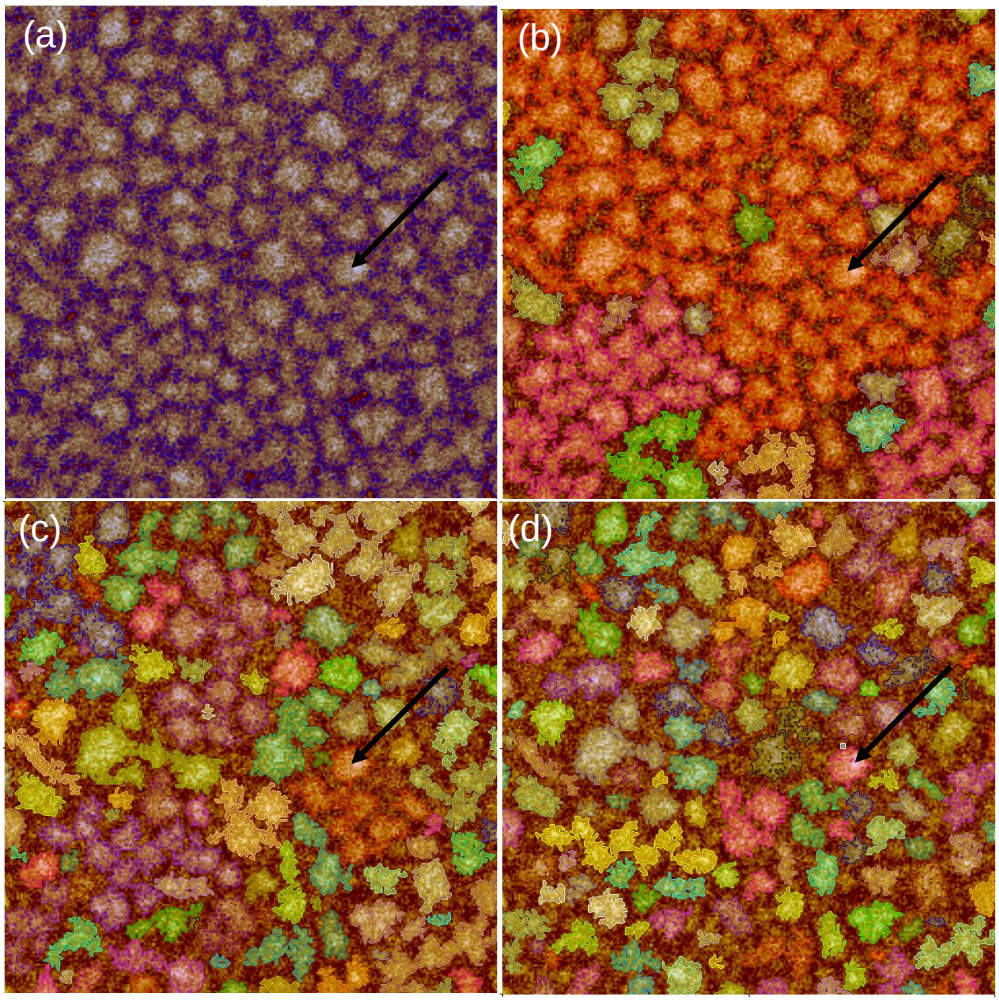

Fig. D.1 For this example the threshold was increased from (a) 80 to (b) 120 to (c) 130 and finally to (d) 137, where the diameter of the NP was measured to be 17.44 pixels. Clicking on the indicated pink outline of the Ga-rich NP in (d) shows the diameter (in pixels) in the pane below the image in SPIP.

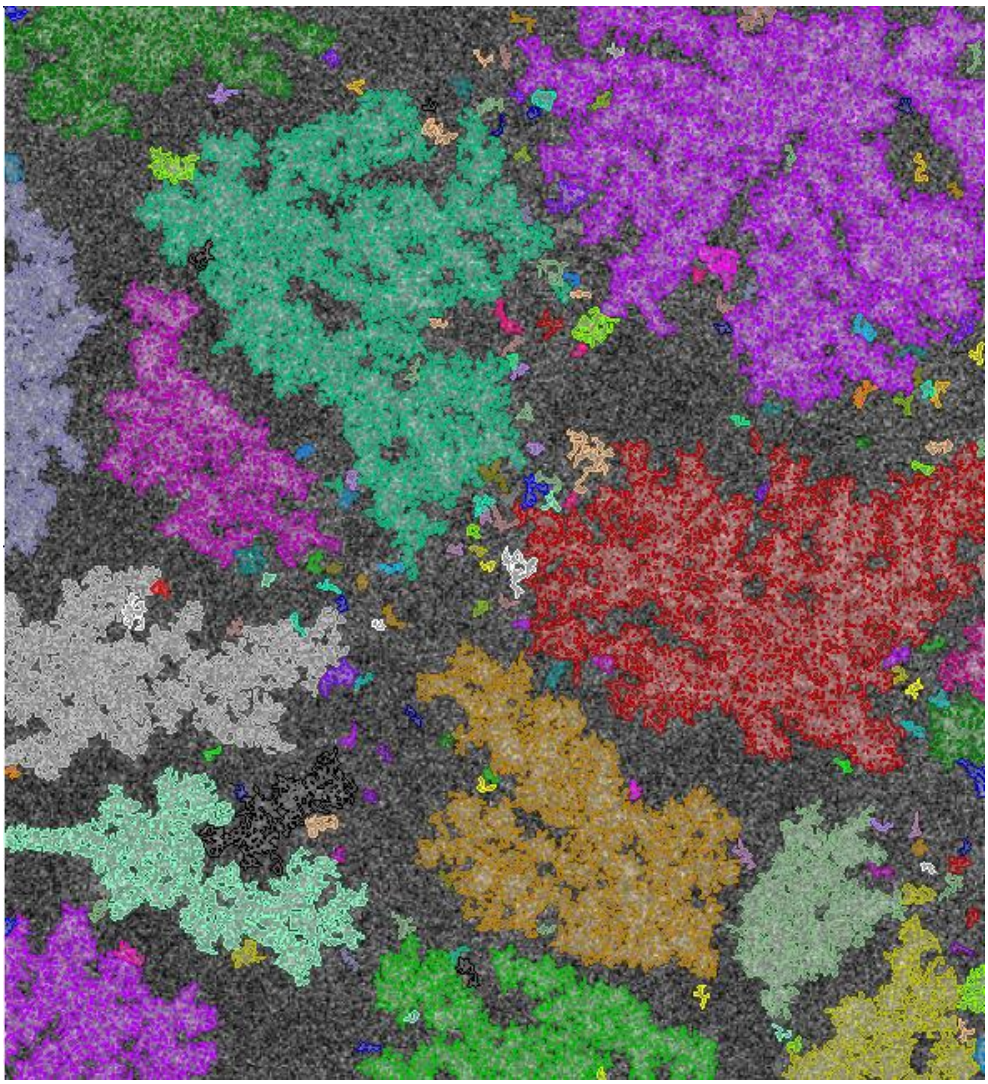

Fig. D.2 Example of features identified by SPIP that were used to find the surface coverage on the Ga-rich fractal sample shown in Fig. 3.4(h).

References

---

[1] SPIP 6.0.14 software by Image Metrology A/S

[2] Origin (OriginLab, Northampton, MA).

[3] Rasband, W.S., ImageJ, U. S. National Institutes of Health, Bethesda, Maryland, USA, http://imagej.nih.gov/ij/, 1997-2012.

[4] B. Davidovitch, A. Levermann, and I. Procaccia, Phys. Rev. E **62**, R5919 (2000).

[5] Mandelbrot, Benoit, *Fractals and Chaos* (2004).

Appendix E

Material Parameters and Procedure for Profile Code Simulations

As mentioned in sections 3.3 and 4.3, Ion Beam Profile Code software by Implant Sciences Corp Profile was used to simulate Ga^+ implantation into SiN_x. Profile Code simulations use empirical formulas based on Monte Carlo simulations to calculate implantation profiles.[1] The simulation takes into account sputtering loss during implantation, unlike other simulations such as Stopping and Range of Ions in Matter (SRIM). Sputtering calculations in Profile Code use empirical equations derived from best-fits to data compiled from the results of weight loss measurements, interferometry, and Rutherford backscattering experiments.[2] For compounds, Profile Code assumes a simple rule of mixtures for sputtering coefficients, so verifying the sputtering coefficient is recommended. Therefore, we measured the sputtering coefficient of SiN_x due to Ga^+ irradiation as detailed below, and used it as the parameter to replace the default in Profile Code. Our measured sputtering coefficient was found to be ~3 times smaller than the default value in Profile Code. Other relevant parameters for simulations of Ga^+ implantation into SiN using Profile Code are presented in Table E.1. The simulations were done using the standard non-Gaussian distribution for ion implantation, the Pearson 4 distribution.

Sputtering coefficients for normal incidence 30 keV and 5 keV irradiation were estimated by irradiating a 20 x 20 μm area of SiN_x with Ga+ ions. The resulting topographic profile was captured using AFM. Presented in Fig. E.1 are AFM line cuts

from (a) 30 keV and (b) 5 keV irradiation. From these lines cuts it is apparent that the sputtering loss due to 30 (5) keV irradiation is ~155 nm (~50 nm) for a dose of $5x10^{17}/cm^2$. Using these sputtering loss values, the sputtering coefficients were calculated and then used to adjust the default sputtering coefficients in Profile Code. Our adjusted sputtering coefficients are listed in Table E.1.

Implantation Energy	Substrate	Atomic Density	Density	Sputtering Coefficient	Sputtering Loss
30 keV	1:1 SiN	$3.87 \times 10^{22}/cm^2$	2.7 g/cm^3	1.200	~ 155 nm
5 keV	1:1 SiN	$3.87 \times 10^{22}/cm^2$	2.7 g/cm^3	0.390	~ 50 nm

Table E.1 Properties of Ga implantation into SiN used for Profile Code simulations.

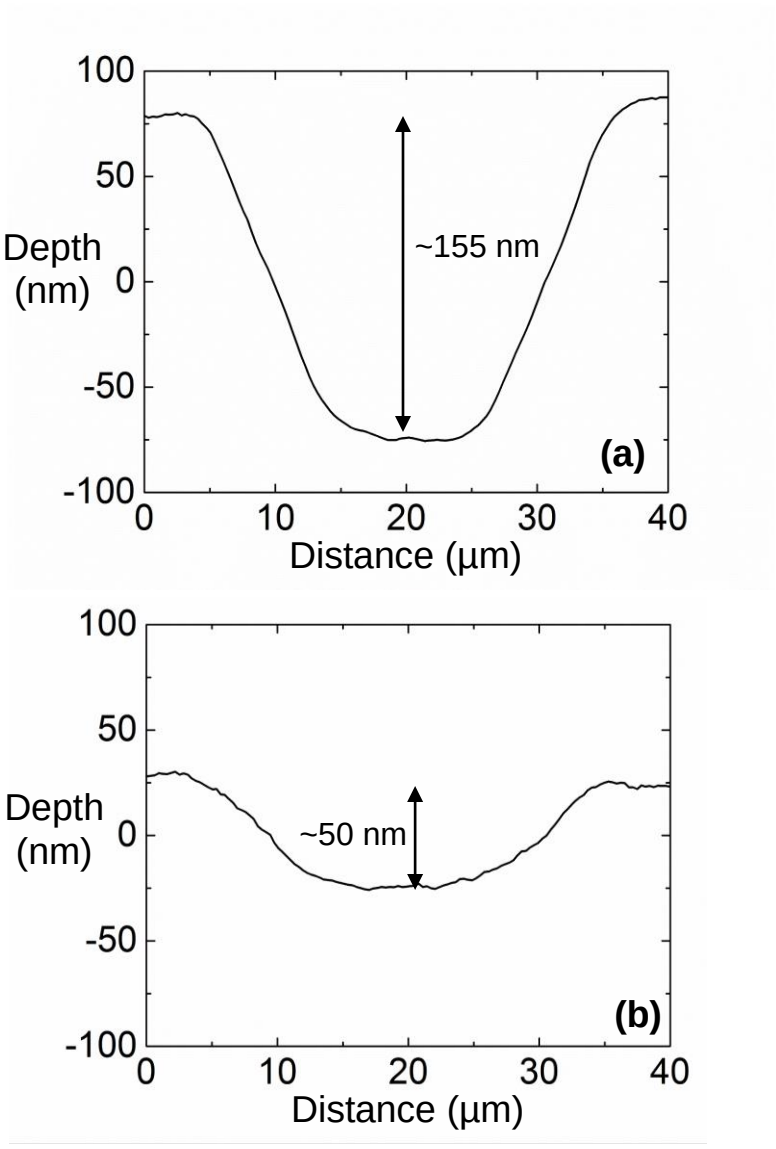

Fig. E.1 AFM lines cuts of 20 x 20 µm squares that were raster-scan irradiated (pitch = half the spot size) at (a) 30 keV and (b) 5keV at a dose of $5x10^{17}/cm^2$.

Appendix F

Analyzing Thermal Conductivity Using Time-Domain Thermoreflectance

We now discuss measuring thermal conductivity using time-domain thermoreflectance. A schematic of the pump/probe experimental setup is shown in Fig. F.1. During measurements, a pump laser pulse heats the sample, while a probe laser reflects off the surface, measuring the thermoreflectance. The temperature change induced is given by:

$$\Delta T(z) = (1-R)\frac{Q}{C(\xi A)}\exp^{-z/\xi} \tag{F.1}$$

where R is the reflectivity, Q is the optical pulse energy, C is the specific heat per unit volume, ξ is the optical absorption length, A is the optical spot area, and z is the distance into the film.[3] A is assumed to be large compared to d, while d is assumed to be large compared to ξ.

By comparing the temperature change ΔT to the results of a one-dimensional heat flow calculation, we can find the value of the thermal conductivity of the sample, κ.[4] The temperature in the metal film is assumed to uniform after 30 ps. Also, the lateral heat flow is assumed to be negligible compared to the heat flow into the sample. Therefore the heat flow into the sample will follow the one-dimensional diffusion equation:

$$\kappa\frac{\partial^2 T_s(z,t)}{\partial z^2} = c_s\frac{\partial T_s(z,t)}{\partial t} \tag{F.2}$$

where $T_s(z,t)$ is the temperature at time *t* at a distance of *z* into the sample, and c_s is the specific heat per unit volume of the sample.

Also, the rate at which the metal transducer loses energy must also be equal to the energy flux into the sample:

$$\kappa \left. \frac{\partial T_s(z,t)}{\partial z} \right|_{z=0} = c_s d \frac{\partial T_m(t)}{\partial t} \tag{F.3}$$

where $T_m(t)$ is the temperature of the metal film.

We must also consider the effect of the thermal-boundary resistance, R_K, which is the ratio of the temperature difference across the transducer/sample interface to the heat flow per unit area through the transducer/sample interface:

$$\kappa \left. \frac{\partial T_s(z,t)}{\partial z} \right|_{z=0} = -\frac{T_m(t) - T_s(0,t)}{R_K} \tag{F.4}$$

The unknown parameters, κ and R_K, are then varied until a curve that best fits the data is obtained.[4]

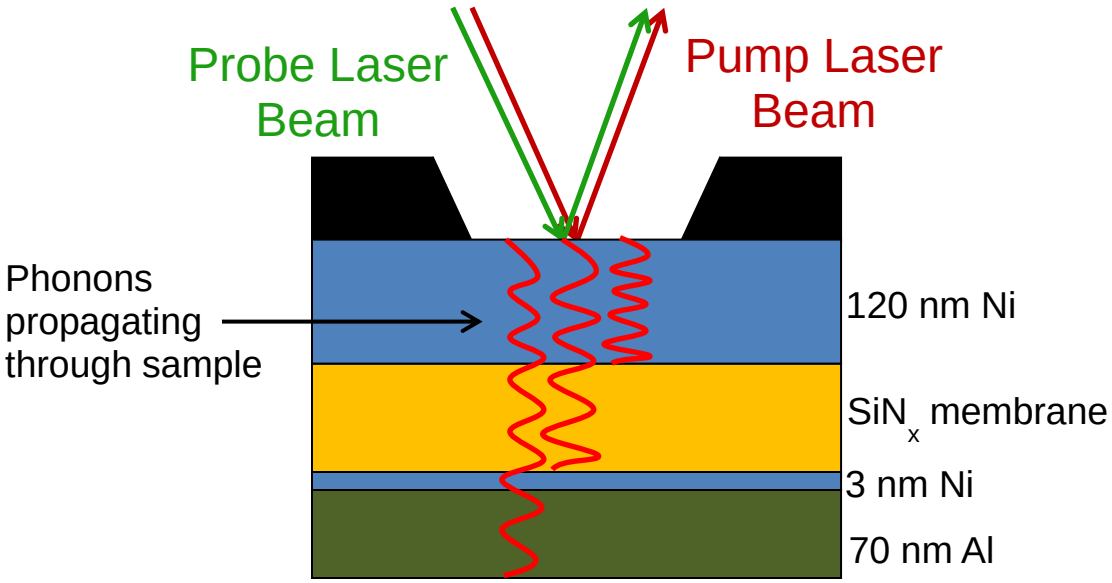

Fig. F.1 Experimental setup for pump/probe time-domain thermoreflectance measurements. A pump laser pulse is incident on a metal film of thickness d. The heat generated from the pulse flows into the sample. The probe laser detects changes in the thermoreflectance.

References

[1] *Profile Code* (Implant Sciences Corp., Wakefield, MA, 1992).

[2] Matsunami et. Al. "Energy Dependence of the Ion-Induced Sputtering Yields of Monatomic Solids," Atomic Data and Nuclear Data Tables, Vol 31, 1-80 (1984).

[3] C. Thomsen, H. T. Grahn, H. J. Maris, and J. Tauc, Phys. Rev. B **34**, 4129 (1986).

[4] G. A. Antonelli, B. Perrin, B. C. Daly, and D. C. Cahill, MRS Bulletin **31**, 607 (2006).